Spring 2012

Automated delineation and quantitative analysis of blood vessels in retinal fundus image

Xiayu Xu
University of Iowa

AUTOMATED DELINEATION AND QUANTITATIVE ANALYSIS OF BLOOD VESSELS IN RETINAL FUNDUS IMAGE

by

Xiayu Xu

An Abstract

Of a thesis submitted in partial fulfillment of the
requirements for the Doctor of Philosophy
degree in Biomedical Engineering
in the Graduate College of
The University of Iowa

May 2012

Thesis Supervisors: Associate Professor Michael D. Abràmoff
Professor Joseph M. Reinhardt

ABSTRACT

Automated fundus image analysis plays an important role in the computer aided diagnosis of ophthalmologic disorders. A lot of eye disorders, as well as cardiovascular disorders, are known to be related with retinal vasculature changes. Many studies has been done to explore these relationships. However, most of the studies are based on limited data obtained using manual or semi-automated methods due to the lack of automated techniques in the measurement and analysis of retinal vasculature.

In this thesis, a fully automated retinal vessel width measurement technique is proposed. This novel method models the accurate vessel boundary delineation problem in two-dimension into an optimal surface segmentation problem in three-dimension. Then the optimal surface segmentation problem is transformed into finding a minimum-cost closed set problem in a vertex-weighted geometric graph. The problem is modeled differently for straight vessel and for branch point because of the different conditions in straight vessel and in branch point. Furthermore, many of the retinal image analysis needs the location of the optic disc and fovea as a prerequisite information, for example, in the analysis of the relationship between vessel width and the distance to the optic disc. Hence, a simultaneous optic disc and fovea detection method is presented, which includes a two-step classification of three classes.

The major contributions of this thesis include: 1) developing a fully automated vessel width measurement technique for retinal blood vessels, 2) developing a simultaneous optic disc and fovea detection method, 3) validating the methods

using multiple datasets, and 4) applying the proposed methods in multiple retinal vasculature analysis studies.

Abstract Approved: _____
Thesis Supervisor

_____
Title and Department

_____
Date

_____
Thesis Supervisor

_____
Title and Department

_____
Date

AUTOMATED DELINEATION AND QUANTITATIVE ANALYSIS OF BLOOD VESSELS IN RETINAL FUNDUS IMAGE

by

Xiayu Xu

A thesis submitted in partial fulfillment of the
requirements for the Doctor of Philosophy
degree in Biomedical Engineering
in the Graduate College of
The University of Iowa

May 2012

Thesis Supervisors: Associate Professor Michael D. Abràmoff
Professor Joseph M. Reinhardt

Graduate College
The University of Iowa
Iowa City, Iowa

CERTIFICATE OF APPROVAL

PH.D. THESIS

This is to certify that the Ph.D. thesis of

Xiayu Xu

has been approved by the Examining Committee for the thesis requirement for the Doctor of Philosophy degree in Biomedical Engineering at the May 2012 graduation.

Thesis Committee: _____
Michael Abràmoff, Thesis Supervisor

_____
Joseph Reinhardt, Thesis Supervisor

_____
Edwin L. Dove

_____
Mona K. Garvin

_____
John A.Goree

_____
Meindert Niemeijer

ACKNOWLEDGEMENTS

First of all, I would like to thank my advisor, Dr. Michael Abràmoff, for his continuous support throughout this work. He is a great mentor who is always full of passion in his research area. He encouraged me to ask questions and to express myself. I could not have come this far without his guidance. A special thanks goes to Dr. Joseph Reinhardt, my other advisor, who has been a great advisor by always inspiring me with brilliant ideas in my research. He is always there to listen and to give advice. His encouragement makes me feel more confident in my study.

I would like to thank the other committee members: Dr. Edwin Dove, Dr. Mona Garvin, Dr. Meindert Niemeijer, and Dr. John A. Goree for their advices on the thesis. Thanks to Dr. Garvin also for all the inspiring disussion, especially in graph theory. Thanks to Dr. Niemeijer for all your help and for your always sharing all the interesting papers. I would like to thank all my colleagues in the research group: Dr. Li Tang, Dr. Kyungmoo Lee, Vinayak Joshi, Mark Christopher and Qiao Hu. Thanks for all the great ideas and advices. Thanks to Mark for developing the iPad version of truthmarker, which makes the manual work less boring to the human experts, and in turn makes my research easier.

During the past four years, I have had a great time in the Medical Imaging Research Lab. My labmates, Dr. Kai Ding, Panfang Hua, Vinayak Joshi, Tarunashree Yavarna, Kaifang Du, Sandeep Bodduluri, and Richard Amendola, are the first ones I can turn to when I have troubles in research, in study and even in daily life. Thanks

to them for their help and being fun to be with.

My sincere thanks goes to the department secretaries, April Tippett and Angie Dickey for their patient assistance during the past years.

Finally, last but not least, I would like to extend a special thanks to my parents, my little brother, and all my friends.

This work was partially supported by the National Eye Institute (R01 EY017066), Research to Prevent Blindness, NY, and the Department for Veterans Affairs.

ABSTRACT

Automated fundus image analysis plays an important role in the computer aided diagnosis of ophthalmologic disorders. A lot of eye disorders, as well as cardiovascular disorders, are known to be related with retinal vasculature changes. Many studies has been done to explore these relationships. However, most of the studies are based on limited data obtained using manual or semi-automated methods due to the lack of automated techniques in the measurement and analysis of retinal vasculature.

In this thesis, a fully automated retinal vessel width measurement technique is proposed. This novel method models the accurate vessel boundary delineation problem in two-dimension into an optimal surface segmentation problem in three-dimension. Then the optimal surface segmentation problem is transformed into finding a minimum-cost closed set problem in a vertex-weighted geometric graph. The problem is modeled differently for straight vessel and for branch point because of the different conditions in straight vessel and in branch point. Furthermore, many of the retinal image analysis needs the location of the optic disc and fovea as a prerequisite information, for example, in the analysis of the relationship between vessel width and the distance to the optic disc. Hence, a simultaneous optic disc and fovea detection method is presented, which includes a two-step classification of three classes.

The major contributions of this thesis include: 1) developing a fully automated vessel width measurement technique for retinal blood vessels, 2) developing a simultaneous optic disc and fovea detection method, 3) validating the methods

using multiple datasets, and 4) applying the proposed methods in multiple retinal vasculature analysis studies.

TABLE OF CONTENTS

LIST OF TABLES viii

LIST OF FIGURES x

CHAPTER

1 INTRODUCTION 1

1.1 Specific Aims 1
1.2 Organization of the Thesis 2

2 BACKGROUND AND SIGNIFICANCE 4

2.1 Anatomy of Eye 4
2.2 Imaging in Ophthalmology 7
2.2.1 Fundus Photography 7
2.2.2 Other Optical Imaging Modality 9
2.3 Retinal Vascular Changes and Related Diseases 11
2.3.1 Methodological Issue in Measuring Retinal Vascular Changes 13

3 AUTOMATED LOCALIZATION OF RETINAL LANDMARKS . . . 19

3.1 Literatures 19
3.2 Methodology 21
3.2.1 Feature Extraction 26
3.2.2 First k-NN Classification 36
3.2.3 Second k-NN Classification 38
3.2.4 Image Post-processing 41
3.3 Experimental Methods 41
3.4 Results 43
3.5 Discussion 48

4 VESSEL WIDTH MEASUREMENT FOR STRAIGHT VESSEL SEGMENTS 56

4.1 Literatures 56
4.2 Methodology 57
4.2.1 Vessel Centerline Extraction 59
4.2.2 Graph Construction 59
4.2.3 Cost Function 63

4.2.4 Graph Search and Boundary Determination 64
4.3 Experimental Methods 64
4.4 Results 66
4.4.1 Relationship between Vessel Width and Distance to Disc . 68
4.5 Discussion 69
4.5.1 Width Measurement on Images of Different Resolution . . 71
4.5.2 Vessel Width and Distance to Optic Disc 73
4.5.3 Computational Performance 75
4.5.4 Limitations 75

5 VESSEL WIDTH MEASUREMENT AT BRANCHING POINTS . . . 77

5.1 Literatures 77
5.2 Methodology 79
5.2.1 Pre-processing and Bifurcation Detection 80
5.2.2 Graph-Based Vessel Boundary Segmentation 82
5.2.3 Cost Function 85
5.2.4 Graph Search and Boundary Determination 87
5.2.5 Graph Search for the Whole Vessel Tree 87
5.3 Experimental Methods 89
5.4 Results 90
5.4.1 Parent Branch-Daughter Branch Relationship 93
5.5 Discussion 98
5.5.1 Parent Branch-Daughter Branch Relationship 99
5.5.2 Computational Performance 102
5.5.3 Limitations 103

6 DISCUSSION 104

6.1 Future Work 105

7 CONCLUSION 109

REFERENCES 111

LIST OF TABLES

Table

3.1 Features extracted for the first k-NN classification. 28

3.2 Selected features for the first k-NN classification. 54

3.3 Features extracted for the second k-NN classification 54

3.4 Overview of test results 55

4.1 Vessel Width Measurement Accuracy of HRIS (success rate in percentage, mean μ and standard deviation σ in pixel) 67

4.2 Vessel Width Measurement Accuracy of CLRIS (success rate in percentage, mean μ and standard deviation σ in pixel) 68

4.3 Vessel Width Measurement Accuracy of VDIS (success rate in percentage, mean μ and standard deviation σ in pixel) 69

4.4 Vessel Width Measurement Accuracy of KPIS (success rate in percentage, mean μ and standard deviation σ in pixel) 70

5.1 Comparison of the performances between human experts and presented method (Vessel widths are in pixels. E_1 and E_2 denote the two human experts. Alg denotes the presented method. μ and σ are the mean and standard deviation of vessel width measurements). 92

5.2 Comparison of the performance between human experts and presented method (Signed error and unsigned error are in pixels. E_1 and E_2 denote the two human experts. Alg denotes the presented method. Ave denotes the average measurements of the two human experts. μ and σ are the mean and standard deviation of errors). 93

5.3 Simulated branch point vessels to illustrate the relationship between vessel width and corresponding fitting power x in model $d^x = d_1^x + d_2^x$, where d is the diameter of parent branch in pixels, d_1, d_2 are the diameters of children branches in pixels. 98

5.4 Comparison of the performances of different parent branch-daughter branch relationship models ($\mu \pm \sigma$ in μm). 98

LIST OF FIGURES

Figure

2.1 Illustration of eye anatomy [1]. 4

2.2 Light path of the visual system [2]. 5

2.3 First known image of human retina as drawn by van Trigt in 1853 [3]. . . 8

2.4 Fundus camera and fundus photograph. (a)Fundus Camera [4]. (b)A Normal Eye Fundus Photograph. 9

2.5 Example figures of multiple ophthalmologic imaging techniques. (a) Peak phase angiogram in a patient with diabetes demonstrates areas of hyporfluorescence in the superior macula secondary to a vascular filling defect as well as hyperfluorescent microaneurysms [5]. (b) Ocular ultrasound: Ultrasound image of a normal eye with lens [6]. (c) Scanning laser ophthalmoscope image of the left eye retina (image courtesy to Michael Judge Brislin). (d) OCT scan of a retina at 800 nm with an axial resolution of 3 μm [7]. 11

2.6 Examples of low and high arteriole-venule ratio [8]. 16

3.1 RGB channels of Figure 2.5. (a)Color fundus image. (b)Red channel. (c)Green channel. (d)Blue channel. 22

3.2 Vessel probability image and vessel centerline image of Figure 2.5. (a)The vessel probability image. (b)The final binary image with centerline pixel inside. 24

3.3 Distance transform of Figure 2.5. (a)The binary image before erasing noise regions. (b)The distance map of (a). It is influenced by small noises greatly. (c)The binary image after erasing noise regions. (d)The distance map of (c). The influence by noise regions disappears. 25

3.4 Circular template of inner radius r and outer radius $\mathcal{R}$. The template is divided into four quadrants. 27

3.5 Illustration of how vessel features are computed. The outer radius of the template is 15 pixels. The inner radius is not shown because it is not used in vessel feature extraction. Vessel pixels are shown in gray and vessel centerlines are shown in black. Pixel 1 is the template center. Arrow a denotes the vessel orientation at pixel 2. Arrow b denotes the direction along which the vessel width is calculated. 29

3.6 A standard true distance map for Figure 3.1. (a). The background is normalized to 127. The higher the gray value is, the higher the probability of being within an optic disc. The lower the gray value is, the higher the probability of being within a fovea. 33

3.7 Feature selection with different criteria. (a)The performance of $\mathcal{C}1$ (1-25 selected features). (b)The performance of $\mathcal{C}1$ (4-25 selected features showing in details). (c)The performance of $\mathcal{C}2$ (1-25 selected features). (d)The performance of $\mathcal{C}2$ (4-25 selected features showing in details). . . 35

3.8 Criterion comparison. (a)Fundus image. (b)Result image using first 11 selected features from $\mathcal{C}1$. (b)Result image using first 11 selected features from $\mathcal{C}2$. $\mathcal{C}1$ performs better than $\mathcal{C}2$ at the image FOV boundary. For images (b) and (c), the background is normalized to 127. The higher the gray value is, the higher the probability of being within an optic disc. The lower the gray value is, the higher the probability of being within a fovea. 37

3.9 Illustration of k-NN regression. k=5 neighbors are found in this example. The red circles denote optic disc pixels ($\mathcal{D} > 50$). The blue stars denote fovea pixels ($\mathcal{D} < 50$). The black triangles denotes background pixels ($\mathcal{D} = 50$). Green star is the test pixel. 39

3.10 Example of first k-NN classification result. Two large regions on the image are labeled as fovea. The region on the left is falsely detected. (The background is normalized to 127. The higher the gray value is, the higher the probability of being within an optic disc. The lower the gray value is, the higher the probability of being within a fovea.) 40

3.11 Examples of typical result of first k-NN classification. Each row shows a paired left eye and right eye result from the same person. The background is normalized to 127. The higher the gray value is, the higher the probability of being within an optic disc. The lower the gray value is, the higher the probability of being within a fovea. 45

3.12 Examples of typical result of second k-NN classification. Each row shows a paired left eye and right eye result from the same person. The false responses has been suppressed. The higher the gray value is, the higher the probability of being within an optic disc. The lower the gray value is, the higher the probability of being within a fovea. 46

3.13 Histograms. Images (a),(b) are the general distance errors of the optic disc and fovea. Images (c),(d) are the distance errors of the left eye. (e), (f) are the distance errors of the right eye. 47

3.14 The correlated error of the optic disc and fovea for both eye images. The x-axis is the distance error of the optic disc. The y-axis is the corresponding distance error of the fovea. 48

3.15 The effect of vessel probability image on the detection result. The top row shows what a normal vessel probability image looks like and the corresponding optic disc/fovea probability image. The second row and last row show two bad cases where insufficient information is provided by the vessel probability image. 51

3.16 Examples of bad quality fundus images and results. The left column shows the fundus images. The right column shows the optic disc/fovea detection results. Though the image qualities are low, our system is able to correctly detect the locations. 52

3.17 Examples of bad quality fundus images and results. The left column shows the fundus images. The right column shows the results. Our system failed to detect the optic disc/fovea locations. 53

4.1 Illustration of the difficulties in accurate vessel width measurement. When the vessels are inspected locally, the vessel edge is very blurry and not well-defined. (a), (b) Two zoomed-in high quality normal fundus images. The rectangular areas show two vessel segments, which seems very clear and well-defind. (c), (d) Enlarged rectangular areas of (a) and (b). The vessel edge appears very blurry. 58

4.2 Example vesselness image generated by a pixel classification method proposed by Niemeijer *et al.* [9]. (a) The color fundus image. The white rectangular is enlarged and used for illustration in Figure 4.3. (b) The corresponding vesselness image. 60

4.3 Illustration of how to luxate the vessel normal profiles into a graph. (a) A small segment of vessel extracted from Figure 4.2. (b) The vessel probability image of (a). (c) The vessel centerline image of (a). (d) The vessel growing directions are calculated and node normal profile perpendicular to the vessel growing direction are constructed. (e) Red normal profiles in (d) are used to build the red graph slice and the green normal profiles in (d) are used to build the green graph slice. The black nodes represent base nodes, corresponding to the black centerline pixels in (d). Consequently, the red slice represents one boundary in (d) and the green slice represents the other boundary in (d). Smoothness constraints (controlled by the arcs between adjacent columns) are applied differently to control the boundary smoothness within one boundary and between the two boundaries. . . . 62

4.4 Gradient image. (a) Part of a green channel image. (b) The corresponding orientation sensitive gradient image. 64

4.5 Sample images showing the result of vessel boundary detection. (a) One image from the CLRIS database. Image size is 2160×1440, $\sigma = 4$. (b) A enlarged part of image (a). 66

4.6 Correlation of predicted vessel width and the mean of the observers' measurements for HRIS. Each point represent one profile. The red line is the $y = x$ line. The black line is the regression line ($y = 0.87x + 1.56$). . . . 71

4.7 Visualization of the relationship between vessel width and distance to optic disc. The black circle marks a 400 pixels to the optic disc center. The vessel width analysis starts from the optic disc center and ends at a distance of 450 pixels (the x-axis). The y-axis shows the vessel width in pixels. The green line is the average vessel width. The black lines are the 95% confidence interval lines. Image resolution is about 800×700 pixels. Scale parameter $\sigma = 4$ pixels was used. 72

4.8 Vessel width measurement on vessel segments with different resolutions. (a) One test vessel segment from HRIS. The length of the vessel segment is 173 pixels. (b) One Test vessel segment from KPIS. The length of the vessel segment is 226 pixels. (c) The vessel width measurement result of (a). If the detected edge is not at an integer location, the nearest integer coordinate is shown. (d) The vessel width measurement result of (b). If the detected edge is not at an integer location, the nearest integer coordinate is shown. (e) The cross-sectional view of vessel intensity with regard to the distance to the centerline for (a). The black curve is the average of 173 normal profiles in the vessel segment. Intensities at non-integer locations are linearly interpolated. The red star is the average vessel width across the whole vessel segment marked by observers. The green star is the average vessel width across the whole vessel segment measured by proposed method. The two boundaries are flipped and shown in one figure. (f) The cross-sectional view of vessel intensity with regard to the distance to the centerline for (b). The black curve is the average of 226 normal profiles in the vessel segment. Intensities at non-integer locations are linearly interpolated. The red star is the average vessel width across the whole vessel segment marked by observers. The green star is the average vessel width across the whole vessel segment measured by proposed method. The two boundaries are flipped and shown in one figure. 74

5.1 Spur pruning and crossing point exclusion on vessel centerline image. (a) An enlarged part of a color fundus image. (b) The corresponding vesselness map. (c) The corresponding vessel centerline image, with detected branching points shown in gray. Spurs are presented due to abrupt vessel direction changes. A crossing point is split into two branching points. (d) The corresponding vessel centerline image after spur pruning and crossing point exclusion. 82

5.2 Illustration of problems in applying traditional graph construction method to branching points and introduction to electric field theory based graph construction method. (a) A figure to illustrate possible problems in applying traditional graph construction method to branching point situation. The problems include possible graph column intersection and graph columns running into another vessel branch. (b) Introduction to electric field theory based graph construction method. Its most attractive is the non-intersecting property of electric field lines. 84

5.3 Improvement of the electric field theory based graph construction method. For illustration purposes, not all graph columns are shown in the figure. (a) Problems encountered when combining the traditional graph and electric field theory based graph. The graph columns intersect each other because the graph columns from the electric field theory based method point outside rather than the normal direction when approaching the end of sub-branches, as shown in dashed red lines. (b) Improved combined graph. Two strategies are introduced to improve the construction of the combined graph. 86

5.4 Illustration of graph construction, cost function design, and vessel width measurement at branching point. Three graphs are built for the three boundaries separately, as shown in color green, blue, and purple. The black dots denote the end of straight vessel segment and start of branching vessel segment. Low cost is given to those nodes to fix the ends of the boundaries at branching point. After the three boundaries are determined, the vessel width is measured as the Euclidean distance between the corresponding nodes from the same centerline pixel. 88

5.5 Illustration of the ground truth generation. Suppose the red, green, and blue lines are vessel width manually marked for branch 1 by one observer. The vessel width for branch 1 is calculated as the average of the three width profiles. The branch center for branch 1 is calculated as the average of the three width profile center. 90

5.6 Illustration of the tablet-based image evaluation system. The human observer is able to locate the center of parent branch center and label it as an artery or a vein. 91

5.7 Typical vessel width measurement images. Red lines denote the vessel width measurement for branching points. Black lines denote the vessel width measurement for straight vessels. 92

5.8 Vessel width measurement scatter plots. (a) The scatter plot of vessel width measured by automatic algorithm and the average of vessel width given by observer 1 and observer 2 for artery branchings. (b) The scatter plot of vessel width measurement performed by observer 1 and observer 2 for artery branchings. (c) The scatter plot of vessel width measured by automatic algorithm and the average of vessel width given by observer 1 and observer 2 for vein branchings. (d) The scatter plot of vessel width measurement performed by observer 1 and observer 2 for vein branchings. 94

5.9 Bland-Altman plots. (a) Bland-Altman plot of proposed method and observer 1. (b) Bland-Altman plot of proposed method and observer 2. (c) Bland-Altman plot of proposed method and the average of observer 1 and observer 2. (d) Bland-Altman plot of observer 1 and observer 2. 95

5.10 Scatter plot of the measured vessel width and predicted vessel width by applying the model $d^x = d_1^x + d_2^x$, where d is the caliber of parent branch and d_1, d_2 are the calibers of daughter branches. (a) The best fitting for arterial branch was found at $x = 3$, which conforms to the Murray's law. (b) The best fitting for venous branch was found at $x = 2.3$ which deviates from the Murray's law. 96

5.11 Bland-Altman plots of real parent branch width and predicted parent branch width. Predicted parent branch width calculated by $d = (d_1^x + d_2^x)^{1/x}$, where d_1 and d_2 are the calibers of two daughter branches. (a) Bland-Altman plot of arterial branch points. $x = 3$. (b) Bland-Altman plot of venous branch points. $x = 2.3$. 97

5.12 Histograms of fitting power x in model $d^x = d_1^x + d_2^x$. (a) Histogram of arterial branch points. (b) Histogram of venous branch points. 99

5.13 Comparison of the performance of different models. (a), (b) Murray's junctional exponent model for artery and vein. (c), (d) Parr-Hubbard model for artery and vein. (e), (f) Knudtson's revised model for artery and vein. 100

5.14 Examples of typical arterial branching and venule branching. Arteries usually have a lower contrast with the background comparing with veins. (a) A typical arterial branching. (b) A typical venule branching. 101

5.15 Example images with similar diameters of parent branch and daughter branch. Branches with white circles denotes parent branches. 102

6.1 Illustration of the region used to calculate AVR in Knudtson's revised formulas. 107

CHAPTER 1
INTRODUCTION

Fundus photography is the most popular and widely accepted image modality in computer aided diagnosis and detection for multiple eye diseases and diseases that show signs on the human retina. An objective assessment of retinal vessel caliber from fundus photographs provides information about the microvascular characteristics, which are known to be associated with eye diseases, such as retinitis pigmentosa, and cardiovascular diseases such as stroke, hypertension, and arteriosclerosis. However, most of the studies were carried out using manual or semi-automated methods due to the lack of a fully automated retinal vessel evaluation method and hence involved lots of painstaking manual work of identifying blood columns and measureing vessel width. The lack of a fully automated retinal vessel delineation and quantitative analysis technique restricted the possibility of large scale studies on using retinal vessel parameters as a biomarker of multiple diseases. A fully automated and precise quantification method for retinal vessel is hence desirable and of great importance.

1.1 Specific Aims

There are several sub-problems in the automated quantification of retinal blood vessel. For instance, the detection of optic disc and fovea is necessary to establish a coordinate system for the whole image and determine the region of interest (ROI). Vessel segmentation must be done to find the vessels themselves. An accurate measurement of vessel width is the most important and challenging problem in the quantitative

analysis of retinal blood vessel.

In particular, the specific aims of the work described in this thesis are as follows:

- Aim 1: Develop a fully automated method for simultaneous detection of the optic disc and fovea, or two optic discs on stereo pair image and to evaluate this method on large datasets.
- Aim 2: Develop an automated vessel width measurement method, including measurement of vessel width at vessel segments and branching points, and to evaluate this method by comparing the result of proposed method with human observers' measurements and existing formulas.
- Aim 3: Describe the parent branch-daughter branch relationship for arteriols and venules.

1.2 Organization of the Thesis

This thesis is divided into 7 chapters. The rest of the thesis is organized as follows:

- Chapter 2 gives an in-depth background description of this thesis, including an introduction to eye anatomy and multiple ophthalmolgy imaging techniques, and a discussion of the relationship between retinal vessel parameters and multiple diseases, which serves as the motivation of this thesis.
- Chapter 3 presents a simultaneous optic disc and fovea detection method based on a machine learning technique.

- Chapter 4 presents an accurate vessel width measurement technique on fundus photography using a graph-based approach.
- Chapter 5 presents a vessel width measurement method designed for branching points and the analysis of multiple retinal vessel parameters.
- Chapter 6 provides some general discussions of this thesis and proposes some possible future works.
- Chapter 7 concludes the thesis.

CHAPTER 2
BACKGROUND AND SIGNIFICANCE

This chapter gives an in-depth background description of the thesis. The basic eye anatomy is given in Section 2.1. The introduction to fundus camera imaging and other ophthalmology imaging modalities is given in Section 2.2. A discussion of the relationship between multiple diseases and retinal vascular changes is given in Section 2.3. This serves as the motivation of the study in this thesis.

2.1 Anatomy of Eye

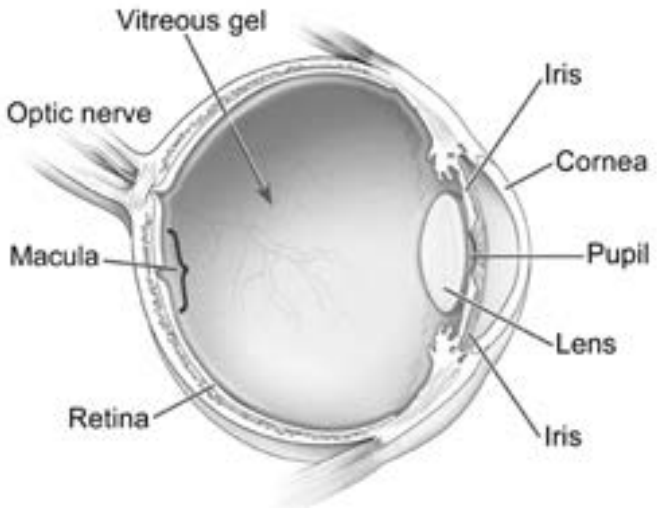

Figure 2.1: Illustration of eye anatomy [1].

The human eye is a complex biological device. The mechanism of how a camera catches an image is often compared with the working of the eye, as shown in Figure

2.2. Light entering the eye is first refracted when it passes through the cornea. It then passes through the pupil and is further refracted by the lens. Finally, it reaches the retina and is converted to electrical signals by photosensitive photoreceptor. The electrical signals are transmitted to the brain along the optic nerve [10].

The light entering the eye is first refracted by the cornea. The cornea is the transparent front part of the eye. However, the focal distance of the cornea is fixed, which means that the cornea can only refract light with a constant angle. The lens, on the other hand, can adjust its focal distance so that incoming light can be focused on the retina. This is similar to the focusing of a photographic camera via movement of its lenses. The lens is a transparent structure lying behind the iris and the pupil.

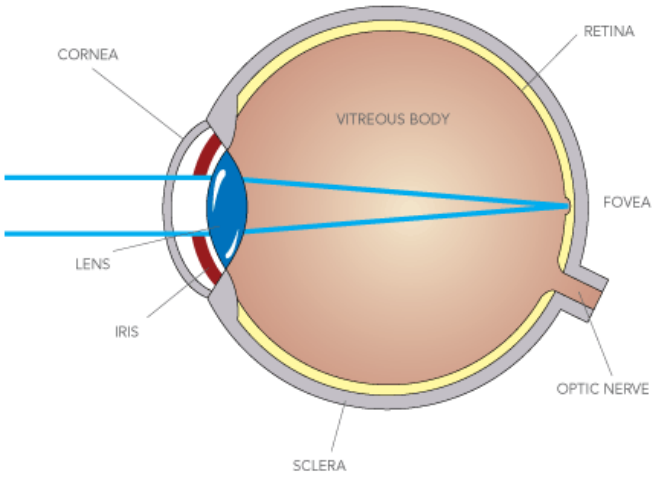

Figure 2.2: Light path of the visual system [2].

The iris is a membrane organ in the eye. It controls the diameter and size of the pupil and hence the amount of light reaching the retina. The movement of iris is

controlled by the iris dilator muscle. The pupil is an opening in the center of the iris. It allows light to enter the eye and reaches the lens. The pupil appears to be black because most of the light entering the pupil is absorbed by the pigment epithelium.

The vitreous is the transparent, colorless, gelatinous mass that fills the space between the lens and the retina. It is also referred to as the vitreous body or vitreous humor. The vitreous contains very few cells, no blood vessels, and $98-99\%$ of its volume is water. Unlike the fluid in the frontal part of the eye which is continuously replenished, the gel in the vitreous is stagnant. So if blood or cytosol get into the vitreous, they may not be reabsorbed for an extended period of time.

The fovea centralis, usually known as the fovea, is located in the center of the macular region on the retina(as shown in Figure 2.1). The fovea is responsible for sharp central vision and is avascular. Approximately 50% of the nerve fibers in the optic nerve carry information from the fovea [10].

The optic disc or optic nerve head is the location where ganglion cell axons exit the eye. It is placed $3-4$mm to the nasal side of the fovea. The optic nerve is a bundle of more than one million nerve fibers. The optic nerve connects the retina to the brain. It is also the place where all retinal blood vessels originate and converge. The retinal blood vessel is unique in that it is the only part of the human circulation that can be directly visualised non-invasively in vivo, readily photographed and subject to digital image analysis [11]. The vascular tree of the retina actually consists of arterioles and venules, rather than arteries or veins. This is because the widest part of the lumen of the retinal vessels is near the optic disk with diameters

of about 100 μm, with neither internal elastic lamina nor a continuous muscular coat [12].

The retina is a light sensitive tissue layer lining the inner surface of the eye. The photosensitive cells on the retina detect light passing through the cornea and lens. The retina is comparable to the film of a camera.

2.2 Imaging in Ophthalmology

The fundus of the eye is the interior surface of the eye, including the retina, optic disc, macula and fovea. The fundus is the only part of the human body where both the circulation and the nerve tissue can be inspected non-invasively. Imaging techniques in ophthalmology has undergone large growth in the past years [13]. This section provides a brief introduction to some of the imaging techniques. Fundus photography is introduced in Section 2.2.1. Fundus photography is the most commonly used technique in ophthalmology imaging and is also the main image studied in this thesis. Other imaging modalities are briefly introduced in Section 2.2.2

2.2.1 Fundus Photography

A fundus photograph is an image of the fundus taken by an ophthalmoscope, or a fundus camera. The first images of the fundus were drawn by the Dutch ophthalmologiest van Trigt in 1853 (Figure 2.3) [3].

A normal human fundus photograph is shown in Figure 2.5. A normal human fundus photograph is reddish. Three major structures are presented in a normal human eye fundus photograph, the optic disc (or optic nerve head), the macula and

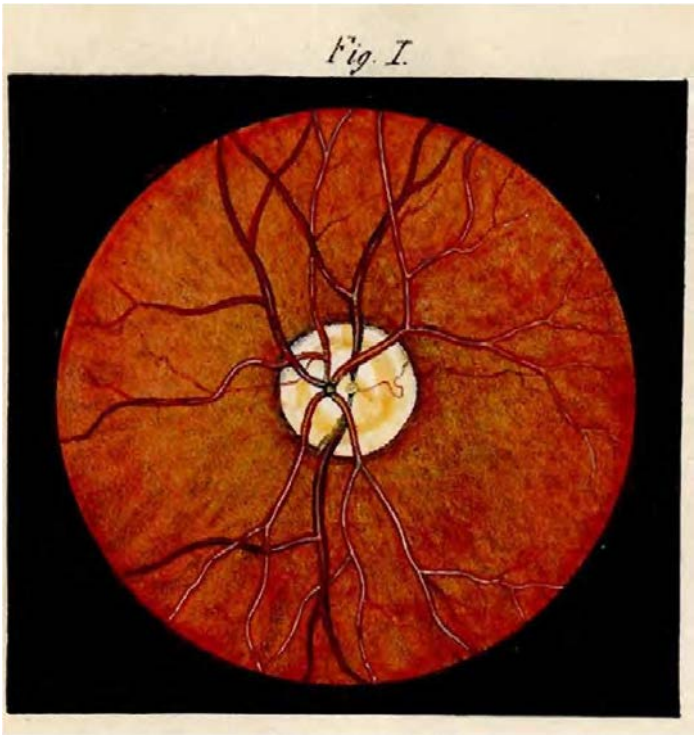

Figure 2.3: First known image of human retina as drawn by van Trigt in 1853 [3].

blood vessels. The optic disc appears to be a bright region in the image, where all blood vessels converge. Arteries are brighter comparing with veins. The macula is a dark region where few blood vessels present. Medical signs, such as hemorrhages, exudates, cotton wool spots, blood vessel abnormalities, and pigmentation can be detected using fundus photographs.

Fundus photography is still the most cost-effective image modality clinically. It is also commonly used in screening programs, where the photos can be analyzed later for diagnosis and be used to monitor the progress in many diseases. In a screening program, where thousands of fundus photographs are taken, it is impossible for the ophthalmologists to personally exam every photo, especially in the extremely labori-

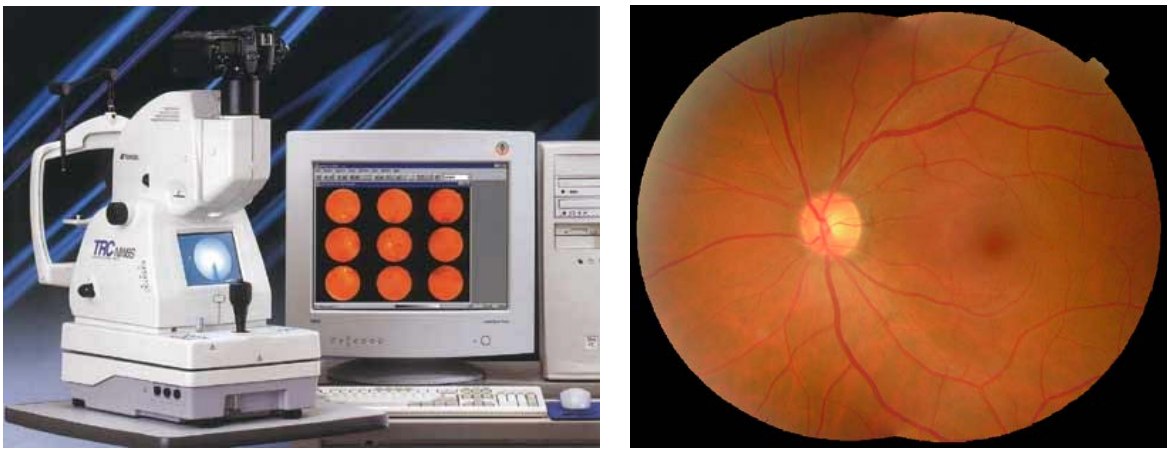

(a) (b)

Figure 2.4: Fundus camera and fundus photograph. (a)Fundus Camera [4]. (b)A Normal Eye Fundus Photograph.

ous work such as measuring vessel width for every vessel segment. Semi-automatic methods have already been introduced to partially relieve the problem [14]. But it is still not enough, especially in screening programs and some population studies where usually at least hundreds of fundus images are involved.

2.2.2 Other Optical Imaging Modality

- **Fluorescein angiography** is an intravenous imaging technique for examining the circulation of the retina using the dye tracing method [5]. Though the imaging technique is still fundus camera, it is an invasive method that involves injection of sodium fluorescein into the systemic circulation. An angiogram is obtained by photographing the fluorescenece emitted after illumination of the retina with blue light at a wavelength of 490 nanometers. Fluorescein angiography is a commonly used technique but it has a large number of side effects,

including nausea in one fifth of patients and in come cases death from anaphylaxis [15].

- **Ocular ultrasound** is an imaging technique that uses high-frequency sound waves that can be used instead of light to create an image of the retina and the surrounding structures [16]. The technique is used to identify complications of diabetic retinopathy including vitreous traction, retinal detachment and blood beneath the retina.
- **Scanning laser ophthalmoscopy** (SLO) uses the technique of confocal laser scanning microscopy for diagnostic imaging of retina or cornea of the human eye [15]. SLO utilizes horizontal and vertical scanning mirrors to scan a specific region of the retina and create raster images. SLO makes it possible to ensure sharp and detailed images because of the short illumination period.
- **Optical Coherence Tomography (OCT)** is a powerful clinical tool for monitoring retinal physiology in patients. It utilizes low coherence interferometry to differentiate tissues within the eye and create a cross section of a living patient's retina in a non-invasive way. The use of relatively long wavelength (near-infrared) light allows it to penetrate into the scattering medium (e.g., biological tissue). It is worth noting that OCT is not only used in ophthalmology, it can also be employed in diverse areas, including art conservation and interventional cardiology to help diagnose coronary artery disease [17].

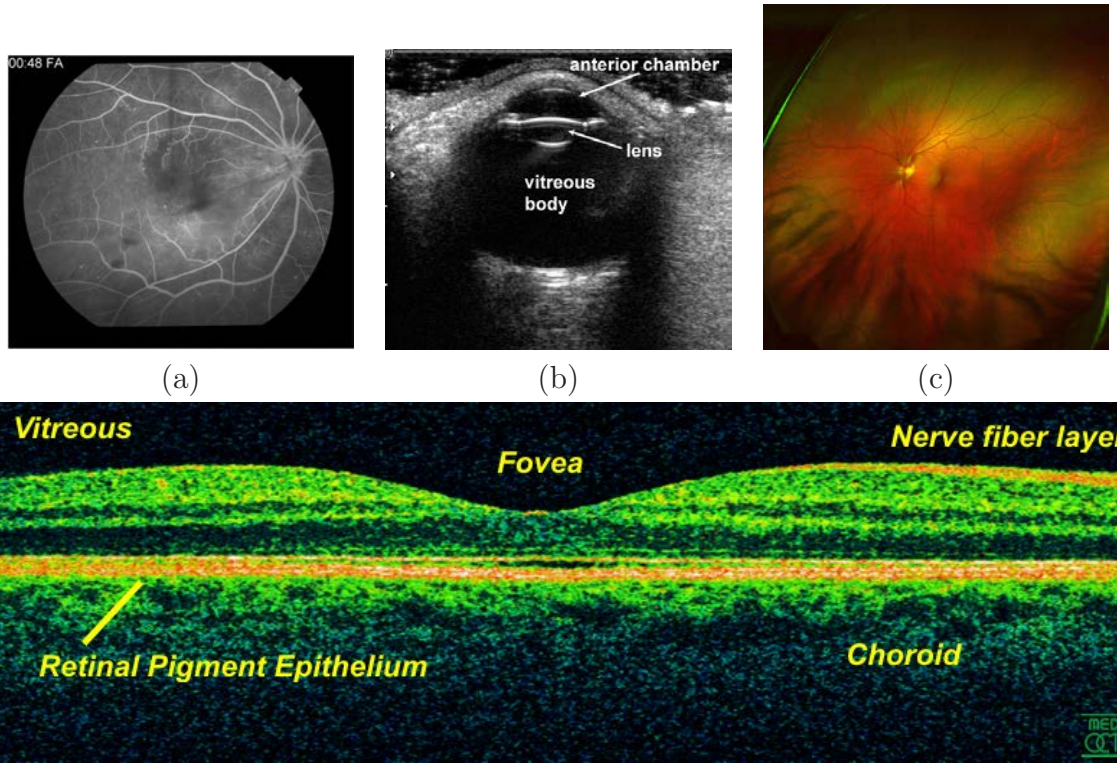

(a) (b) (c)

(d)

Figure 2.5: Example figures of multiple ophthalmologic imaging techniques. (a) Peak phase angiogram in a patient with diabetes demonstrates areas of hyporfluorescence in the superior macula secondary to a vascular filling defect as well as hyperfluorescent microaneurysms [5]. (b) Ocular ultrasound: Ultrasound image of a normal eye with lens [6]. (c) Scanning laser ophthalmoscope image of the left eye retina (image courtesy to Michael Judge Brislin). (d) OCT scan of a retina at 800 nm with an axial resolution of 3 μm [7].

2.3 Retinal Vascular Changes and Related Diseases

Retinal blood vessel changes have been reported to be associated with a number of diseases. Retinal arteriolar changes and venular changes have been reported to be associated with different diseases [18][8][19][13]. The retinal arteriolar narrowing is mainly associated with hypertensive retinopathy. The pathophysiological changes in retinal vessels in response to blood pressure elevation are often referred to as hy-

pertensive retinopathy. The main vascular changes in hypertensive retinopathy is seen clinically as generalized narrowing of the retinal arterioles [20]. Less is known about the pathophysiological mechanisms of retinal venular caliber changes. Epidemiological studies have consistently shown associations of retinal venular caliber with systemic inflammatory markers [19]. Retinal venular widening is also reported to be associated with smoking, hyperglycemia, obesity, and dyslipidemia [8]. In a population-based study of normal Australian children with a mean age of 12.7 years, those in the highest quartile of blood pressure had significantly narrower mean retinal arterial diameters ($p < 0.0001$) after adjustment for age, gender, ethnicity, height, birth, weight, BMI and iris color [21]. Children in the highest quartile of BMI had significantly increased venous caliber ($p = 0.001$) and significantly decreased arteriolar caliber ($p = 0.01$) [21, 22]. In another cross-sectional study of children aged 7 to 9 years, increased BMI was associated with increased venous caliber, but not with decreased arterial caliber, after adjustment for age, gender, race, socioeconomic status and birth parameters [23].

The retinal vessel width relationship at vessel branching points in fundus images is another important biomarker of retinal and systemic disease, such as periventricular white matter hyperintensities, ischaemic heart disease, and hypertension [24, 20]. The retinal arterial diameters at branching points conform to predicted optimal values in normal subjects, but deviate significantly in men with peripheral vascular diseases [25]. Studies also showed that the retinal branch point exponents deviate from optimal values with advancing age [26]. Increased branching coefficient

of retinal vessels was also reported to be associated with periventricular white matter hyperintensities and ischaemic heart disease, and decreased branching coefficient with deep white matter hyperintensities [24]. Compared to straight vessel segment width as a parameter, the width ratio at branch points has the obvious advantage that it is dimensionless, which allows the difference in magnification by the optics of the eye across individuals, so that the ratio can be compared across subjects [13, 27].

2.3.1 Methodological Issue in Measuring Retinal Vascular Changes

A number of quantitative analysis has been made on the fundus images as an indicator of those changes, including the retinal arteriole-venule ratio (AVR), parent branch-daughter branch relationship, vascular bifurcation angles, vascular tortuosity, and length-to-diameter ratios [11]. Among these parameters, parent branch-daughter branch relationship and arterial-to-venous ratio are closely related with retinal vessel width measurement and they are closely related with each other as well. A discussion of previous works on those two parameters is given below.

- **Parent Branch-Daughter Branch Relationship**

In 1926, Murray proposed the parent branch-daughter branch relationship that required minimum expenditure of energy by the organism in arteries and in capillaries. Murray argues that larger vessels lower the energy expended in pumping blood, while larger vessels also increase the overall volume of blood in the system, which will in turn requires more metabolic support. So In order to minimize the expenditure of energy, the parent branch and daughter branches should follow the relationship given

in Equation 2.1.

$$d^3 = d_1^3 + d_2^3, \tag{2.1}$$

where d is the caliber of parent branch and d_1, d_2 are the calibers of two daughter branch. In 1995, Stanton *et al.* followed Murray's study on the parent branch-daughter branch relationship in human retina on a set of 25 subjects by manually measuring the branching vessel width of arteries [26]. However, they concluded that the junction exponents (value of x in Equation 2.1) were 2.65±0.18 for normotensive and 2.48±0.17 for hypertensive subjects.

On the other hand, Parr et al. proposed the arterial parent branch-daughter branch relationship in human retina in the form of a second power polynomial relationship [20], as given in Equation 2.2. The study included 40 subjects and 126 arterial branchings. All branch vessel width were manually measured. The proposed relationship was concluded by doing a linear fitting.

$$W_a = (0.87w_1^2 + 1.01w_2^2 - 0.22w_1w_2 - 10.76)^{1/2}, \tag{2.2}$$

where w_1, w_2, and W_a are the widths of the narrower branch, the wider branch, and the parent trunk in an arteriolar branching. This described relationship applies only to normal vessels of young subjects. There may be different relationships for normal vessels of old subjects and for abnormal vessels.

In 1999, Hubbard et al. proposed a similar relationship for retinal venous branch points, as given in Equation 2.3.

$$W_v = (0.72w_1^2 + 0.91w_2^2 + 450.05)^{1/2}, \tag{2.3}$$

where w_1, w_2, and W_v are the widths of the narrower branch, the wider branch, and the parent trunk in a venular branching.

In 2003, Knudtson *et al.* argued that the Parr-Hubbard formulas have some spurious variability [28]. First of all, these calculations allow contributions of a variable number of vessel diameters for each eye to the overall estimate of vessel caliber, which resulted in increasing trends between the number of vessels included in the calculation and the magnitude of summary estimates. Secondly, the formulas include constant terms in their equations, which in turn cause the result to be dependent upon the units (e.g. microns, pixels) of the measurement. They therefore developed the revised formulas for summarizing the caliber of arterioles and venules, which is given in Equation 2.4 and 2.5.

$$\hat{W}_a = 0.88 \times (w_1^2 + w_2^2)^{1/2} \tag{2.4}$$

$$\hat{W}_v = 0.95 \times (w_1^2 + w_2^2)^{1/2}, \tag{2.5}$$

where $\hat{W}_a$ and $\hat{W}_v$ is the widths of the trunk of an arteriolar branching and a venular branching separately and w_1 and w_2 is the widths of the two branches.

All the studies are based on manual measurement and very limited number of subjects and branch points. Until now, no large scale study has been done to explore the parent branch-daughter branch relationship due to the lack of a fully automated

retinal vessel measurement technique. Hence, no commonly accepted relationship is developed.

- **Arteriole-to-Venule Ratio**

The arteriole-venule ratio (AVR) is another commonly used measurement, because it is simple to understand and is attractive to clinicians, and because correction for refractive error is not needed [19]. Figure 2.6 shows two retinal images as examples of low and high arteriole-venule ratio [18].

Figure 2.6: Examples of low and high arteriole-venule ratio [8].

Even though the concept of AVR is very straightforward, the calculation is not easy. The variation among individuals of the number of branches and pattern of branches makes it no straightforward quantitative way to express the general caliber

of the retinal vessel [29]. Because at a bifurcation, although each branch is usually narrower than its parent, the total cross-sectional area of the vascular bed increases [20].

Parr *et al.* proposed the concept of the central retinal artery equivalent (CRAE) in 1974 [29]. They use Equation 2.2 to calculate the width of a parent vessel from the widths of its two branches. This procedure is done iteratively until a single arterial branch is reached, which is called the central retinal artery equivalent (CRAE).

Similarly, in 1999, Hubbard *et al.* proposed the concept of central retinal vein equivalent (CRVE) and a parent branch-daughter branch relationship to calculate CRVE [14]. The formula is given in Equation 2.3. Similarly, the parent branch-daughter branch relationship equation is used to calculate the caliber of parent branch using the calibers of two daughter branches until a single venous branch is reached.

Knudtson proposed to used the revised Parr-Hubbard equations (Equation 2.4 and Equation 2.5)to calculate CRAE and ARVE. However, only the six largest arterioles and the six largest venules are included in the calculation. They used an iterative procedure of pairing up the largest vessels with the smallest vessels and repeating until they reached a single number, which is still called a central retinal vessel equivalent.

A more recent work of Patton *et al.* proposed a formula using a linear regression model to incorporate the asymmetry index of the vessel branches being measured [30]. However, they did not provide a comparison between their proposed formulas

and the Parr-Hubbard formulas and Knudtson's revised formulas.

The current arteriole-venule ratio measurement method has been reported to have significant limitations. As mentioned, narrowing retinal arterioles and widening venules has been reported to be associated with different systemic diseases. Smaller retinal arteriolar caliber is associated with hypertension, while larger retinal venular caliber has been associated with inflammation, smoking, hyperglycemia, obesity, and dyslipidemia [8]. However, the current arteriole-venule ratio measurement is unable to separate those different changes in arterioles and in venules. Furthermore, the AVR is constructed by producing a formula that convert the AVR into a single ratio number (CRAE/CRVE). Thus it is unable to differentiate the AVR changes across the image at different branching levels. There are reports shown that in some conditions, such as hypertension, it is the smaller arteries that may be most affected [29]. But the current AVR is not able to show these differences.

CHAPTER 3
AUTOMATED LOCALIZATION OF RETINAL LANDMARKS

3.1 Literatures

A knowledge of the location of the optic disc and fovea will benefit the fundus image analysis in many aspects. This is important for two reasons. First, it is often necessary to mask out the normal anatomy before finding abnormal structures. For instance, the optic disc might be mistaken as bright lesion if it is not masked out. Secondly, the distribution of the abnormalities is not uniformly distributed on fundus photographs. Certain types of abnormalities occur more often in specific areas on the retina. In the conventional study of arteriole-venule ratio, the arteriole-venule ratio is usually measured around a circular region centered at the optic disc [28]. It is also known that hypertensive retinopathy has a larger influence on the smaller retinal vessels, which are usually far away from the optic disc [20]. Thus a advance knowledge of the location of the optic disc is required.

A lot of work has been reported in the optic disc or fovea detection [31] [32] [33] [34] [35] [36] [37] [38]. Most optic disc detection methods are based on the fact that the optic disc is the convergence point of blood vessels and it is normally the brightest structure on a fundus image. Most fovea detection methods depend partially on the result of the optic disc detection.

Hoover *et al.* proposed a method for optic disc detection based on the combination of vessel structure and pixel brightness [33]. If strong vessel converge point is

found in the image, it is regarded as the optic disc. Otherwise the brightest region is detected. Foracchia *et al.* proposed an optic disc detection method based on vessel directions [32]. A parabolic model of the main vascular arches is established and the model parameters are the directions associated with different locations on the parabolic model. The point with a minimum sum of square error is reported as the optic disc location. In Lowell *et al.*, by matching an optic disc model using the Pearson correlation, an initial optic disc location is determined [35]. Then a deformable contour model was used to trace the optic disc boundary.

Compared with the automatic detection of optic disc, less work has been done in the field of fovea detection. Most methods use the fact that the fovea is a dark region in the image and that it normally lies in a specific location relative to the optic disc and the main vascular arch. In Flemming, approximate locations of the optic disc and fovea are obtained using the elliptical form of the main vascular arch [31]. Then the locations are refined based on the circular edge of the optic disc and the local darkness at the fovea. Li and Chutatape also proposed a method to select the brightest 1% pixels in a gray level image [34]. Then the pixels are clustered and principal component analysis based on a trained system is applied to extract a single point as the estimated location of optic disc. A fovea candidate region is then selected based on the optic disc location and the main vascular arch shape. Within the candidate region, the centroid of the cluster with the lowest mean intensity and pixels number greater than 1/6 disk area is regarded as fovea location. In Sinthanayothin's paper, the optic disc was located as the area with the highest variation in intensity

of adjacent pixels, while the fovea was extracted using intensity information and a relatively distance to the optic disc [37]. Tobin *et al.* proposed a method to detect the optic disc based on blood vessel features, such as density, average thickness and orientation [38]. Then a fovea location is determined based on the location of optic disc and a geometry model of the main blood vessel. Niemeijer *et al.* proposed a method to automatically localize both the optic disc and fovea in 2008 [36]. For the optic disc detection, a set of features are extracted from the color fundus image. A k-nearest-neighbor classification is used to give a soft label to each pixel on the test image. The probability image is blurred and the pixel with the highest probability is detected as optic disc. A relative position information between the optic disc and the fovea is used to limit the search of fovea into a certain region. For each possible location of the optic disc, a possible location of the fovea is given. The possible locations for the fovea is stored in a separate image and the highest probability location is detected as the fovea location. The simultaneous detection of optic disc and fovea proposed in this thesis is an extension of the work of Niemeijer *et al.*

3.2 Methodology

The algorithm for simultaneous detection of the optic disc and the fovea is an extension of the work of Niemeijer *et al.* [36]. Part of the work has already been published [39].

In order to extract the intensity information from different color channels, the red, green and blue channels are extracted from the color fundus image (Figure

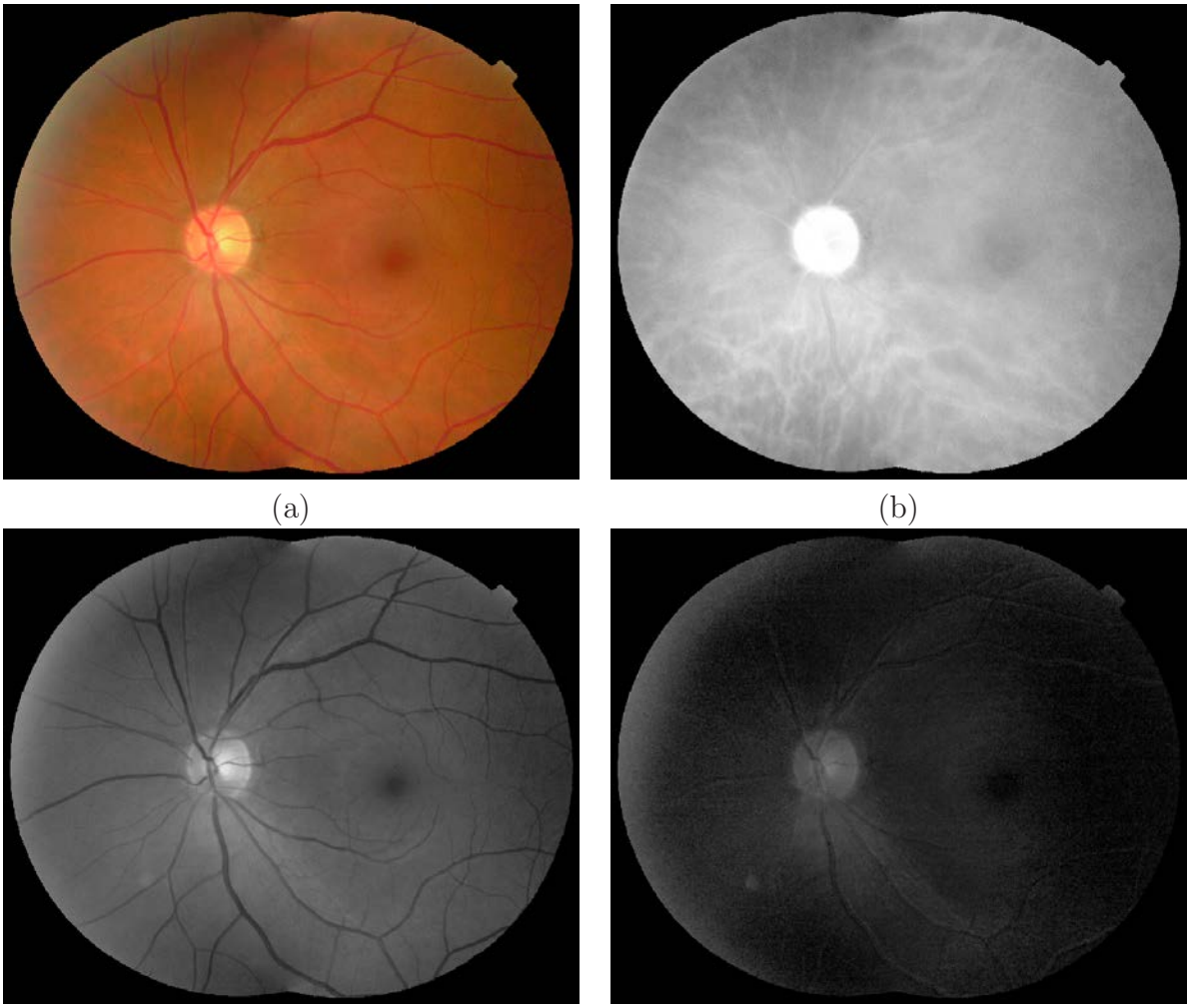

Figure 3.1: RGB channels of Figure 2.5. (a)Color fundus image. (b)Red channel. (c)Green channel. (d)Blue channel.

3.1). The green component allows the best contrast between retinal vessels and background. The red channel is usually saturated while the blue component is very dark and contains lots of noise. We extract features from all three channels and let the feature selection decide which features are useful later.

As mentioned in Section 2.1, the optic disc is the convergence point of blood vessels. The fovea center has very few blood vessels. Consequently, blood vessel

features such as vessel width, orientation, etc. can be used as indicator of the optic disc and fovea positions. In order to measure vessel features, a vascular segmentation is required. We applied the vessel segmentation method proposed by Niemeijer *et al.* [9]. This segmentation method is trained using a set of images in which all vasculature has been manually segmented. A posterior probability map was produced with each pixel's gray value being the probability of this pixel being a vessel pixel. An example of the probability image is shown in Figure 3.2.

The probability image is then thresholded to generate a binary vessel segmentation image. The threshold is set to 110 in this study so that big blood vessels can be maintained while small branches and noise are discarded. In the binary vessel image, a pixel value of 255 indicates that it is a vessel pixel while 0 indicates it is a background pixel.

The centerlines of blood vessels are extracted from this binary image through sequential thinning approach [40]. The structuring element E and L used in sequential thinning are shown in Equations 3.1 and 3.2. $*$ means the pixel at that position can be either 0 or 1. The other five elements are given by rotation.

$$E_1 = \begin{bmatrix} * & 1 & * \\ 0 & 1 & 0 \\ 0 & 0 & 0 \end{bmatrix}, \quad E_2 = \begin{bmatrix} 0 & * & * \\ 0 & 1 & 0 \\ 0 & 0 & 0 \end{bmatrix}, \cdots, \quad E_7 = \begin{bmatrix} * & 0 & 0 \\ * & 1 & 0 \\ 0 & 0 & 0 \end{bmatrix} \tag{3.1}$$

$$L_1 = \begin{bmatrix} 0 & 0 & 0 \\ * & 1 & * \\ 1 & 1 & 1 \end{bmatrix}, \quad L_2 = \begin{bmatrix} * & 0 & 0 \\ 1 & 1 & 0 \\ * & 1 & * \end{bmatrix}, \cdots, \quad L_7 = \begin{bmatrix} 0 & 0 & * \\ 0 & 1 & 1 \\ * & 1 & * \end{bmatrix} \tag{3.2}$$

Sequential thinning is defined as Equation 3.3. Let $B_{(1)}, B_{(2)}, ..., B(n)$ denote the

(a)

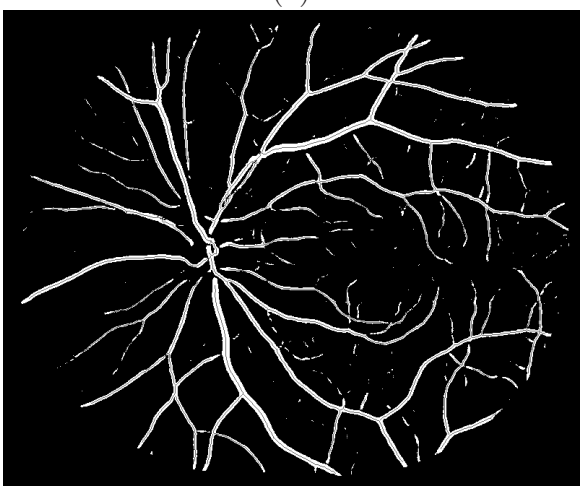

(b)

Figure 3.2: Vessel probability image and vessel centerline image of Figure 2.5. (a)The vessel probability image. (b)The final binary image with centerline pixel inside.

structuring elements E and L mentioned above. $X \ominus B$ means erode X with element B. $X \ominus B = p \in \varepsilon^2$: $p = x + b \in X$ for every b $\in B$.

$$X \ominus B_{(i)} = (((X \ominus B_{(1)}) \ominus B_{(2)}) ... \ominus B_{(n)}) \tag{3.3}$$

The centerline image are then added back to the binary image and gives a gray

value of 100, in order to distinguish from the vessel pixels, which is 255. An example image is shown in Figure 3.2.

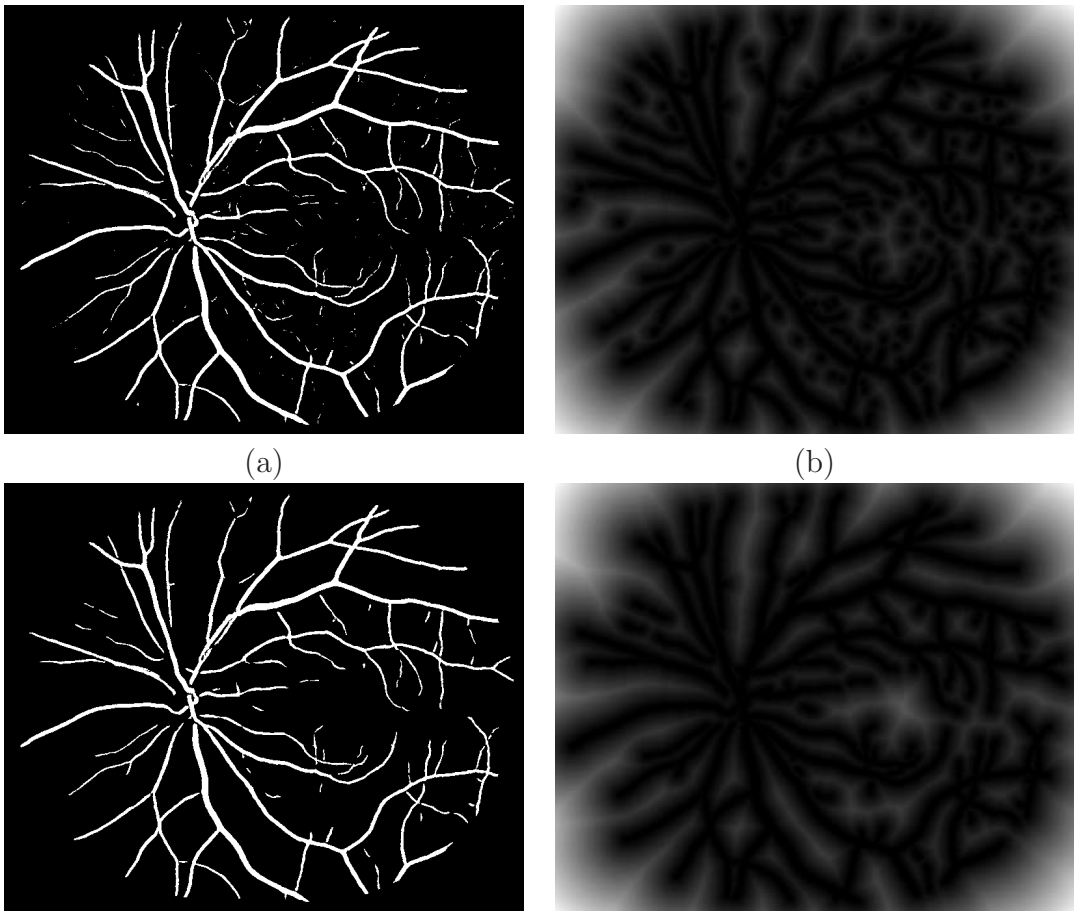

Figure 3.3: Distance transform of Figure 2.5. (a)The binary image before erasing noise regions. (b)The distance map of (a). It is influenced by small noises greatly. (c)The binary image after erasing noise regions. (d)The distance map of (c). The influence by noise regions disappears.

As mentioned, usually no blood vessel can be observed around the fovea, while lots of vessels are around the optic disc since it is the convergence point of blood vessel.

Therefore, a distance transform of the binary vessel segmentation image is generated to make use of this observation (see Figure 3.3). The brightness of a pixel denotes its distance to the nearest blood vessel pixel. So the blood vessel pixels have a brightness 0 because it has a distance 0 to blood vessel. The optic disc region normally has a very low average brightness, because of a high blood vessel density. The four corners and the fovea region are usually much brighter because of the absence of vessel pixels.

However, if we use the binary image directly to generate the distance image, the distance map will be influenced by small noise, as shown in Figure 3.3 (a) and (b). If there are small noises around the fovea, the distance image will be changed greatly. In order to solve this problem, the vessel regions that have an area smaller than 20 pixels are erased from the binary blood vessel image. As shown in Figure 3.3 (c) and (d).

3.2.1 Feature Extraction

For each sample point, a set of features are extracted from the pre-processed images. A circular template is used to extract those features (see Figure 3.4). The outer diameter $\mathcal{R}$ is set to 50 pixels because it is comparable to the diameters of the optic disc and fovea. The inner diameter r of the template is designed to best obtain the intensity contract between the center of the fovea and the peripheral. In our study, we empirically chose the inner radius 25 pixels. Since the optic disc is the entry point for the optic nerve, for pixels around the optic disc, all the vessel segments should oriented to the template center. Also, despite the few numbers, the vessels

that approach the fovea center from the top and bottom directions are expected to be more or less parallel to the y-axis, while the vessels approaching from the left and right should approximately be parallel with the x-axis. Based on this observation, the template is also divided into four quadrants, in order to better capture the vessel orientation differences in different directions.

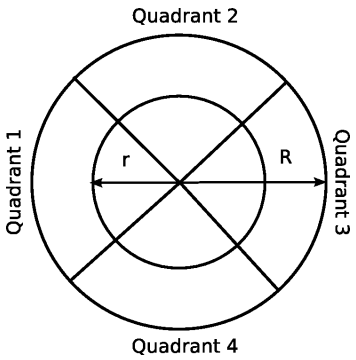

Figure 3.4: Circular template of inner radius r and outer radius $\mathcal{R}$. The template is divided into four quadrants.

The features extracted from the pre-processed images are shown in Table 3.2.1. Among these features, feature 1-30 is extracted from the vessel probability map. Feature 31-42 are extracted from the red, green and blue channel. Feature 43-45 are from the distance transform image of the binary image.

Figure 3.5 shows an simple illustration of how the vessel features are calculated within the template. The template radius is 15 pixels. The inner template boundary is not shown because it is not used in vessel feature extraction. Pixel 1 denotes the template center.

Table 3.1: Features extracted for the first k-NN classification.

feature #	feature description	template	image
1-4	number of vessels	quadrants	vessel image
5-8	average vessel width	quadrants	vessel image
9-12	standard deviation of vessel width	quadrants	vessel image
13-16	average vessel orientation difference	quadrants	vessel image
17-20	standard deviation of vessel orientation difference	quadrants	vessel image
21-24	maximum vessel width	quadrants	vessel image
25-28	orientation difference of max-width vessel	quadrants	vessel image
29	vessel density	whole template	vessel image
30	average vessel width	whole template	vessel image
31-36	average image intensity	inner/outer template	R,G,B image
37-42	standard deviation of image intensity	inner/outer template	R,G,B image
43-44	average distance to vessel pixel	inner/outer template	distance image
45	maximum distance to nearest vessel pixel	inner template	distance image

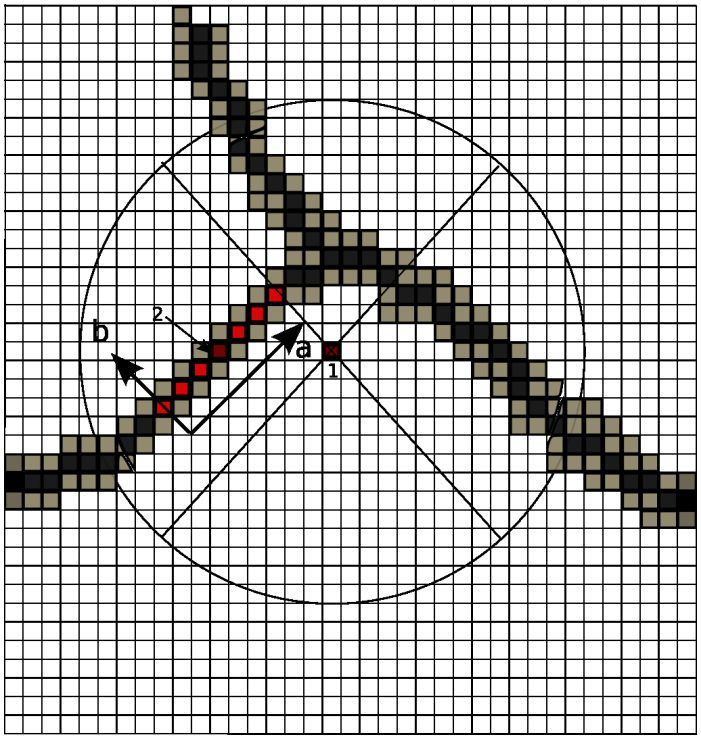

Figure 3.5: Illustration of how vessel features are computed. The outer radius of the template is 15 pixels. The inner radius is not shown because it is not used in vessel feature extraction. Vessel pixels are shown in gray and vessel centerlines are shown in black. Pixel 1 is the template center. Arrow a denotes the vessel orientation at pixel 2. Arrow b denotes the direction along which the vessel width is calculated.

Under each quadrant, the number of vessels is the number of vessel pixels under the quadrant. So the number of vessels for quadrant 1 is 27. Similarly, vessel number for quadrant 2, 3, and 4 is 39, 41 and 0 separately.

For each centerline pixel p, the three neighbor centerline pixels in the left and in the right are found. So a vessel centerline segment of length 7 is selected. Near the end of the vessel, where less than three neighbors can be found at one end, only centerline coordinates inside the vessel are used, 4 pixels for the end point. If the total length of the centerline segment is less than 4 pixels, it is regarded as noise and

discarded. For example, the 6 neighbors for pixel 2 are labeled red in Figure 3.5.

For this centerline segment, principal component analysis is applied to find the dominant orientation. The orientation is regarded as the orientation of centerline pixel p. In this example, the first principal component for the vessel segment centered at pixel 2 is $[0.707, 0.707]$, as shown in arrow a. The vessel angle is 45 degrees.

The vessel width at pixel p is measured along a line perpendicular to the dominant vessel orientation. In Figure 3.5, the vessel width is measured along arrow b. The vessel width at pixel 2 is two pixels.

After the vessel width and orientation is computed for each centerline pixel, the width average, width standard deviation, orientation average, orientation standard deviation and maximum vessel width can be calculated consequently.

$$\bar{x} = \frac{\sum_{i=1}^{n} x_i}{n} \tag{3.4}$$

$$s = \sqrt{\frac{1}{n-1}\sum_{i=1}^{n}(x-\bar{x})^2} \tag{3.5}$$

The vessel density under the complete template is measured by dividing the number of vessel pixels under the whole template by the area of the template. In the example shown in Figure 3.5, the total number of vessel pixels within the whole template is 107. The template area is $\pi\mathcal{R}^2 = 706$ pixels. So the vessel density is $107/706 = 0.15$.

The average vessel width under the whole template is calculated by dividing the number of vessel pixels by the number of centerline pixels. So in this example it is 107 divided by 34, which is 3.4. So the average vessel width is 3.4 within this

template.

The average and standard deviation of pixel intensities within the inner template and outer template are extracted separately on the red, green, and blue channels. The outer template radius $\mathcal{R}$ is set to 50, which is comparable to the radius of optic disc and fovea. Hence, if the template is centered around optic disc, the average intensity should be high while the standard deviation is supposed to be low, because of the low dispersion of image intensity. Similarly, around fovea, the average image intensity should be low and the standard deviation of intensity should also be low. Especially on the green channel, where optic disc, fovea, and blood vessels all have the best contract with the background. On the red channel, which is usually over saturated, the overall brightness is very high, often not only for the optic disc region; while on the blue channel, the overall brightness is usually very low, not only for the fovea region. But we still compute all those features and let the feature selection to decide which ones are useful. The equations for average and standard deviation is given in equation 3.4 and 3.5.

In this study, the radius of the inner template r is set to 25 pixels, because it gives a good intensity contract between the inner template and outer template when the template is centered around fovea.

The average distance to the nearest vessel pixel for both inner and outer templates are extracted from the distance image. On the distance image, the distance to the nearest vessel pixel is simply the pixel intensity. Near the optic disc, the distance image is usually very dark because of the high vessel density, while near the fovea

and four corners of the image, the distance image is usually very bright because of the absence of blood vessel.

In order to build a relationship between those features from sampling points with the true distance to optic disc and fovea, a distance variable $\mathcal{D}$ must be defined. First of all, for each sample pixel, the Euclidean distance to optic disc d_{od} and fovea d_f is calculated separately. Then dependent variable $\mathcal{D}$ is defined as follows:

$$\mathcal{D} = \begin{cases} d_f & \text{if} \quad d_f < R \\ 2R - d_{od} & \text{if} \quad d_{od} < R \\ R & \text{otherwise} \end{cases} \tag{3.6}$$

Parameter $\mathcal{R}$ is the radius of the outer template. $\mathcal{R} = 50$ in this study. Those pixels that are within 50 pixels to optic disc will have a d ranging from 50 pixels to 100 pixels, while those pixels that are within 50 pixels to fovea will get a d ranging from 0 pixels to 50 pixels. Since normally the distance between the optic disc and fovea in a fundus image is larger than 100 pixels, it is very unlikely for a pixel to fall in both side. Pixels that neither within $\mathcal{R}$ to optic disc or within $\mathcal{R}$ pixels to fovea will get a background value of 50 pixels. A true distance $\mathcal{D}$ map for Figure 3.1 looks like Figure 3.6.

After proposing all these potentially useful features, a feature selection method is necessary because all features are not necessarily helpful and may result in overdimensionality reducing optimization quality. Also, the more features used, the slower the system tends to be. What we need is a compact set of features that can separate the optic disc and fovea from the background and the blood vessels to the largest extent.

A sequential forward and backward selection method is adapted [41]. This

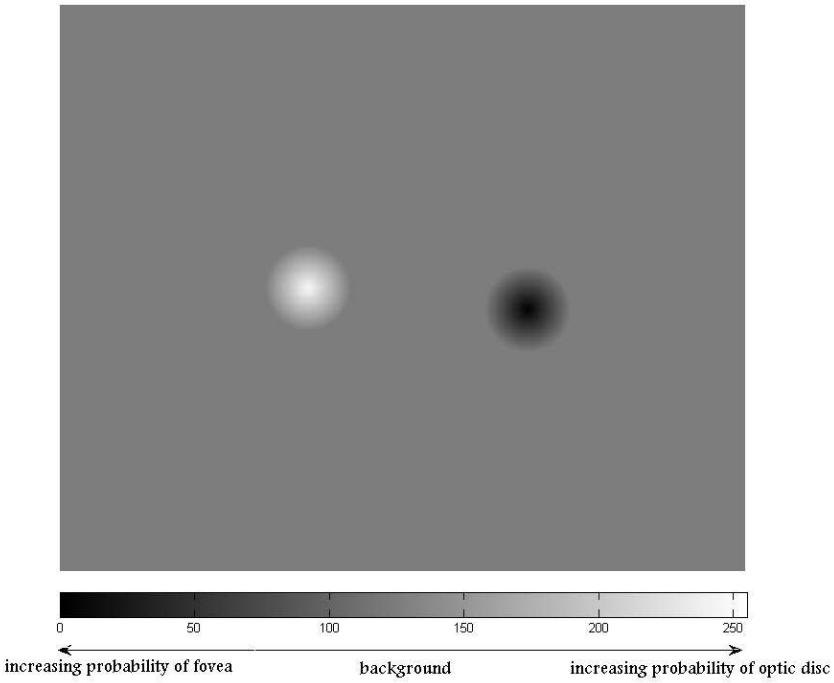

Figure 3.6: A standard true distance map for Figure 3.1. (a). The background is normalized to 127. The higher the gray value is, the higher the probability of being within an optic disc. The lower the gray value is, the higher the probability of being within a fovea.

algorithm employs a $plus\, l, take\, away\, i$ strategy. Stating with an empty feature set, l features with the best combined performance are selected one by one and then i features are subtracted from the chosen feature group if by subtracting those features, the overall performance is better. This procedure goes on until the maximum feature number or a satisfactory performance is reached.

In this study, the maximum feature number is set to 25. A larger number of feature will make the system very slow. The performance is measured as shown below.

Two criterion was proposed to measure the performance of the features. Cri-

terion one is the rate of correctness. Criterion two is the mean distance.

$$\mathcal{C}1 = \begin{cases} \frac{N_{od|t}+N_{f|t}}{\mathcal{M}+\mathcal{N}} & \text{if} \quad \mathcal{M} > 3000, \mathcal{N} > 3000 \\ 0 & \text{otherwise} \end{cases} \tag{3.7}$$

Where $\mathcal{M}$ denotes the predicted number of pixels within $\mathcal{R}$ pixels to optic disc center and $\mathcal{N}$ denotes the predicted number of pixels within $\mathcal{R}$ ($R = 50$) pixels to fovea center. $N_{od|t}$ and $N_{f|t}$ denotes the number of pixels that are really within $\mathcal{R}$ pixels of the optic disc or fovea. $\mathcal{C}1$ ranges from 0 to 1. $\mathcal{C}1 = 1$ means that all the pixels detected as optic disc or fovea pixels are truly optic disc or fovea pixels. $\mathcal{C}1 = 0$ indicates that none of the pixels detected as optic disc/fovea pixels are really optic disc/fovea pixel.

$\mathcal{M} > 3000, \mathcal{N} > 3000$ guarantees that the detected pixels is not too small. 50 images are used to do the feature selection. So this condition guarantees that approximately 60 pixels are detected as optic disc and 60 pixels are detected as fovea on each test image. Without this limitation, solely the criterion is meaningless. For an extreme example, if only 1 points are detected from the 50 test images and it is within 50 pixels of the optic disc, then $\mathcal{C}1 = 1$, which might imply a very good result. But in fact it is not, because it lack the ability to detect any point from most of the images.

$$\mathcal{C}2 = \begin{cases} \frac{\sum_{i=1}^{\mathcal{M}} dist_{i|od}+\sum_{j=1}^{\mathcal{N}} dist_{j|f}}{\mathcal{M}+\mathcal{N}} & \text{if} \quad \mathcal{M} > 3000, \mathcal{N} > 3000 \\ 0 & \text{otherwise} \end{cases} \tag{3.8}$$

Similarly, $\mathcal{M}$ and $\mathcal{N}$ denotes the predicted number of pixels within R pixels within optic disc or fovea. $\sum_i^{\mathcal{M}} dist_{i|od}$ denotes the true distance to the optic disc for all $i \in \mathcal{M}$. $\sum_j^{\mathcal{N}} dist_{j|f}$ denotes the sum of true distance to the fovea for all $j \in \mathcal{N}$.

$\mathcal{C}2$ ranges from 0 to $+\infty$. $\mathcal{C}2 = 0$ will imply that all $p \in \mathcal{M}$ are at the exact true location of the optic disc and all $p \in \mathcal{N}$ are at the exact true location of the fovea. The smaller the $\mathcal{C}2$ is, the better the performance.

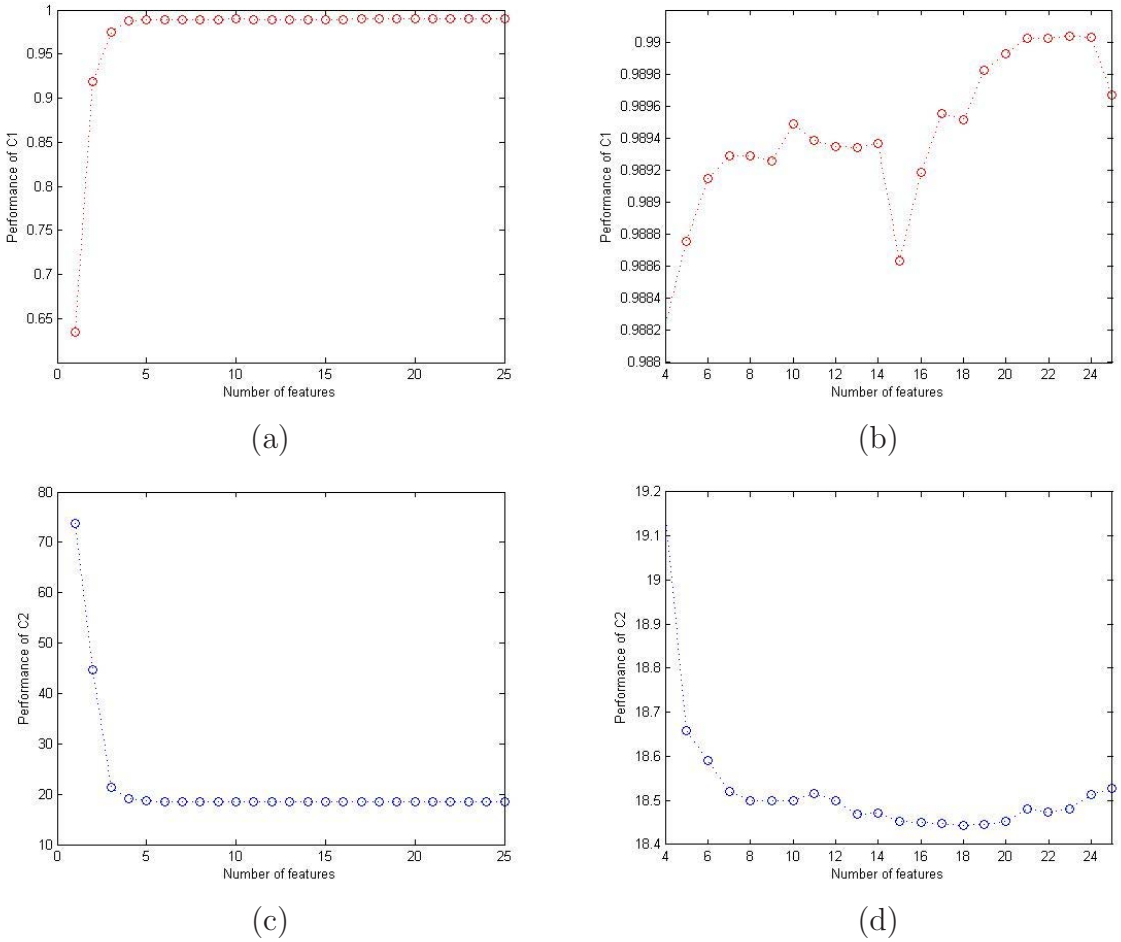

Figure 3.7: Feature selection with different criteria. (a)The performance of $\mathcal{C}1$ (1-25 selected features). (b)The performance of $\mathcal{C}1$ (4-25 selected features showing in details). (c)The performance of $\mathcal{C}2$ (1-25 selected features). (d)The performance of $\mathcal{C}2$ (4-25 selected features showing in details).

The feature selection results using two different criterion are shown in Figure

3.7. From the figures, we can see that, for both criterion, the performance fluctuates within a small range after five selected features. So even if the performance goes slightly better as more features are selected, the system becomes much slower. Also, too much features might cause over-fitting problems. So the first 11 selected features from both feature selections, which is a local maximum in $\mathcal{C}1$. The test results are shown in Figure 3.8.

From the test images, we can see that $\mathcal{C}1$ performs lightly better than $\mathcal{C}2$. It deals with the images better at the edge of the images and it can better distinguish the optic disc from the large blood vessel. So, the first 14 features from $\mathcal{C}1$ are used for final test. They are listed in Table 3.2.

In the 14 selected features, two of them are from the green channel, but no feature from the red or blue channel is selected. This again proofs that the green channel contains more information than the red channel and blue channel.

3.2.2 First k-NN Classification

During the training phase, the relationship is build between the selected feature and the dependent variable $\mathcal{D}$. For each training image, a rectangular grid of size $(2\mathcal{R})^2$ is centered at the optic disc and fovea separately. Inside the rectangular grid, the image is sampled densely for every 5 pixels, Then a number of 1000 sample points are randomly picked within the whole image. So a total number of 188,200 sample points are used to train the system. The circular template is placed on every sample point. The features are measured around the template and the dependent variable d

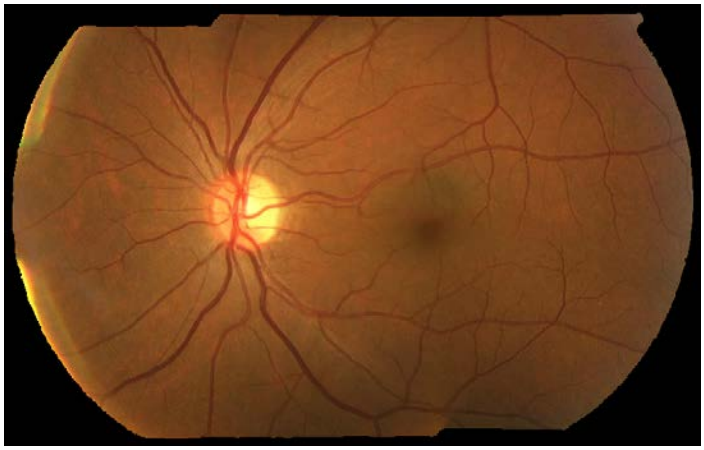

(a)

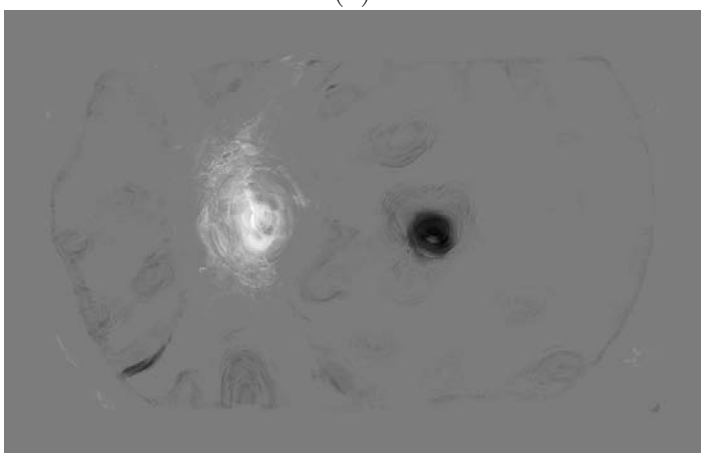

(b)

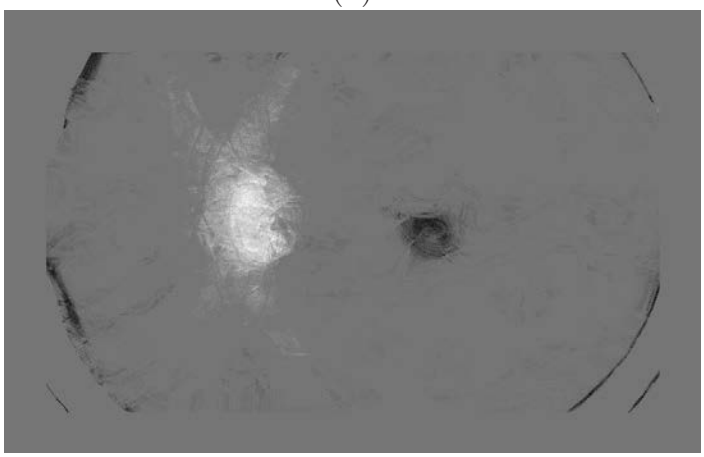

(c)

Figure 3.8: Criterion comparison. (a)Fundus image. (b)Result image using first 11 selected features from $\mathcal{C}1$. (b)Result image using first 11 selected features from $\mathcal{C}2$. $\mathcal{C}1$ performs better than $\mathcal{C}2$ at the image FOV boundary. For images (b) and (c), the background is normalized to 127. The higher the gray value is, the higher the probability of being within an optic disc. The lower the gray value is, the higher the probability of being within a fovea.

is calculated.

During test, the same set of features is measured for every pixel in the image. To estimate the distance d, the k nearest neighbors in the feature space are found and the values d of these nearest neighbors are averaged. k is chosen to be 11 in this study.

An simple illustration of how k-NN works is shown in Figure 3.9. In this simple example, the red circles denote optic disc pixels ($\mathcal{D} > 50$). The blue stars denote fovea pixels ($\mathcal{D} < 50$).The black triangles denotes background pixels ($\mathcal{D} = 50$). Green star is the test pixel. $k = 5$ is used. Three red circles, one blue star and one black triangle are found as the five nearest neighbors for the testing green star. Suppose the $\mathcal{D}$ associated with the five neighbors are 75, 70, 65, 50, 45 respectively. We can calculate the $\mathcal{D}$ associated with the testing green star to be $\frac{75+70+65+50+45}{5} = 61$.

After the first k-NN classification, a soft label is assigned to every pixel in the image. A value larger than 50 indicates that this pixel is likely to be an optic disc pixel. The larger the value, the higher the likelihood is. Similarly, a value smaller than 50 indicates a possibility of being a fovea center, the lower the pixel value, the larger the probability.

3.2.3 Second k-NN Classification

A first k-NN classification can give a good detection result for most cases. But when diseases appears or image quality is low, detection failures might occur. Within the detection failure cases, most of them have one structure, either optic disc or fovea,

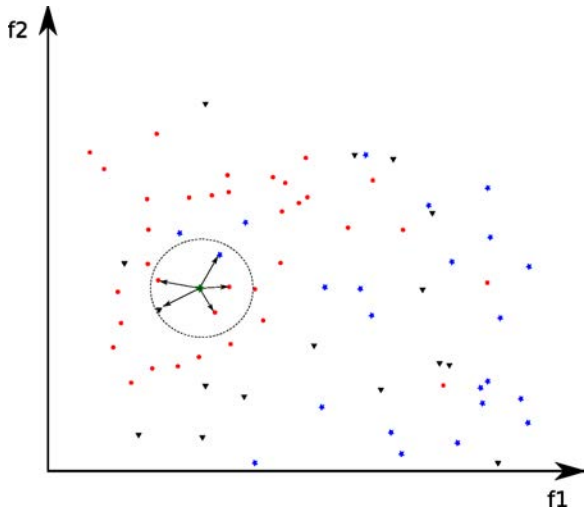

Figure 3.9: Illustration of k-NN regression. k=5 neighbors are found in this example. The red circles denote optic disc pixels ($\mathcal{D} > 50$). The blue stars denote fovea pixels ($\mathcal{D} < 50$). The black triangles denotes background pixels ($\mathcal{D} = 50$). Green star is the test pixel.

detection failed. The reason is usually that, there is some other areas has a higher probability than the true location does.

A second k-NN regression is applied to further enhance the result. During the first k-NN regression, the same set of features are applied to distinguish the optic disc and fovea from the other structures simultaneously. But no mutual information is included. Actually, in a fundus image, the distance between the optic disc and fovea as while as the angle between them has some potential patterns and might be used to enhance the detection result.

During training, for every pixel that is assigned as an optic disc/fovea pixel in the first stage, three more features are extracted from the probability image and a similar dependent variable d with is assigned to it.

During test, first the whole probability map is scanned and the maximum value

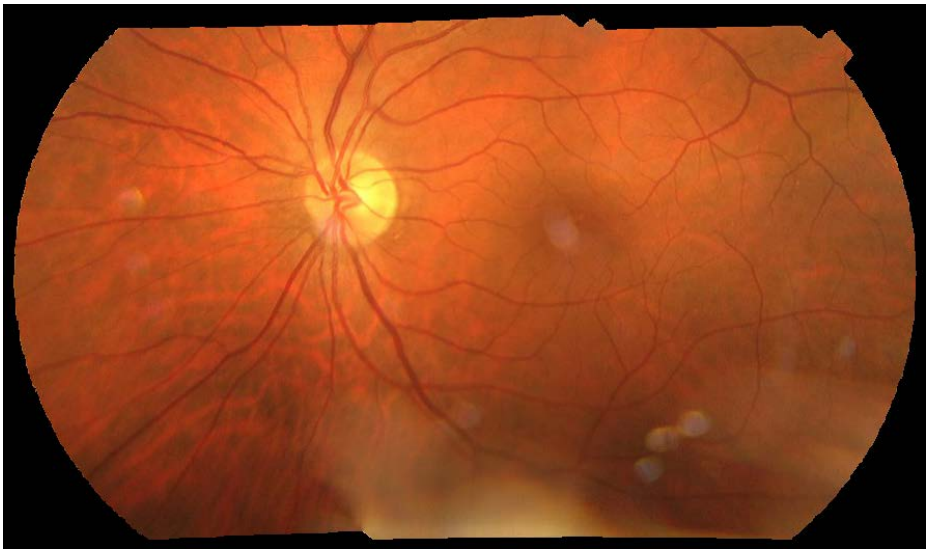

(a)

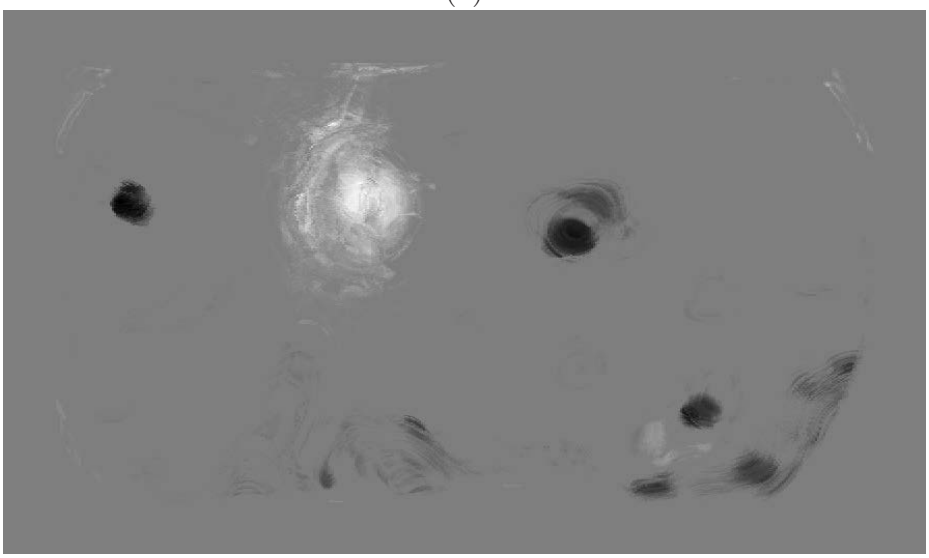

(b)

Figure 3.10: Example of first k-NN classification result. Two large regions on the image are labeled as fovea. The region on the left is falsely detected. (The background is normalized to 127. The higher the gray value is, the higher the probability of being within an optic disc. The lower the gray value is, the higher the probability of being within a fovea.)

and minimum value is stored as detected optic disc and fovea. Then same features as in training are extracted and a set of $k = 11$ nearest neighbors in the feature space are found. The corresponding d are averaged and assigned as a second probability label.

When the second k-NN regression is finished, it is combined with the first k-NN regression. For the pixels detected to be optic disc pixels, the probability is added to the first probability map to make the gray value even higher. While for those pixels detected to be fovea pixels, the gray value is subtracted from the first probability image to make the gray value even lower.

3.2.4 Image Post-processing

To find the optic disc and fovea, the final probability image is blurred, with a Gaussian kernel with $\sigma = 15$. This value is empirically determined. It dose not have a big influence on the final result. Finally, the pixel with the highest value is selected as the optic disc location and the pixel with the lowest value is selected as the fovea location.

3.3 Experimental Methods

Two hundreds normal fundus images of the left eye were used to train the system. One hundred and fifty of them were used for first k-NN training. Fifty images were used for feature selection. Fifty images were used for the second k-NN training.

A set of 479 fundus images with early diabetic retinopathy were used to test

the system. Two hundreds and forty of them are left eye images. Two hundreds and thirty nine of them are right eye images. The right eye images were manually identified and flipped before the test and the output images were flopped back.

During the first k-NN training and feature selection, the relationship between a set of features and the dependent variable $\mathcal{D}$ is built. For each training image, a rectangular grid of size $(2\mathcal{R})^2$ is centered at the optic disc and fovea separately. Inside the rectangular grid, the image is sampled densely for every 5 pixels, which is 882 sample points for both rectangular grids. Additionally, a number of 1,000 sample points are randomly picked within the whole image. In total, 1882 locations are sampled on each image, which is 188,200 sample points for the whole 100 training set.

For each sample point, the circular template is placed on it. The features are measured within the template and dependent variable $\mathcal{D}$ is calculated.

Image sampling during second k-NN regression is a little different. Instead of a densely sample plus random sample, the first probability image is thresholded at 170 and 80 separately. All pixels that have a gray value larger than 170 on the first probability image are picked for optic disc training. Similarly, all pixels that have a gray value smaller than 80 on the first probability image are picked for fovea training.

During test, in order to save running time, not every pixel on the image is measured. Intuitively a down-sample, up-sample method may be more preferable. But image down sample will change some features, of the image, such as vessel width, and vessel number. So features are only calculated for even column pixels. The odd

column will get a probability value through nearest neighbor interpolation.

Pixels within $\mathcal{D}$ pixels to the image boundary are not considered and labeled as background.

3.4 Results

Typical result images from the first k-NN classification is shown in Figure 3.11. The high gray value regions indicate the possible locations of the optic disc, while the low gray value regions indicate the possible locations of the fovea. The background is normalized to gray level 127.

Some good results will have only have one bright region and one dark region, like in case (a), (c), (d) (g) and (h). In these cases, the estimated locations will be accurate and clear. On the other hand, other cases might get more than one bright regions or dark regions, like in case (b), (e) and (f). Possible reasons include the presence of disease, low image contrast, artifacts or unbalanced illumination. Among those cases, it is possible to finally detect correct locations. However, this is not guaranteed. In some really bad cases as shown in (b), it is very hard to tell where the estimated fovea is.

In order to solve this problem, the second k-NN classification is introduced. The corresponding second k-NN results for images in Figure 3.11 is shown in Figure 3.12. The second k-NN classification includes certain mutual information between the optic disc and the fovea. Hence, it is able to only enhance the bright/dark regions that get support from the dark/bright regions. As shown in Figure 3.12, the image

cases (b), (e) and (f) can be handled very nicely. The misleading dark regions are suppressed.

The test database is constitutive of 103 left eye images and 207 right eye images with early sign of diabetic retinopathy. The general statistic results are shown in Table 3.4.

For all the 310 images, the mean distance error is 20.31 pixels with a standard deviation of 35.19 pixels for the optic disc. 98.1% estimated results fall in a circle with a radius of $\mathcal{R} = 100$ centered at the true location. 93.9% estimated results fall in a circle with a radius of $\mathcal{R} = 50$ pixel centered at the true location (as shown in Figure 3.14).

For the fovea, the mean distance error is 32.31 pixels with a standard deviation of 55.62 pixels. 95.8% estimated results fall in a circle with a radius of $\mathcal{R} = 100$ centered at the true location. 88.1% estimated results fall in a circle with a radius of $\mathcal{R} = 50$ pixel centered at the true location.

The histograms of the distance error is shown in Figure 3.13.

The correlated distance error is shown in Figure 3.14. Most of the points are located both within 50 pixels to the true location of the optic disc and 50 pixels to the true location of the fovea. The distance error for the fovea is slightly more dispersive than the optic disc. Most images only have one estimation error (if there is any), except for three outliers.

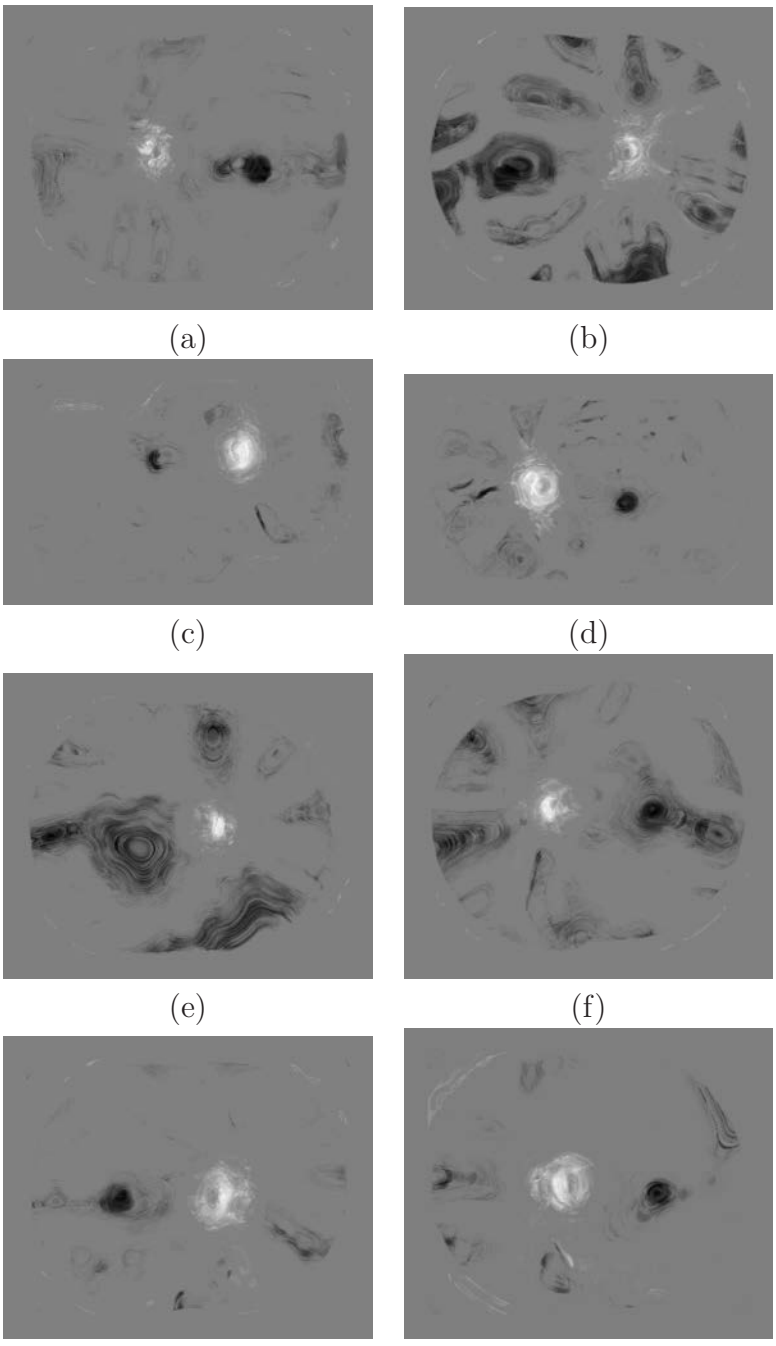

Figure 3.11: Examples of typical result of first k-NN classification. Each row shows a paired left eye and right eye result from the same person. The background is normalized to 127. The higher the gray value is, the higher the probability of being within an optic disc. The lower the gray value is, the higher the probability of being within a fovea.

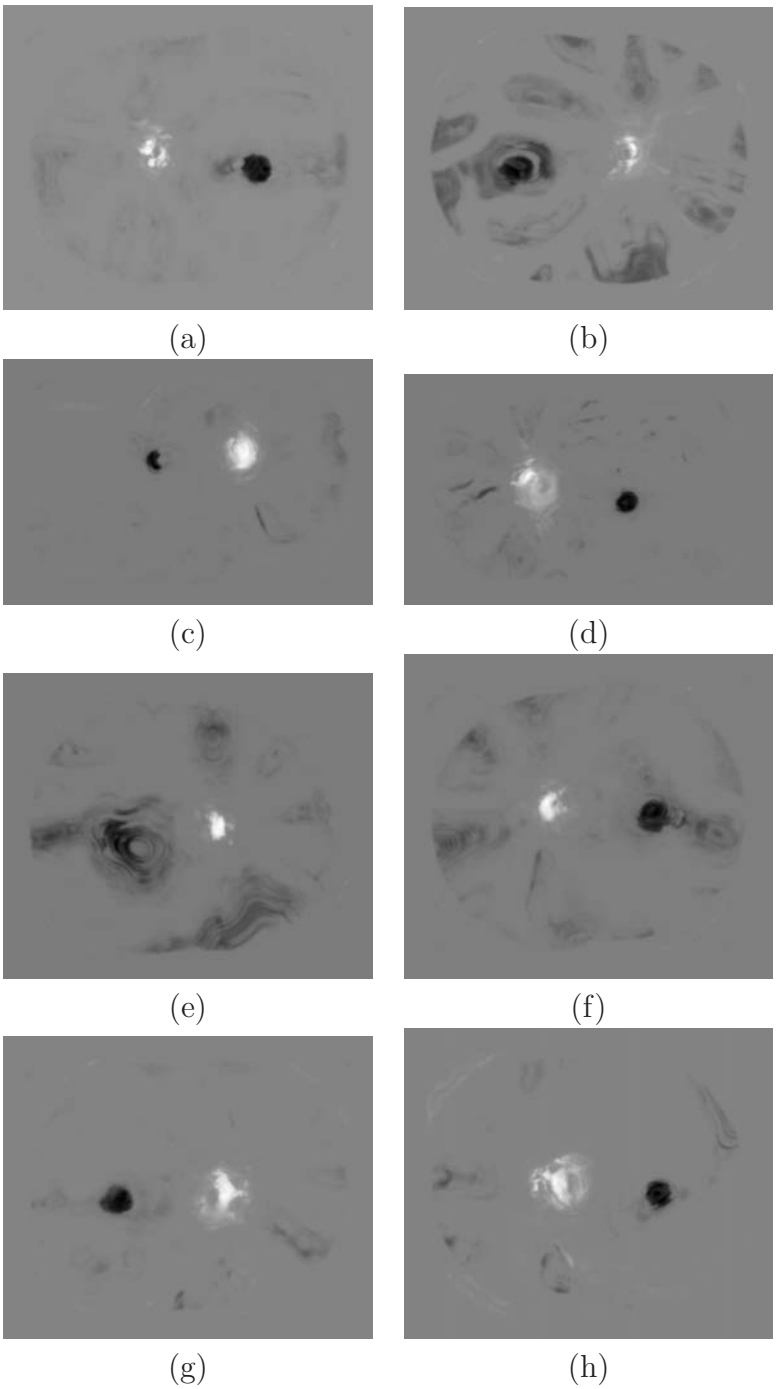

Figure 3.12: Examples of typical result of second k-NN classification. Each row shows a paired left eye and right eye result from the same person. The false responses has been suppressed. The higher the gray value is, the higher the probability of being within an optic disc. The lower the gray value is, the higher the probability of being within a fovea.

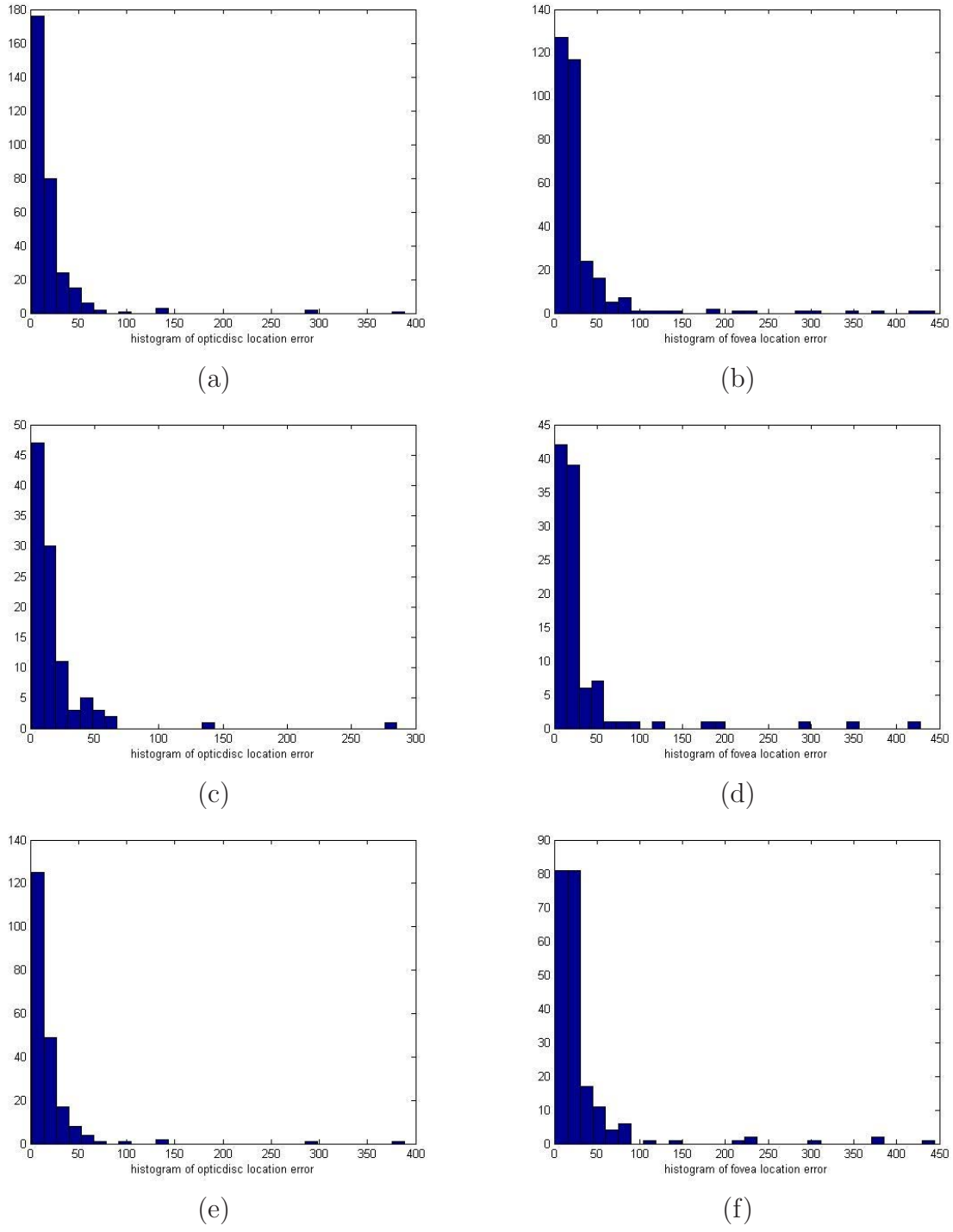

Figure 3.13: Histograms. Images (a),(b) are the general distance errors of the optic disc and fovea. Images (c),(d) are the distance errors of the left eye. (e), (f) are the distance errors of the right eye.

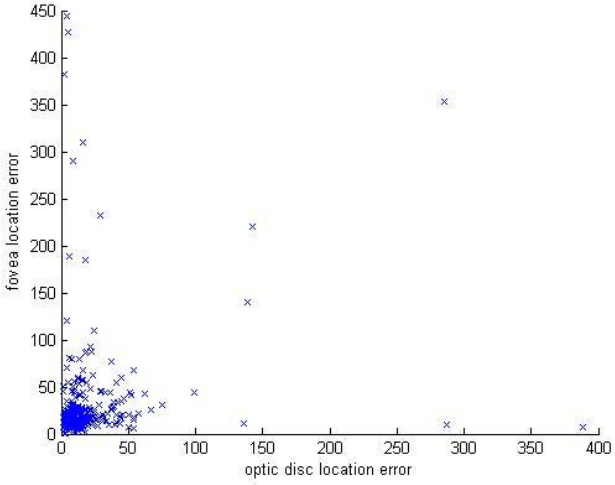

Figure 3.14: The correlated error of the optic disc and fovea for both eye images. The x-axis is the distance error of the optic disc. The y-axis is the corresponding distance error of the fovea.

3.5 Discussion

Method proposed in this thesis has several improvements comparing with previous work. First of all, the first stage of the detection is a simultaneous but independent detection of the optic disc and the fovea. The conventional way to detect both optic disc and fovea is to first detect the optic disc using some algorithm, and then detect the fovea depending on the result of the optic disc detection [31] [34] [37] [38]. The fovea detection could not provide any feedback to the optic disc detection. Our method achieves the independent but simultaneous detection of the optic disc and fovea using the same set of features.

Secondly, we then introduce the mutual information between the two structures to enhance the result. During the enhancement, the fovea detection is not depend on the optic disc detection. Neither does the optic disc detection depend

on the fovea detection. One structure is just given the right to adjust the detection of the other structure by putting more weight to the place that it believes to be the true location of the other structure. If the other structure is in an expected location, its probability of being the true location gets even higher. If it is not in an expected location, whether or not the algorithm accept this adjustment depends on the comparison between the originally detected location from the first stage and the enhanced location from the second stage. If the original detected location gives a stronger indication (i.e. higher probability) than the enhanced location from the second stage, the estimated location remains unchanged. On the other hand, if the enhanced location gives a stronger indication, the estimated location will move to the location suggested in the second stage.

Thirdly, new features are introduced for the classification. Features from the distance transform image, such as the average distance to the nearest blood vessel and maximum distance to the nearest blood vessel, were not used in previous work. We also tried to extract features from the red, green and blue channels. The feature selection result proves that the green channel contains more information than the other two channels on a color fundus photograph.

Image preprocessing includes getting the vessel probability images. Blood vessel features is a very important part of the feature set. Hence the quality of the vessel probability image will greatly influence the optic disc and fovea detection results. In other words, if the vessel probability image contains insufficient information, the detection result will be influenced largely.

Fig 3.15 shows some example vessel probability images and the optic disc and fovea detection results. The top row shows what a normal vessel probability image looks like and the corresponding optic disc/fovea probability image. The second row and last row show two bad cases where insufficient information is provided by the vessel probability image. Not surprisingly, the optic disc/fovea probability image is completely devastated. However, these results are actually very reasonable because the absence of vessel, i.e. low vessel density, is a very important property of the fovea area. That is why a large region is labeled dark if the vessel image implies so.

The image quality will effect the detection result greatly. If severe diseases or flaws appear on the image, it will influence the result. Our method is capable of handle some of the low quality images or images with severe diseases. Fig. 3.16 shows some cases with low quality images and their result.

But there are also cases that our method fails to detect the correct locations on the low quality images. Some examples are shown in Fig. 3.17.

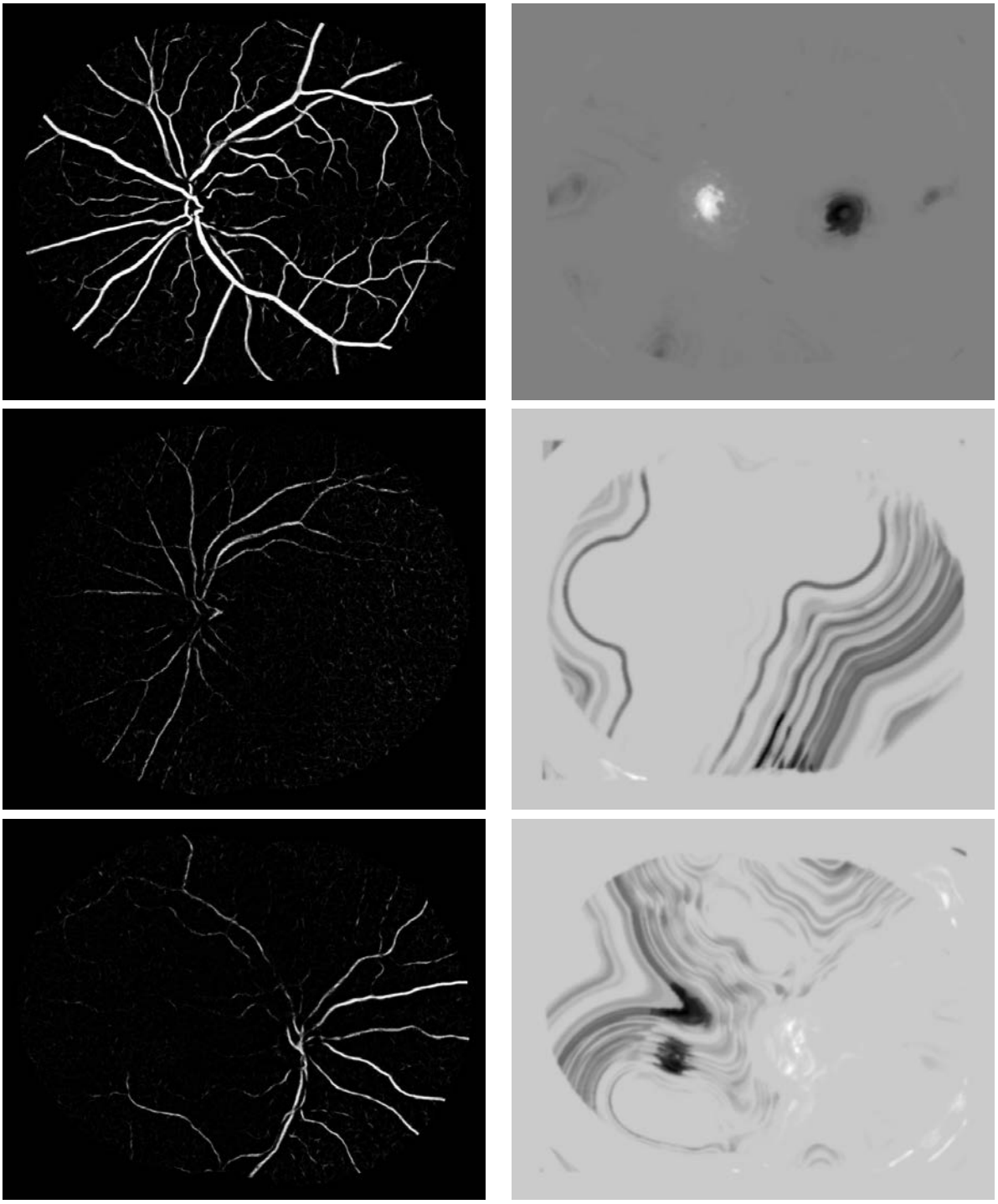

Figure 3.15: The effect of vessel probability image on the detection result. The top row shows what a normal vessel probability image looks like and the corresponding optic disc/fovea probability image. The second row and last row show two bad cases where insufficient information is provided by the vessel probability image.

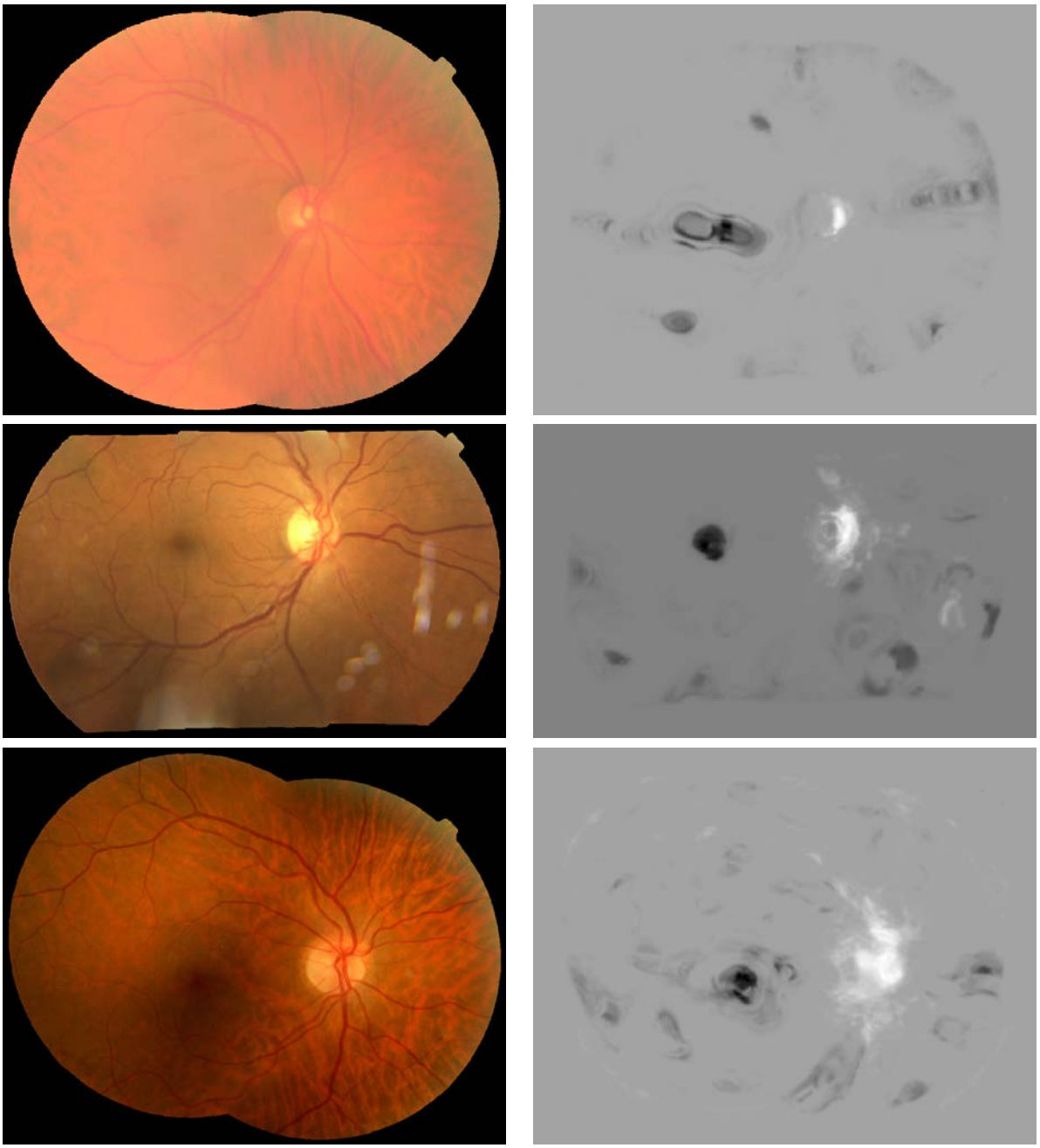

Figure 3.16: Examples of bad quality fundus images and results. The left column shows the fundus images. The right column shows the optic disc/fovea detection results. Though the image qualities are low, our system is able to correctly detect the locations.

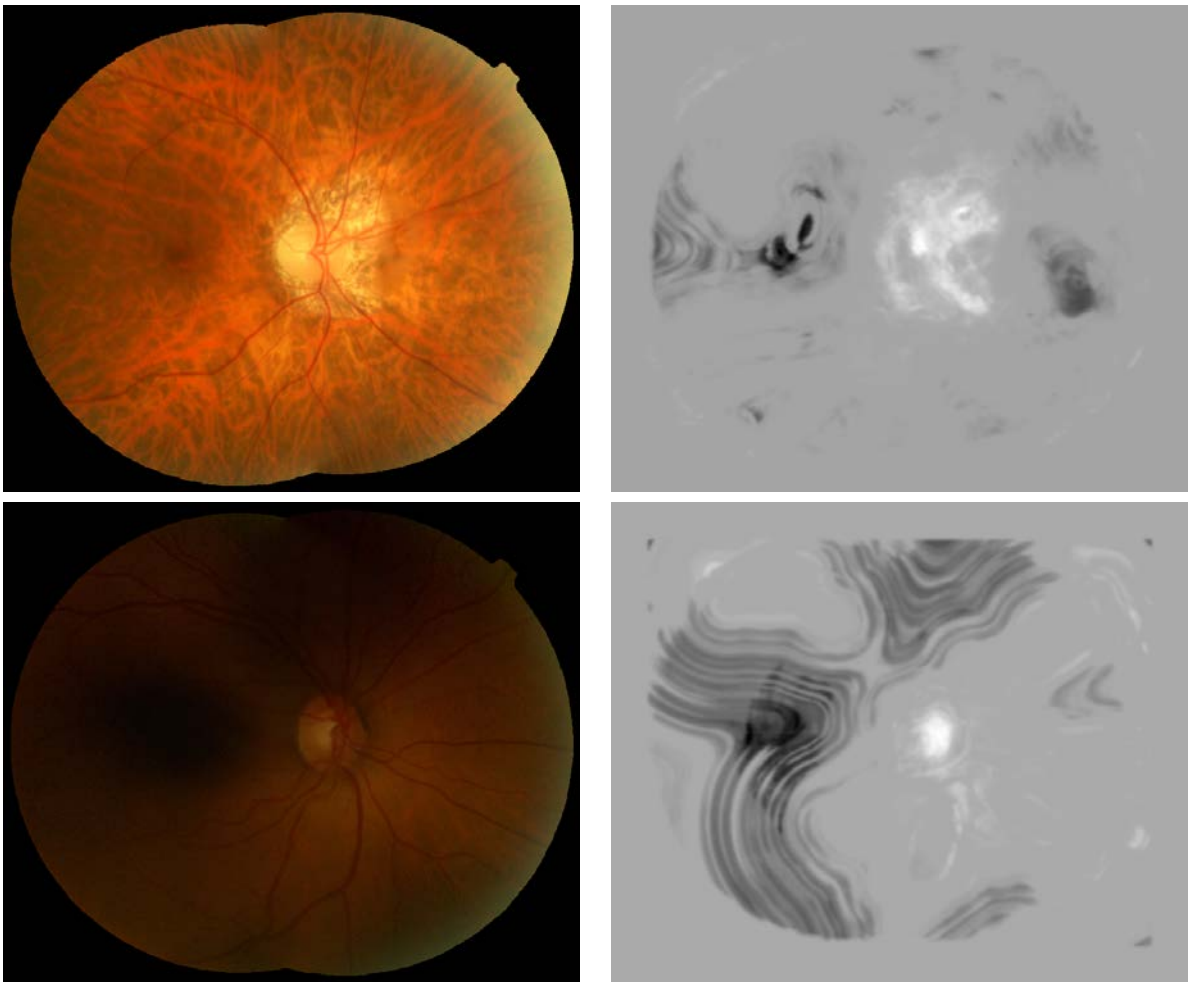

Figure 3.17: Examples of bad quality fundus images and results. The left column shows the fundus images. The right column shows the results. Our system failed to detect the optic disc/fovea locations.

Table 3.2: Selected features for the first k-NN classification.

feature #	feature description	template	image
1	number of vessels	quadrant 4	vessel image
2	average orientation difference	quadrant 3	vessel image
3	average orientation difference	quadrant 4	vessel image
4	standard deviation of orientation difference	quadrant 1	vessel image
5	standard deviation of orientation difference	quadrant 2	vessel image
6	standard deviation of orientation difference	quadrant 3	vessel image
7	standard deviation of orientation difference	quadrant 4	vessel image
8	orientation difference of max-width vessel	quadrant 3	vessel image
9	orientation difference of max-width vessel	quadrant 4	vessel image
10	vessel density	whole template	vessel image
11	standard deviation of image intensity	inner template	green channel image
12	standard deviation of image intensity	outer template	green channel image
13	average distance to nearest vessel pixel	inner template	distance image
14	max distance to nearest vessel pixel	inner template	distance image

Table 3.3: Features extracted for the second k-NN classification

for optic disc pixels	for fovea pixels
pixel intensity	pixel intensity
distance to fovea center	distance to optic disc
angle to fovea center	angle to optic disc

Table 3.4: Overview of test results

	left eye		right eye	
number of images	103		207	
	optic disc	fovea	optic disc	fovea
mean of distance error	19.6640	34.5459	20.6351	31. 1866
standard deviation of distance error	31.9516	63.9703	36.7664	51.1050
correct rate	93.2%	88.4%	94.0%	87.9%

CHAPTER 4
VESSEL WIDTH MEASUREMENT FOR STRAIGHT VESSEL SEGMENTS

This chapter presents a comprehensive description of the vessel width measurement. Literature reviews of previous work is given in Section 4.1. Method description and experimental methods are provided in Section 4.2 and Section 4.3. Result analysis is given in Section 4.4. At last, there is a general discussion section (Section 4.5).

4.1 Literatures

Most retinal vessel segmentation work focuses on separating the blood vessels from the background, leaving the issue of measurement to be treated separately.

Vessel detection approaches that have been published previously can be broadly divided into region-based and edge-based approaches. Region-based segmentation methods label each pixel as either inside or outside a blood vessel. Niemeijer *et al.* proposed a pixel based retinal vessel detection method using a Gaussian derivative filter bank and k-nearest-neighbor classification [9]. Staal *et al.* proposed a pixel feature based method that additionally analyzed the vessels as elongated structures [42].

Edge-based methods can be further classified into two categories: window-based methods [43] and tracking-based methods [44]. Window-based methods estimate a match at each pixel against the pixel's surrounding window. The tracking

approach exploits local image properties to trace the vessels from an initial point. A tracking approach can better maintain the connectivity of vessel structure. Lalonde *et al.* proposed a vessel tracking method by following an edge line while monitoring the connectivity of its twin border on a vessel map computed using a Canny edge operator [44]. Breaks in the connectivity will trigger the creation of seeds that server as extra starting points for further tracking. Gang *et al.* proposed a retinal vessel detection using second-order Gaussian filter with adaptive filter width and adaptive threshold [43].

The above methods locate the vessels, without directly determining vessel width. Algorithms to estimate the vessel width have been developed independently of vessel segmentation algorithms. Al-Diri *et al.* proposed an algorithm for segmentation and measurement of retinal blood vessels by growing a "Ribbon of Twins" active contour model, the *extraction of segment profiles* (ESP) algorithm, which uses two pairs of contours to capture each vessel edge [45]. The half-height full-width (HHFW) algorithm defines the width as the distance between the points on the intensity curve at which the function reaches half its maximum value to either side of the estimated center point [46]. The Gregson algorithm fits a rectangle to the profile, setting the width so that the area under the rectangle is equal to the area under the profile [47].

4.2 Methodology

Vessel width measurement on retinal image is a challenging problem. The main challenge comes from the low local contrast between blood vessel and the background,

as well as the large variation in image resolution and image quality. For example, Figure 4.1 shows two enlarged retinal images. The vessel edge is barely noticeable in the local view of the retinal image, which makes the exact vessel boundary delineation very challenging.

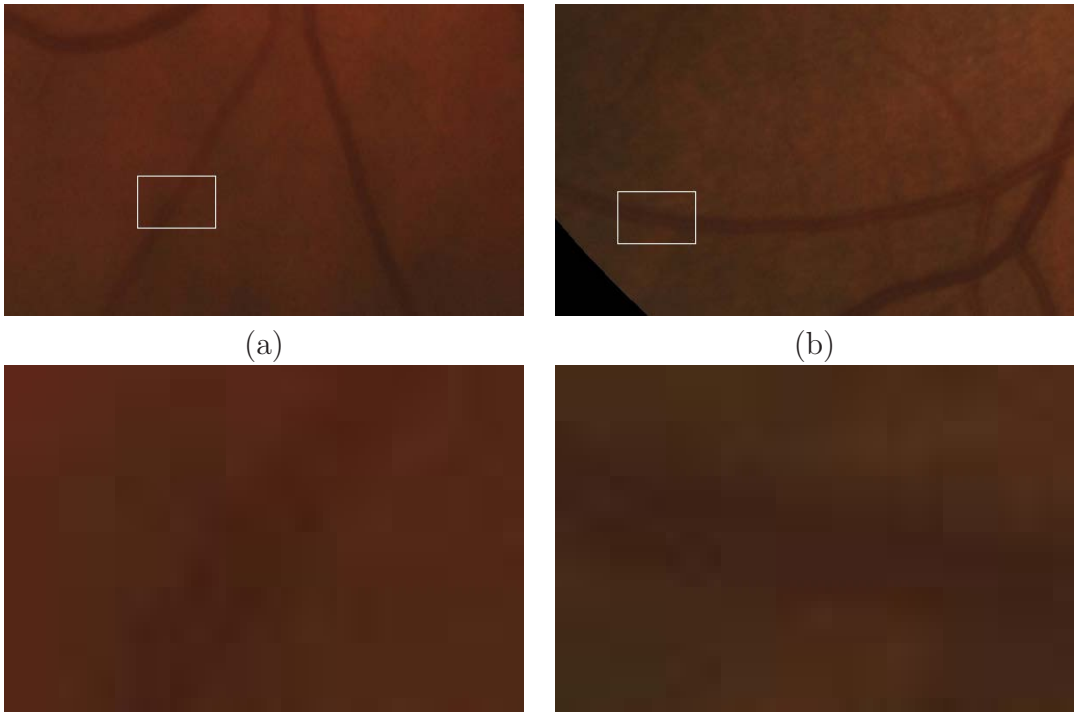

Figure 4.1: Illustration of the difficulties in accurate vessel width measurement. When the vessels are inspected locally, the vessel edge is very blurry and not well-defined. (a), (b) Two zoomed-in high quality normal fundus images. The rectangular areas show two vessel segments, which seems very clear and well-defind. (c), (d) Enlarged rectangular areas of (a) and (b). The vessel edge appears very blurry.

To solve these problems, a graph-based method to measure the vessel width in this thesis. Specifically, we use a graph-cuts algorithm to separate the selected

image regions into vessels and non-vessels. This method is motivated by the fact that the graph-based method gives a globally optimal solution, which frees the boundary delineation from local low image contrast.

4.2.1 Vessel Centerline Extraction

An initial segmentation is needed to build the graph. We use a vesselness map as proposed by Niemeijer *et al.* as our initial segmentation [9]. One example image is shown in Figure 4.2. By thresholding the gray scale image, a binary vessel segmentation is generated. A (constant) low threshold of 70 is chosen to better maintain the continuity of blood vessels. The trade-off is that small regions of noise may not be suppressed adequately. In order to solve this problem, the vessel regions with an area smaller than 20 pixels are erased from the thresholded image. A sequential thinning approach is then applied to the binary vessel segmentation to find the vessel centerlines [40].

4.2.2 Graph Construction

From this vessel centerline image, the bifurcation points and crossing points are excluded, because these points need special treatment. A bifurcation point is defined as a centerline pixel with three eight-connected neighbors and a crossing point is defined as a centerline pixel with four or more eight-connected neighbors. Hence, the vessel centerline image is scanned first to get the centerline pixels that have three or more neighbors. By deleting the bifurcation points and crossing points, the vessel trees are cut into vessel segments. From these vessel segments, the end points which

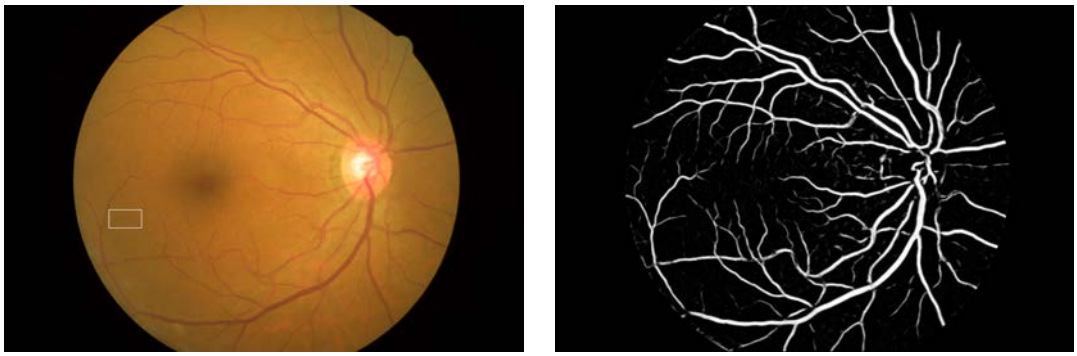

(a) (b)

Figure 4.2: Example vesselness image generated by a pixel classification method proposed by Niemeijer *et al.* [9]. (a) The color fundus image. The white rectangular is enlarged and used for illustration in Figure 4.3. (b) The corresponding vesselness image.

have only one neighbor pixel are found by scanning the image again. Starting from one end point, we then trace the vessel segment until the other end point is reached. In this way, we trace all the vessel segments on the image and label each of them.

For each labeled vessel segment, the growing direction for every centerline pixel is calculated. We use n adjacent centerline pixels on both sides of the target centerline pixel and apply principal component analysis on the resulting vessel segment [48]. The value of n is a parameter of the image size, which is approximately 0.005 times the first dimension of the image size. So if the first dimension of an image is 600 pixels. The value of n would be three pixels, resulting in a total vessel segment length of seven pixels. The minimum value of n is two. The first principal component corresponds to the growing direction of the pixel. An end point that does not have enough neighboring centerline pixels to define the vessel growing direction is determined to have the direction of the nearest centerline pixel that has a definition of a vessel

growing direction.

For the vessel growing direction, a counter-clockwise 90 degree is regarded as the normal direction for this point. Using the centerline pixels as the base nodes, profiles on the positive direction of the normal directions are built as one slice and profiles on the negative direction are built as another slice, as shown in Figure 4.3. The node step was 0.5 pixels. We used the "*multi-column model*" proposed by Li *et al.* [49].

Along each normal profile $Col(x, y)$ every node $V(x, y, z)(z > 0)$ has a directed arc to the node $V(x, y, z-1)$. Along the $x-$direction, meaning along the same boundary, for each node, a directed arc is constructed from $V(x, y, z) \in Col(x, y)$ to $V(x+1, y, max(0, z-\Delta_x)) \in Col(x+1, y)$. Similarly, arcs from $V(x, y, z) \in Col(x, y)$ to $V(x-1, y, max(0, z-\Delta_x)) \in Col(x-1, y, z)$ is constructed. Δ_x is the maximum difference allowed between two adjacent normal profiles within one boundary. Along the $y-$direction, meaning between the two slices, arcs from $V(x, y, z) \in Col(x, y)$ to $V(x, y+1, max(0, z-\Delta_y)) \in Col(x, y+1, z)$ and arcs from $V(x, y, z) \in Col(x, y)$ to $V(x, y-1, max(0, z-\Delta_y)) \in Col(x, y-1, z)$ is constructed. Δ_y is the maximum difference allowed between two corresponding normal profiles between the two boundaries. The base nodes are all connected [49]. A surface is regarded feasible if it satisfies the smoothness constraint defined by Δ_x and Δ_y. An optimal surface is defined as the surface with the minimum cost among all feasible surfaces defined in the 3-D volume.

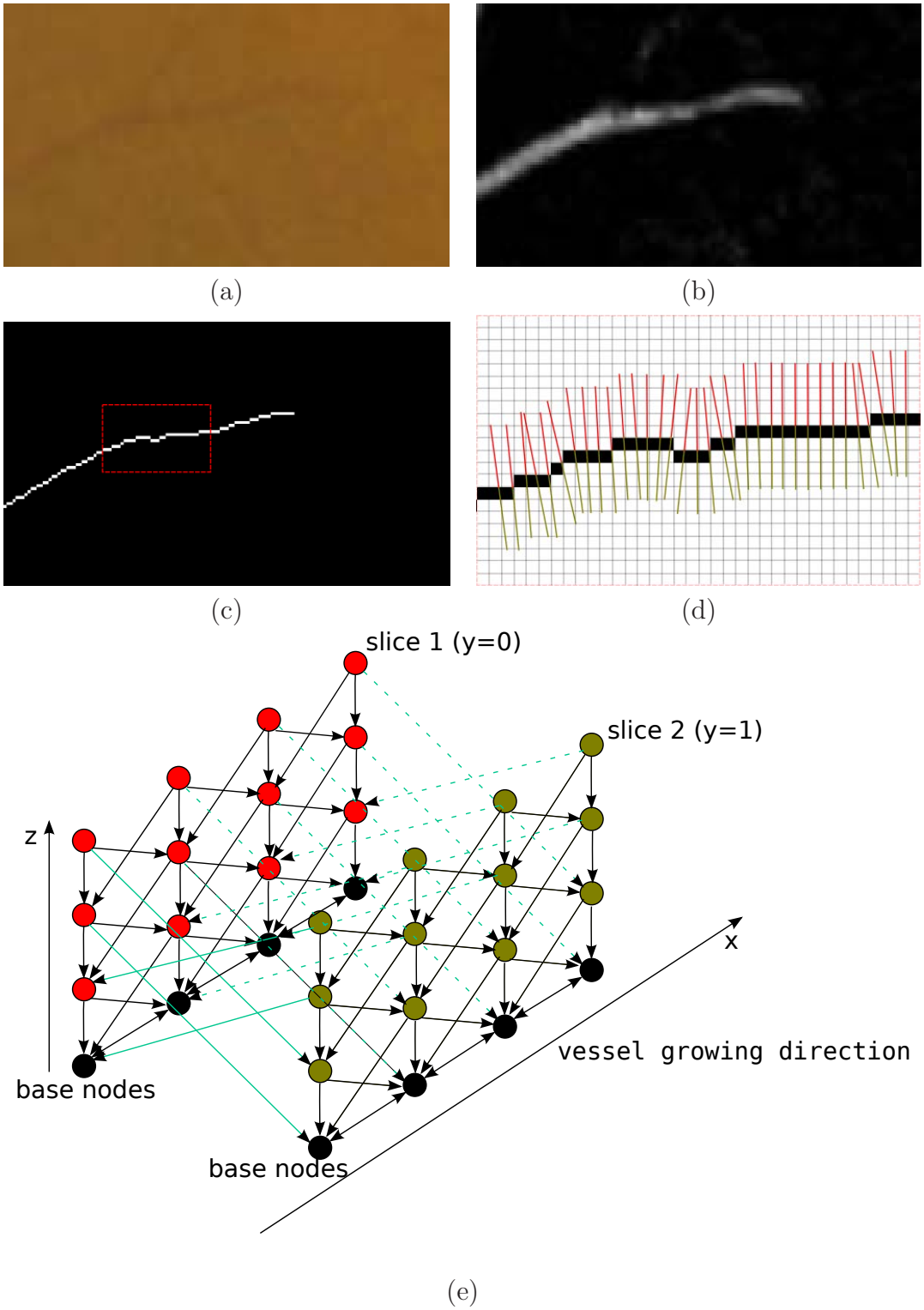

Figure 4.3: Illustration of how to luxate the vessel normal profiles into a graph. (a) A small segment of vessel extracted from Figure 4.2. (b) The vessel probability image of (a). (c) The vessel centerline image of (a). (d) The vessel growing directions are calculated and node normal profile perpendicular to the vessel growing direction are constructed. (e) Red normal profiles in (d) are used to build the red graph slice and the green normal profiles in (d) are used to build the green graph slice. The black nodes represent base nodes, corresponding to the black centerline pixels in (d). Consequently, the red slice represents one boundary in (d) and the green slice represents the other boundary in (d). Smoothness constraints (controlled by the arcs between adjacent columns) are applied differently to control the boundary smoothness within one boundary and between the two boundaries.

4.2.3 Cost Function

The cost image is generated from the orientation sensitive first order derivative of Gaussian of the green channel. The green channel of the color image usually shows the highest contrast between the blood vessels and background [50]. In order to find the gradient of vessels specified at different locations with different orientations, a steerable first order derivative of Gaussian filter is used in this study [51]. The separable first order derivative of Gaussian along the x-axis and along the y-axis are given in equations 4.1 and 4.2. The first order derivative of Gaussian along any angle θ is defined in equation 4.3.

$$G_1^{0^\circ} = -\frac{x}{\sigma_x^2}\exp(-\frac{x^2}{2\sigma_x^2}), \tag{4.1}$$

$$G_1^{90^\circ} = -\frac{y}{\sigma_y^2}\exp(-\frac{y^2}{2\sigma_y^2}), \tag{4.2}$$

$$G_1^{\theta} = cos(\theta)G_1^{0^\circ} + sin(\theta)G_1^{90^\circ}, \tag{4.3}$$

where σ_x and σ_y are the *scale* of the first order derivative kernel along the x-axis and y-axis. Because equations 4.1 and 4.2 are separable kernels, the original image is first convolved with $G_1^{0^\circ}$ and $G_1^{90^\circ}$ to get the first order derivative image along the x-axis and y-axis. Then within each normal profile, the weights of the profile nodes are calculated according to equation 4.3. Figure 4.4 (b) shows part of a cost image.

(a) (b)

Figure 4.4: Gradient image. (a) Part of a green channel image. (b) The corresponding orientation sensitive gradient image.

4.2.4 Graph Search and Boundary Determination

The value of Δ_x is set to one to maintain the smoothness within one boundary and Δ_y is set to two so that a difference is allowed between widths from the centerline to the left edge and from the centerline to the right edge, in case the centerline is not exactly at the center of the two edges. After the node-weighted directed graph is constructed, the optimal surface is determined[49]. To determine the vessel width, the coordinate difference between the two corresponding nodes on the optimal surface from the two slices are calculated. To show the boundary on the image, the nearest integer coordinate of every node on the optimal surface is calculated and shown on the image.

4.3 Experimental Methods

The REVIEW database (http://ReviewDB.lincoln.ac.uk) is used to assess the diameter measurement results. REVIEW is a publicly available database that contains a number of retinal profiles with manual measurements from three observers.

The four images from the *High Resolution Image Set* (HRIS) represent different severe grades of diabetic retinopathy. This set consists of four images where 90 segments containing 2368 profiles are manually marked. The images were subsequently down-sampled by a lateral factor of four for submission to the measurement algorithms, so that the vessel widths are known to ± 0.25 of a pixel, discounting human error. The *Central Light Reflex Image Set* (CLRIS) contains 285 profiles from 21 segments from two images from two patients. These images include early atherosclerotic changes that often includes a strong central vascular specular reflex. The *Vascular Disease Image Set* (VDIS) consists of eight digitally captured images, six of which illustrate different types of diabetic retinopathy. A set of 79 segments containing 2249 profiles are manually marked. This set of images is very noisy and suffers from pathologies. The *Kick Point Image Set* (KPIS) consists of two images containing three segments with 164 gold standard widths. By down-sampling the images to a lower resolution, these gold standard widths have higher accuracy than expressed in the measured images so the measurements can be assessed with sub-pixel accuracy.

To evaluate our method further, we determined the relationship between the average vessel width (both arteries and veins) and the distance to the optic disc, in a sample of 600 composite color fundus images, each consisting of two registered and blended fundus images, the characteristics of which were published previously [50]. For these images, automatically determined disc location and vesselness map were available [9, 52] .

4.4 Results

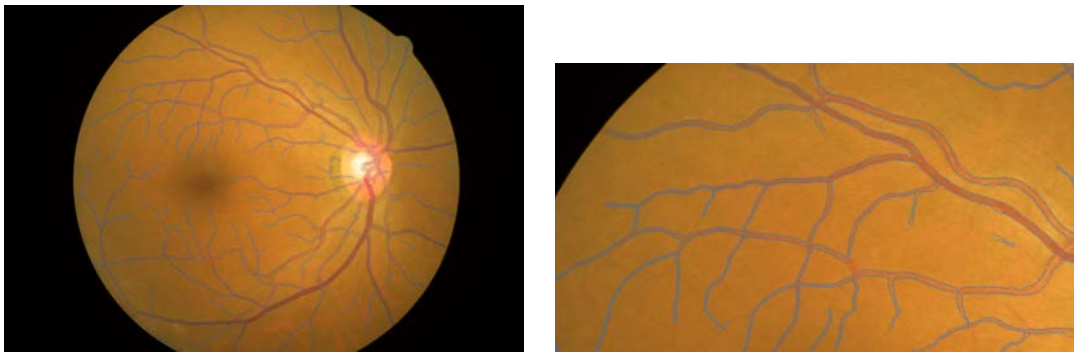

(a) (b)

Figure 4.5: Sample images showing the result of vessel boundary detection. (a) One image from the CLRIS database. Image size is 2160×1440, $\sigma = 4$. (b) A enlarged part of image (a).

An example of the quality of the obtained vessel boundary detection is shown in Figure 4.5. It shows a good performance on even the smallest vessels, which have low contrast.

The proposed method were compared to the other known algorithms in Table 4.1 to Table 4.4. The first three rows are the manual result from the observers. Row 4-8 show the results of the other algorithms. The last row shows the result of proposed method. The first column is the success rate. It is worth noticing that the definition of success rate is different in our method and in Al-Diri's paper. In their paper, a point that has a meaningful measurement (e.g. a measurement that converges) was assigned "success measurement" [45]. In contrast, we counted every centerline pixel that had corresponding ground truth profiles as a "success measurement", irrespective

of our estimate of the width. Therefore all measurements with a corresponding ground truth profile were included even if the measurements did not result in a meaningful estimation. The columns 2-3 are the mean and standard deviation of all measurements labeled as 'success measurement'. Column 4-5 are the signed mean and standard deviation of the point-by-point differences.

Among the four datasets, the HRIS dataset has the highest image resolution (3584×2438 pixels). The performance of the vessel width detection is comparable to the observers. The CLRIS dataset images have a resolution of 2160×1440 pixels. The mean vessel with and the point-by-point difference mean are very close to the observers' performance. But the point-by-point difference standard deviation is high. The VDIS dataset has a resolution of 1360×1024 pixels. The mean vessel width is 0.53 pixels smaller than the ground truth. The KPIS dataset has the smallest image resolution, 288×119 pixels and 170×92 pixels.

Table 4.1: Vessel Width Measurement Accuracy of HRIS (success rate in percentage, mean μ and standard deviation σ in pixel)

Method Name	Success Rate %	Measurement		Difference	
		μ	σ	μ	σ
Observer 1 (O_1)	100	4.12	1.25	-0.23	0.288
Observer 2 (O_2)	100	4.35	1.35	0.002	0.256
Observer 3 (O_3)	100	4.58	1.26	0.23	0.285
Gregson's Algorithm	100	7.64	-	3.29	2.841
Half-height full-width (HHFW)	88.3	4.97	-	0.62	0.926
1-D Gaussian Model-fitting	99.6	3.81	-	-0.54	4.137
2-D Gaussian Model-fitting	98.9	4.18	-	-0.17	6.019
Extraction of Segment Profiles (ESP)	99.7	4.63	-	0.28	0.42
Proposed Method	**100**	**4.56**	**1.30**	**0.21**	**0.567**

Table 4.2: Vessel Width Measurement Accuracy of CLRIS (success rate in percentage, mean μ and standard deviation σ in pixel)

Method Name	Success Rate %	Measurement		Difference	
		μ	σ	μ	σ
Observer 1 (O_1)	100	13.19	4.01	-0.61	0.566
Observer 2 (O_2)	100	13.69	4.22	-0.11	0.698
Observer 3 (O_3)	100	14.52	4.26	0.72	0.566
Gregson's Algorithm	100	12.8	-	-1.0	2.841
Half-height full-width (HHFW)	0	-	-	-	-
1-D Gaussian Model-fitting	98.6	6.3	-	-7.5	4.137
2-D Gaussian Model-fitting	26.7	7.0	-	-6.8	6.019
Extraction of Segment Profiles (ESP)	93.0	15.7	-	-1.90	1.469
Proposed Method	**94.1**	**14.05**	**4.47**	**0.08**	**1.78**

Our testing indicates that fundus images with a higher resolution can be measured more accurately with a larger σ. The final choice of σ is $\sigma = 7$ for HRIS dataset, $\sigma = 4$ for CLRIS and VDIS, $\sigma = 1$ for KPIS.

Figure 4.6 shows the correlation of predicted vessel width and the mean of the observers' measurement for HRIS. The regression line shows the prediction tends to give a smaller measurement for vessels with fine vessels while a larger measurement for large vessels, compared to the observers' measurements.

4.4.1 Relationship between Vessel Width and Distance to Disc

The relationship between vessel width and distance from the optic disc center is shown in Figure 4.7. A total of 2,936,749 centerline pixels were extracted from the 600 images. If we do not consider the pixels near the center of optic disc, where the blood vessels show a very complicated structure, the average vessel width shows a

Table 4.3: Vessel Width Measurement Accuracy of VDIS (success rate in percentage, mean μ and standard deviation σ in pixel)

Method Name	Success Rate %	Measurement		Difference	
		μ	σ	μ	σ
Observer 1 (O_1)	100	8.50	2.54	-0.35	0.543
Observer 2 (O_2)	100	8.91	2.69	0.06	0.621
Observer 3 (O_3)	100	9.15	2.67	0.30	0.669
Gregson's Algorithm	100	10.07	-	1.22	1.494
Half-height full-width (HHFW)	78.4	7.94	-	-0.91	0.879
1-D Gaussian Model-fitting	99.9	5.78	-	-3.07	2.110
2-D Gaussian Model-fitting	77.2	6.59	-	-2.26	1.328
Extraction of Segment Profiles (ESP)	99.6	8.80	-	-0.05	0.766
Proposed Method	**96.0**	**8.35**	**3.00**	**-0.53**	**1.43**

monotonic decrease from a distance of 20 pixels to 450 pixels, with a sudden slope change at a distance of 300 pixels to the optic disc. For vessels near the optic disc border, the average vessel width is about 5.0 pixels (approximately 75 microns) while the vessels that have a distance of 450 pixels to the optic disc have an average vessel width of 3.5 pixels (approximately 52.5 microns).

4.5 Discussion

We introduced a novel method to find the retinal blood vessel boundaries using a graph-based approach. The results of our evaluation show that the blood vessel boundaries are accurate, and our method outperforms the current state-of-the-art algorithm on two datasets of standard retinal image resolution, while it underperforms on lower resolution retinal images [45], as further discussed in Section 4.5.1. Our method allows us to find the retinal vessel boundaries of even small vessels on standard posterior pole images as used in diabetic retinopathy screening programs

Table 4.4: Vessel Width Measurement Accuracy of KPIS (success rate in percentage, mean μ and standard deviation σ in pixel)

Method Name	Success Rate %	Measurement		Difference	
		μ	σ	μ	σ
Observer 1 (O_1)	100	7.97	0.47	0.45	0.234
Observer 2 (O_2)	100	7.60	0.42	0.08	0.213
Observer 3 (O_3)	100	7.00	0.52	-0.52	0.233
Gregson's Algorithm	100	7.29	-	-0.23	0.602
Half-height full-width (HHFW)	96.3	6.47	-	-1.05	0.389
1-D Gaussian Model-fitting	100	4.95	-	-2.57	0.399
2-D Gaussian Model-fitting	100	5.87	-	-1.65	0.337
Extraction of Segment Profiles (ESP)	100	6.56	-	-0.96	0.328
Proposed Method	**99.4**	**6.38**	**0.59**	**-1.14**	**0.67**

around the world [53]. Though the performance on the HRIS and CLRIS was close to the human experts reference standard, it tends to be biased towards showing a smaller measurement, for smaller vessels. The most likely explanation is that the vessel width measurement is done with a fixed scale parameter σ, while the optimal measurement of vessels in different scales need different scale parameters. A multi-scale cost function is under study to solve this problem.

Alternatively, vessel width can be measured directly from the vesselness map. In a preliminary experiment, we thresholded the vesselness image, generating a binary vessel segmentation. A fixed threshold of 190 was used. Width were then measured on this binary vessel map, resulting, on the HRIS dataset, in average vessel width of 6.5 pixels, with a standard deviation of 32.52 pixels. Therefore, the vesselness map itself gave a poor estimation of the mean of vessel width, with a standard deviation about 30 times higher than other methods, which makes this approach unfeasible.

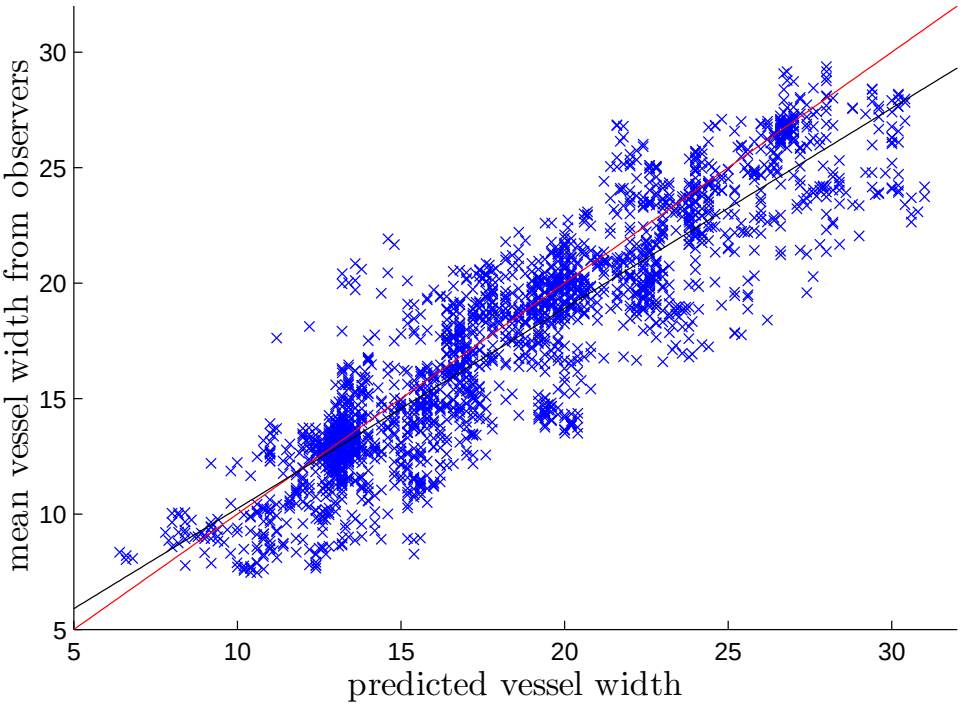

Figure 4.6: Correlation of predicted vessel width and the mean of the observers' measurements for HRIS. Each point represent one profile. The red line is the $y = x$ line. The black line is the regression line ($y = 0.87x + 1.56$).

4.5.1 Width Measurement on Images of Different Resolution

The proposed method showed a consistently underestimated vessels in (comparing with RS) low resolution images, especially for the KPIS dataset, where the point-by-point difference is -1.14 pixels. But we also noticed that all other algorithms in Table 4.4 also underestimated the width. Figure 4.8 illustrates the RS and the algorithmic estimates on vessel segments from a high resolution image and a low resolution image. This is a cross-sectional view of vessel intensity with regard to the distance to the centerline. The black line is the average intensity of all normal profile

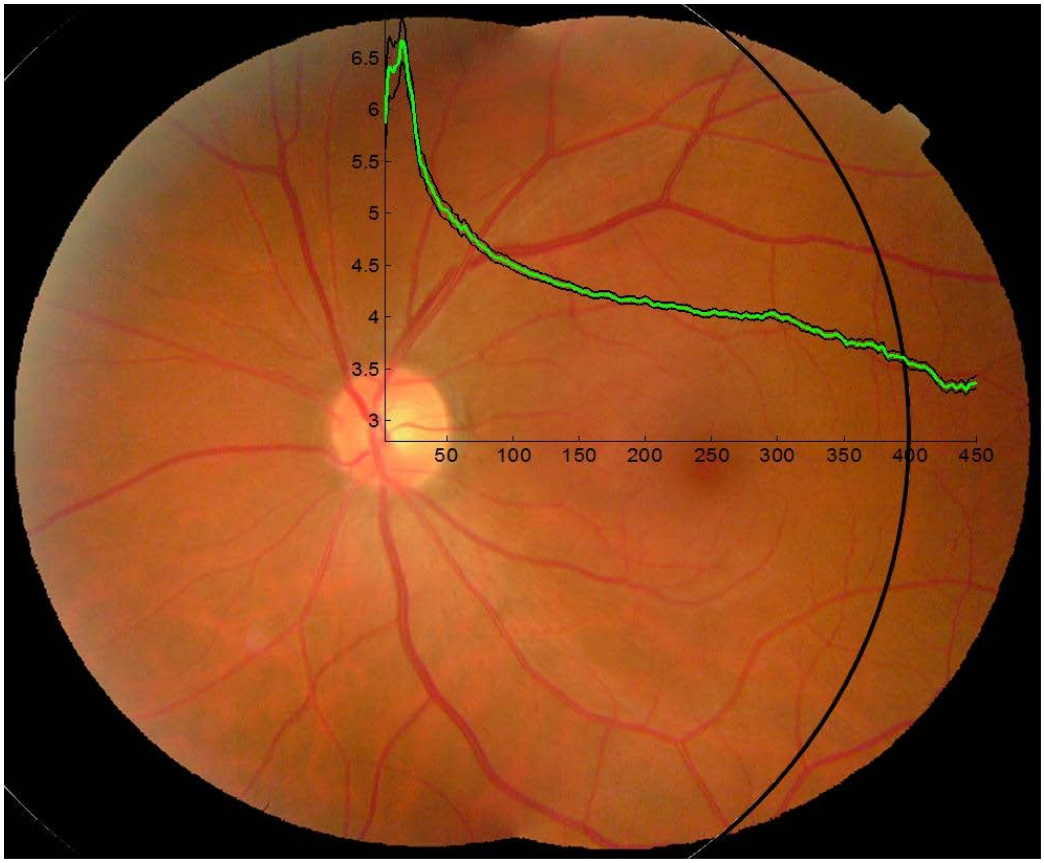

Figure 4.7: Visualization of the relationship between vessel width and distance to optic disc. The black circle marks a 400 pixels to the optic disc center. The vessel width analysis starts from the optic disc center and ends at a distance of 450 pixels (the x-axis). The y-axis shows the vessel width in pixels. The green line is the average vessel width. The black lines are the 95% confidence interval lines. Image resolution is about 800×700 pixels. Scale parameter $\sigma = 4$ pixels was used.

nodes with the same distance to the centerline in the vessel segments. The red star is the average vessel width across the whole vessel segment marked by observers. The green star is the average vessel width across the whole vessel segment measured by proposed method. The HRIS image has a resolution of 3584×2438 pixels. The vessel segment has a mean vessel width of about 26 pixels and the edge crosses about ten pixels. The KPIS image has a resolution of 288×119 pixels. The vessel segment

has a mean vessel width of about seven pixels and the edge crosses about three pixels. This figure suggests the underlying standards for width measurement of vessels in different scales are different. On the HRIS vessel segment, Both the RS and the proposed method found the location with the maximum gradient as the vessel edge. However, on the KPIS vessel segment, the RS and the proposed method give different measurements. The observers on average give a larger measurement on those low resolution vessels.

4.5.2 Vessel Width and Distance to Optic Disc

Our results show that the relationship between vessel width with distance and the optic disc center is inverse and monotonous. Using this method, we were able to reliably determine the relationship between the average retinal vessel diameter and the distance from the optic disc from 600 patients with diabetes. Except for the vessel pixels near the center of the optic disc (about 20 pixels), the blood vessel width shows a monotonic decrease considering the distance from the optic disc to the center. This is most likely caused by branching - if we assume the blood vessel volume to be unchanged. If the number of blood vessels is kept constant, the higher the branch frequency with increasing distance to the optic disc, the larger the slope of the width decrease. At a distance of around 300 pixels, there is a slight slope change in average vessel width, most likely caused by the fact that this is where the image centered on the optic disc ends and transitions to the fovea centered image that is registered to it in our dataset.

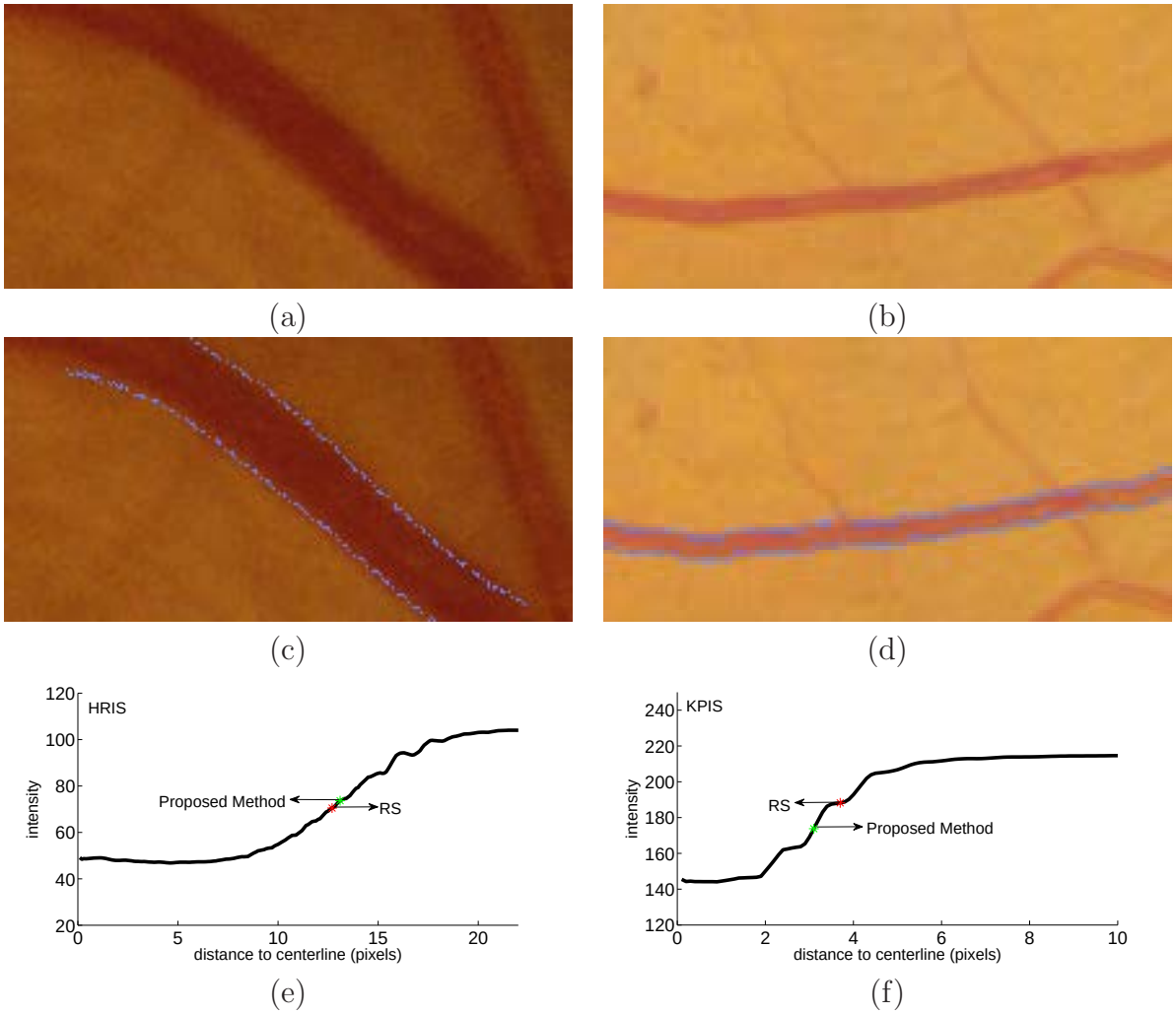

Figure 4.8: Vessel width measurement on vessel segments with different resolutions. (a) One test vessel segment from HRIS. The length of the vessel segment is 173 pixels. (b) One Test vessel segment from KPIS. The length of the vessel segment is 226 pixels. (c) The vessel width measurement result of (a). If the detected edge is not at an integer location, the nearest integer coordinate is shown. (d) The vessel width measurement result of (b). If the detected edge is not at an integer location, the nearest integer coordinate is shown. (e) The cross-sectional view of vessel intensity with regard to the distance to the centerline for (a). The black curve is the average of 173 normal profiles in the vessel segment. Intensities at non-integer locations are linearly interpolated. The red star is the average vessel width across the whole vessel segment marked by observers. The green star is the average vessel width across the whole vessel segment measured by proposed method. The two boundaries are flipped and shown in one figure. (f) The cross-sectional view of vessel intensity with regard to the distance to the centerline for (b). The black curve is the average of 226 normal profiles in the vessel segment. Intensities at non-integer locations are linearly interpolated. The red star is the average vessel width across the whole vessel segment marked by observers. The green star is the average vessel width across the whole vessel segment measured by proposed method. The two boundaries are flipped and shown in one figure.

Though our method has been tested on retinal images only, it may be equally effective on other two-dimensional blood vessel projections such as cardiac and brain angiograms.

4.5.3 Computational Performance

The proposed method has a high computational performance. For a retinal image of size 2160 × 1440 pixels, vesselness map creation takes about 110 seconds, and this is an operation $\mathcal{O}(n)$, where n is the number of pixels. The image skeletonization and small region removal takes about 120 seconds, and this is also an operation $\mathcal{O}(n)$. The total number of centerline pixels is around 20000 pixels (or $0.0064n$) and the total number of vessel segments is 160. Consequently the average length of the graph is around 125 pixels. The average size of the graph would be slice number × height of graph × length of graph, which is 45000 (or $0.0145n$) in this case. It takes around 9 seconds to build all the graphs in the image. The method we used to solve the max-flow problem is a pseudoflow algorithm. The running time is $\mathcal{O}(n^3)$ [54]. It takes about 41 seconds to solve all the graphs in the example image.

4.5.4 Limitations

Our approach has some limitations. It relies largely on the initial segmentation, the vesselness image. False positives or disconnected vessels may result in incorrect vessel boundary detection and vessel diameter measurements. A low threshold value and spur pruning is one possible way to reduce the problem. But the trade-off is the loss of some fine vessel information.

The crossing points and branching points are currently not treated separately, because the vessel growing direction, and consequently the vessel normal direction, at those points are not well defined. This does not have a significant influence on the vessel diameter measurements. However, the generation of the continuous vessel tree will require the vessels be connected at the crossing and branching points. A possible method to solve the direction problem at the crossing points and branching points is the distance transform of the vessel centerline image. For the crossing points, branching points and centerline pixels near them, the direction with the maximum gradient can be considered as the normal profile direction. Another solution is detecting and dealing with the crossing and branching points explicitly.

CHAPTER 5
VESSEL WIDTH MEASUREMENT AT BRANCHING POINTS

5.1 Literatures

Over two hundred published studies have explored the field of retinal vasculature structure detection and vessel width measurements. However, only a few of them treat branching points specifically. There are two steps in vessel width measurement at branching points: detection of the branching points, and vessel width measurement at branching points.

Most of the retinal branching points detection methods target at using the bifurcations as a landmark for further image analysis [55, 56, 57, 58, 59], such as retinal image registration. Shen *et al.* in 2001, proposed a real-time landmark extraction method from fundus images. This model-based method detects branching points as a fragment of the vasculature that consist of two relatively straight anti-parallel edges with either and intensity peak or an intensity valley in between. Tsai *et al.* further refined this method in 2004, in which the dtected branching point is used as the initial estimated branching point. Then an exclusion region is provided around the estimated branching point and the location is further refined within the exclusion region. Finally, in 2008, Bhuiyan *et al.* proposed a method to detect vascular bifurcations and crossovers based on the vessel geometrical features. A binary vessel image is first segmented from the color fundus image and morphological thinning operation is applied to find the vessel centerline. Then rotational invariant 3×3 masks are used

to detect potential bifurcations and crossover points. At last, the geometrical and topological properties are used to refine the result. A detection accuracy of 95.82% was reported. Quelhas *et al.* proposed a method to detect branching points by using the bi-level thresholding [58].

Compared with vessel branchpoint detection, fewer studies have addressed vessel branching width measurement. In most retinal branching studies, the vessel width is measured using manual ([20, 14, 26, 28]) or semi-automatic methods ([25, 24, 30]). In a study on the relationship of peripheral vascular disease and arteriolar bifurcation diameter, Chapman *et al.* proposed a semi-automatic method to measure the vessel width for arterioles [25]. This method needs human expet operators to draw lines perpendicular to arteriole and then an automatic method is used to determine the points of maximum intensity variation based on the cross-sectional profiles [60]. This method was not specific for retinal vascular branchings. Doubal *et al.* proposed a semi-automatic method that can track down each sub-branch if the branching center is identified by a trained grader. Then the cross-sectional profiles can be obtained and a Gaussian curve is fitted to determine the width [24]. Each profile needs manual inspection after the fitting. Patton *et al.* used a similar semi-automatic method to calculate the branching vessel width [30]. The human operator manually identifies the arteriolar and venular branching points and draw a line perpendicular to the vessel. Four other intensity profiles can be automatically generated from the given profile. Each profile can be rejected or accepted by the operator. Then a Gaussian fitting is used to identify the vessel width.

To our knowledge, no fully automatic method has been developed to specifically deal with the vessel width measurement problem at branching points on fundus image.

5.2 Methodology

We have previously published a graph based method to measure the vessel width for straight vessel segments [61]. The vessel centerline image is used to obtain the based-nodes for the graph. Then, a two-slice three-dimensional graph is luxated for each vessel segment. The graph columns are built perpendicular to the vessel growing directions. The perpendicular direction is calculated using principal component analysis (PCA). A smoothness constraint between the two slices is applied. Thus the simultaneous two-dimensional boundary segmentation problem is transformed into a three-dimensional surface segmentation problem. It is further converted to a minimum closed set problem in a node-weighted graph. By solving the minimum closed set problem, the two boundaries of blood vessels can be determined and the vessel width can be measured. The traditional graph constructs graph column perpendicular to the vessel growing direction and the perpendicular direction is calculated using PCA. This method is referred to as PCA method for the rest of the paper.

The traditional graph construction method at straight vessel width measurement could not be extended to branching point vessel width measurement, as explained in Figure 5.2. First, the graph columns will intersect each other as the graph columns approaches the branching center, resulting in multiple vessel width measure-

ment at the same point. Second, the graph columns might run into adjoining vessel branches, resulting in meaningless measurements of vessel width inside the vessel segment. In order to address these problems, a different graph construction method is needed. We propose a electric field theory motivated graph construction method to solve this problem. Similar to the PCA method, the electric field theory motivated graph construction method is referred to as ELF method for short.

The remainder of the method description is organized as follows. The image pre-processing and bifurcation detection is explained in Section 5.2.1. The graph construction that specifically deal with the branching problem is discussed in Section 5.2.2. Cost function design is described in Section 5.2.3. Graph search and boundary determination is briefly discussed in Section 5.2.4. Finally, the vessel width measurement at straight vessel segments and at branching points are combined and a smooth and consistent vessel width measurement is given for the whole vessel tree. The method is described in Section 5.2.5. The experimental methods are given in Section 5.3.

5.2.1 Pre-processing and Bifurcation Detection

The goal of pre-processing is to obtain a vessel centerline image as the initial segmentation. We start with the vesselness map as proposed by Niemeijer *et al.*, and as shown in Figure 5.1 (b). The vesselness map is a gray scale image with each pixel assigned the likelihood of being in a blood vessel. The higher the intensity, the higher the likelihood. By thresholding the gray scale image, a binary vessel segmentation

image is generated. A constant low threshold of 70 is chosen to better maintain the continuity of blood vessels. The trade-off is that small regions of noise may not be suppressed adequately. So the vessel regions with an area smaller than 20 pixels are erased from the binary vessel image. A sequential thinning approach is then applied to the binary vessel segmentation image to find the vessel centerline [40].

The branching points are detected on the vessel centerline image using a series of 3×3 kernels [40]. The kernels are given in Equation 5.1.

$$k_1 = \begin{bmatrix} 1 & 0 & 1 \\ 0 & 1 & 0 \\ 0 & 0 & 1 \end{bmatrix}, \quad k_2 = \begin{bmatrix} 1 & 0 & 1 \\ 0 & 1 & 0 \\ 0 & 1 & 0 \end{bmatrix}, \cdots, \quad k_{16} = \begin{bmatrix} 0 & 0 & 1 \\ 0 & 1 & 0 \\ 1 & 0 & 1 \end{bmatrix} \tag{5.1}$$

These kernels can effectively detect branching points on the binary vessel centerline image. However, not all detected branching points are true vessel branchings, as shown in Figure 5.1 (c). False branches can result from abrupt vessel width changes, vessel direction changes, or from noise. Moreover, the vessel crossings are often detected as two adjacent branchings on the vessel centerline image due to sequential thinning. Hence, a spur pruning and crossing point exclusion step is required.

Starting from a detected branching point, all the three sub-branches are traced. If another branching point is reached within certain distance, the two branching points are regarded as a single crossing point and excluded from further study. On the other hand, if an end point is reached within certain distance, the traced sub-branch is regarded as a spur and removed from the centerline image.

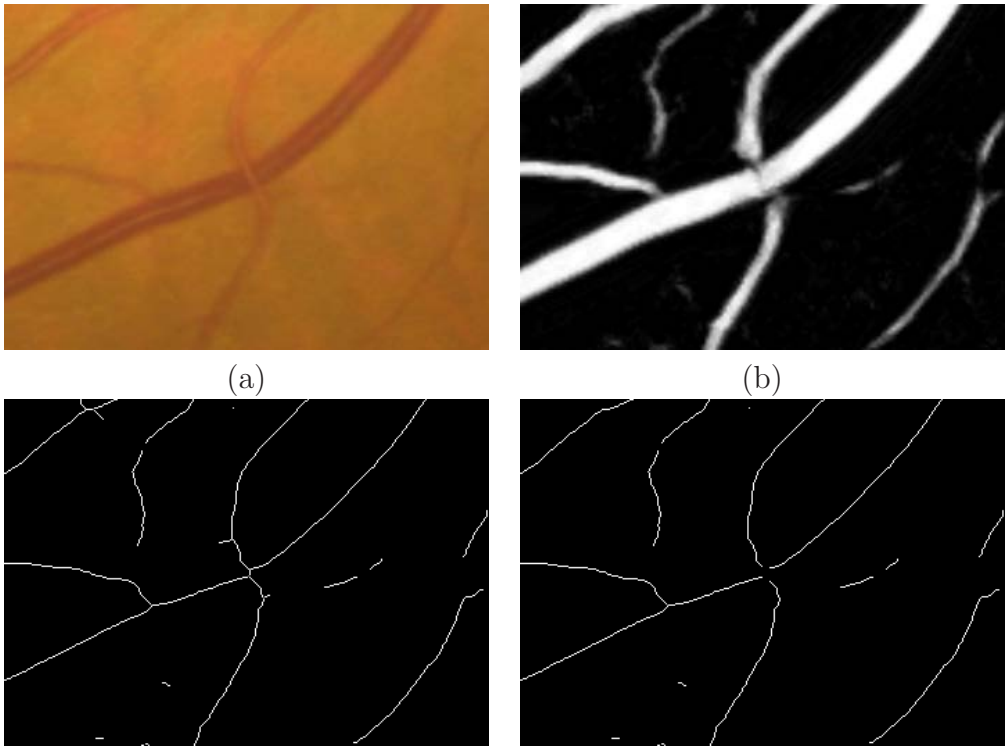

Figure 5.1: Spur pruning and crossing point exclusion on vessel centerline image. (a) An enlarged part of a color fundus image. (b) The corresponding vesselness map. (c) The corresponding vessel centerline image, with detected branching points shown in gray. Spurs are presented due to abrupt vessel direction changes. A crossing point is split into two branching points. (d) The corresponding vessel centerline image after spur pruning and crossing point exclusion.

5.2.2 Graph-Based Vessel Boundary Segmentation

We apply an electric field theory motivated graph construction method to build the graph at branching points. This graph construction method was first proposed by Yin *et al.* in 2009 [62]. The method is inspired by the non-intersecting property of electric lines of force. Recall the Coulomb's law:

$$E_i = \frac{1}{4\pi\varepsilon_0}\frac{Q}{r^2}\hat{\mathbf{r}}, \tag{5.2}$$

where E_i is the electric field at point **i**, Q is the charge of point **i**, r is the distance from the point **i** to the evaluation point **j**, $\hat{\mathbf{r}}$ is the unit vector pointing from the point **i** to the evaluation point **j**, and ε_0 is the vacuum permittivity. The total electric field E at point **j** is the sum of E_i:

$$E = \sum E_i, \tag{5.3}$$

the electric field has the same direction as the *electric line of force* (ELF).

When multiple source points exist in an electric field, the electric line of force exhibits the non-intersecting property. If we change r^2 to $r^n (n > 0)$, the non-intersection property still holds. The difference is that the vertices with larger distances will be penalized in ELF computing. A value of $n = 4$ is used to decrease the effect from pixels with a larger distance and hence increase the robustness of local ELF computation.

In the problem of graph construction at branching points, we assume each vessel centerline pixel is a positive unit charge. The electric line of force is calculated and the graph is constructed along the electric line of force, as illustrated in Figure 5.2 (b).

If we consider the branching to be isolated from the vessel tree, the graph given above is good enough to give a reliable measurement. However, if a consistent vessel width measurement is desired for the whole vessel tree, problems will arise at the transition from the graph built for a branching point to the graph built for the adjoining straight vessels, as shown in Figure 5.3 (a). The electric line of force points

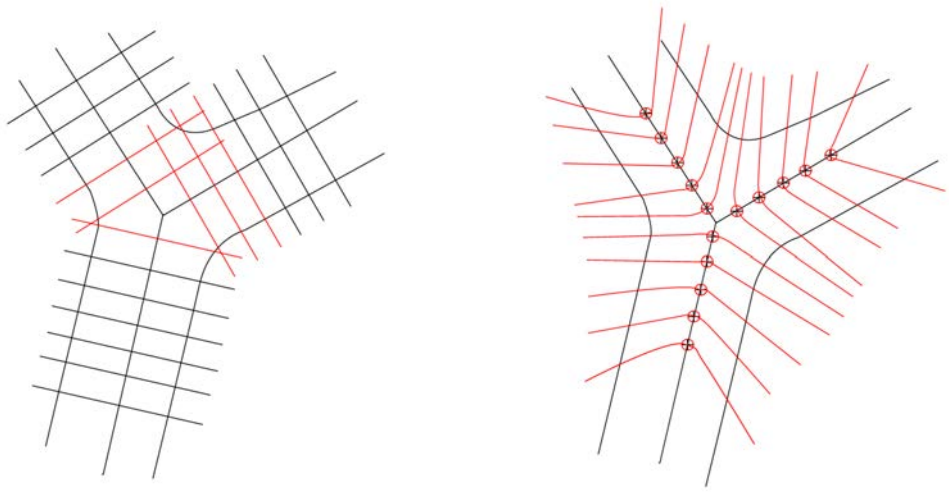

(a) (b)

Figure 5.2: Illustration of problems in applying traditional graph construction method to branching points and introduction to electric field theory based graph construction method. (a) A figure to illustrate possible problems in applying traditional graph construction method to branching point situation. The problems include possible graph column intersection and graph columns running into another vessel branch. (b) Introduction to electric field theory based graph construction method. Its most attractive is the non-intersecting property of electric field lines.

outside at the end of each branch. When the two kinds of graph are connected, the graph columns from different methods will intersect.

We propose two strategies to improve the electric field theory based graph construction method, as illustrated in Figure 5.3. First, in order to pull the electric lines of force towards the normal direction at the end of each branch, extra positive charges and negative charges are added in the electric field. Positive charges with extremely large values are positioned at the infinite extension of each branch. This is used to generate a parallel force along the vessel growing direction that can push the graph columns toward the perpendicular direction. A distance of 10,000 pixel is

used to simulate the infinite distance and the charge value was chosen to be 100,000 unit charges. The choice of the distance value and charge value are not sensitive and do not have a large difference as long as they are big enough to be considered as "infinity" in this case. In order to further pull the graph columns towards the normal direction, three negative charges are positioned in the middle points of three branches. The value of the negative charges are also not sensitive as long as they are comparable to the value of adjacent positive charges. We chose the value to be five in our case.

Second, a combined graph construction method is introduced at the transition location. Six centerline pixels at the transition location are used to build the combined graph. First of all, the location of graph nodes are calculated using both the PCA method and the ELF method, given by $(x_{pca|i}, y_{pca|i})$ and $(x_{elf|i}, y_{elf|i})$, where $i = 0, 1, ..., 5$ is the distance from the graph column to the branching center. Then the node locations in the combined graph is calculated using a weighted linear interpolation of $(x_{pca|i}, y_{pca|i})$ and $(x_{elf|i}, y_{elf|i})$:

$$\begin{cases} x_i &= 0.2ix_{pca|i} + (1 - 0.2i)x_{elf|i} \\ y_i &= 0.2iy_{pca|i} + (1 - 0.2i)y_{elf|i} \end{cases}, \tag{5.4}$$

where $i = 0, 1, ..., 5$.

5.2.3 Cost Function

The cost function is generated from convolution of the image's green channel with an oriented first order derivative of Gaussian l. The green channel has been

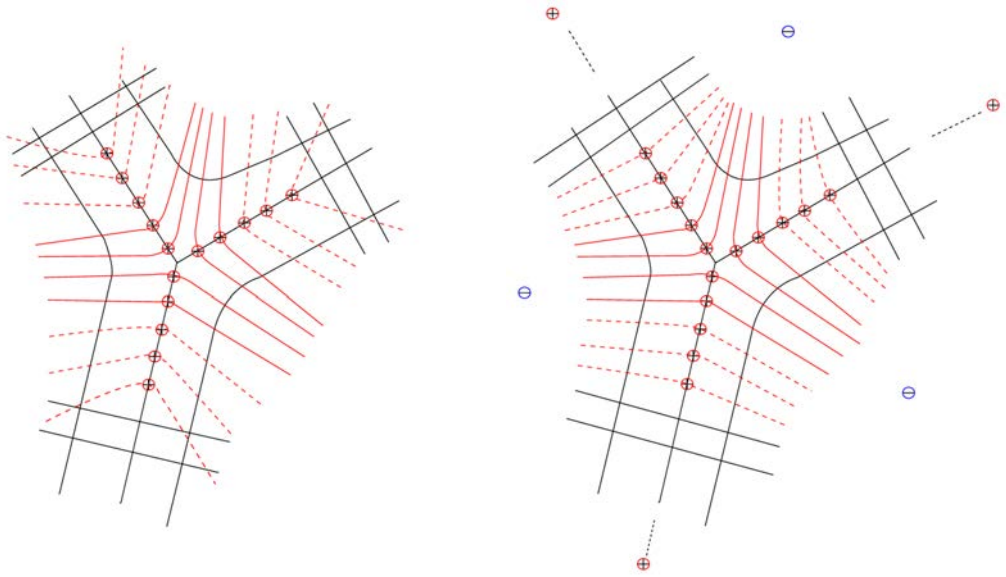

(a) (b)

Figure 5.3: Improvement of the electric field theory based graph construction method. For illustration purposes, not all graph columns are shown in the figure. (a) Problems encountered when combining the traditional graph and electric field theory based graph. The graph columns intersect each other because the graph columns from the electric field theory based method point outside rather than the normal direction when approaching the end of sub-branches, as shown in dashed red lines. (b) Improved combined graph. Two strategies are introduced to improve the construction of the combined graph.

reported to show the highest contrast between the blood vessels and background [50]. A steerable first order derivative of Gaussian filter is used to implement the kernel [51]. The steerable filter is able to find the gradient along different angles at different locations. The separable first order derivative of Gaussian along the x-axis and along the y-axis are given by $G_1^{0^\circ}$ and $G_1^{90^\circ}$. The first order derivative of Gaussian along any ngle θ is defined in Equation 5.5.

$$G_1^{\theta} = \cos(\theta)G_1^{0^\circ} + \sin(\theta)G_1^{90^\circ}, \tag{5.5}$$

where σ_x and σ_y are the *scale* of the first order derivative kernel along the x-axis and y-axis. Because equations 4.1 and 4.2 are separable kernels, the original image is first convolved with $G_1^{0^\circ}$ and $G_1^{90^\circ}$ to get the first order derivative image along the x-axis and y-axis. Then within each normal profile, the weights of the profile nodes are calculated according to equation 4.3. In our implementation, the gradient is computed along the graph column direction, i.e., the direction of the electric lines of force at each graph node location.

5.2.4 Graph Search and Boundary Determination

In order to keep the vessel boundaries smooth, the branching unit is constructed as three independent single slice graphs. Intra-column smoothness constraints are set to maintain the smoothness within the slice. After the graphs are built, the optimal segmentation is found and the vessel boundary is determined as described by Li *et al.* [49].

Once the three boundaries are determined, the vessel width can be measured as the Euclidean distance between the graph nodes on the optimal segmentation from the same centerline pixel, as illustrated in Figure 5.4.

5.2.5 Graph Search for the Whole Vessel Tree

Different graph construction methods are used for straight vessels and for branching points and the graphs are solved independently. In order to keep the consistency of the vessel width measurement result, the two methods need to be combined.

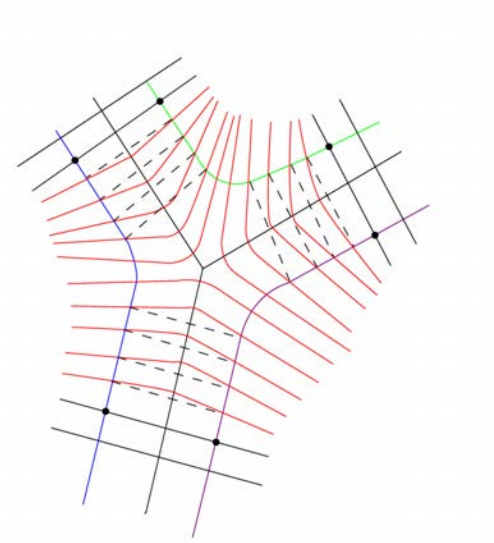

Figure 5.4: Illustration of graph construction, cost function design, and vessel width measurement at branching point. Three graphs are built for the three boundaries separately, as shown in color green, blue, and purple. The black dots denote the end of straight vessel segment and start of branching vessel segment. Low cost is given to those nodes to fix the ends of the boundaries at branching point. After the three boundaries are determined, the vessel width is measured as the Euclidean distance between the corresponding nodes from the same centerline pixel.

Starting from the vessel centerline image, branching points are detected and all sub-branches are traced for certain length, as described in Section 5.2.1. Then, the branching points and sub-branches are excluded from the vessel centerline image and leave the straight vessels as separate vessel segments. The vessel widths of straight vessel segments are measured using the method described in an earlier paper [61]. After that, for each branching point, if adjacent straight vessels are found, then the start node of the graph is forced to be the same as the node on the optimal segmentation from the straight vessel width measurement result. This is accomplished by giving low cost to the node that is force to be on the optimal segmentation. If no

adjacent straight vessels are found, then no restriction is placed on the start node. By doing this, a consistent vessel width measurement is given for the whole vessel tree.

5.3 Experimental Methods

A set of 100 artery branchings and 100 vein branchings were selected from 50 fundus images from 50 normal subjects were used to assess the vessel width measurement performance. The image resolution is 2196×1958 pixels, and stored as DICOM format. For each fundus image, two artery branchings and two vein branchings were selected to evaluate the algorithm. The two observers are denoted as E_1 and E_2 respectively. For each branching, at least three measurement profiles were given to each of the three branches from each observer. Each measurement profile contains seven outputs: image name, image index, branch index, x_1, y_1, x_2, and y_2. The branch center is defined as $(x_k, y_k) = (\frac{1}{2n}\sum_{i=1}^{n}(x_{1i} + x_{2i}), \frac{1}{2n}\sum_{i=1}^{n}(y_{1i} + y_{2i}))$ and the width of the branch is defined as $w_k = \frac{1}{n}\sum_{i=1}^{n}\sqrt{(x_{1i} - x_{2i})^2 + (y_{1i} - y_{2i})^2}$, where $i = 1, ..., n$ is the number of measurement at the given branch and $k = 1, 2$ denotes the two observers. Figure 5.5 is given to better illustrate the relationship.

The parent branch-daughter branch relationship was explored on a dataset of 544 independent subjects from the Tromsø study in Norway. The Tromsø study is a population-based cohort from a single village in Norway ages 55-85 that has been studied and was retinally images during 2003-2006. The de-identified images and linked clinical parameters was given in DICOM format.

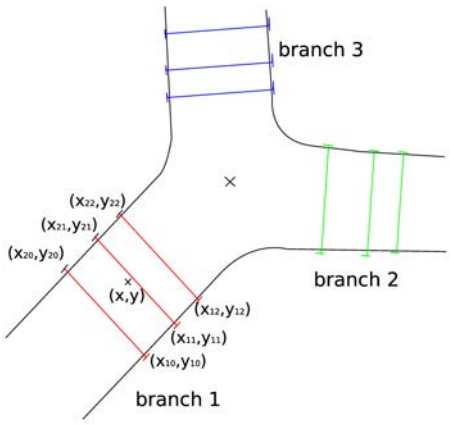

Figure 5.5: Illustration of the ground truth generation. Suppose the red, green, and blue lines are vessel width manually marked for branch 1 by one observer. The vessel width for branch 1 is calculated as the average of the three width profiles. The branch center for branch 1 is calculated as the average of the three width profile center.

The vessel segmentation images for each image was created and the vessel width was measured and superimposed on the original color fundus image. A human expert was invited to locate the parent branch center for each valid branch and label it as an artery or a vein. This was done on a tablet-based color fundus image evaluation system ([63]) and the interface is shown in Figure 5.6.

5.4 Results

Typical vessel width measurements are shown in Figure 5.7. Red lines denote the vessel width measurement for branching points. Black lines denote the vessel width measurement for straight vessels.

We compared the performance of our algorithm with the performance of the two human observers. As mentioned, the branch center is defined as (x_k, y_k), where

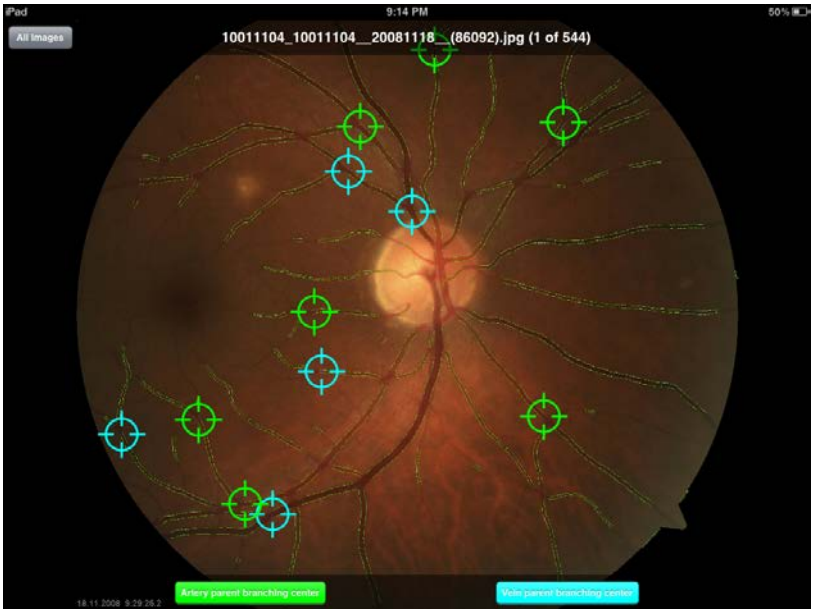

Figure 5.6: Illustration of the tablet-based image evaluation system. The human observer is able to locate the center of parent branch center and label it as an artery or a vein.

$k = 1, 2$ are the two observers. Similarly, we determine the branch center calculated in our algorithm as $(x_{alg}, y_{alg}) = (\frac{1}{2n}\sum_{i=1}^{n}(x_{1i} + x_{2i}), \frac{1}{2n}\sum_{i=1}^{n}(y_{1i} + y_{2i}))$, where n is the number of measurement profiles given by the algorithm. When the performance is compared, (x_1, y_1), (x_2, y_2), (x_{alg}, y_{alg}) are matched. A match is considered successful if the Euclidean distance between the two center is less than 10 pixels. The match could fail when (x, y) is too far from either (x_1, y_1) or (x_2, y_2), or (x_1, y_1) and (x_2, y_2) are too far from each other. The performance for a branching is considered as valid if the matches of all the three branches are successful. Among the 200 branchings,for three of them the algorithm failed to match all the branches, so the success rate is 98.5%. The vessel width is compared for the valid branchings. The average of w_1 and w_2 is considered as the ground truth for comparison and is denoted as AVE in

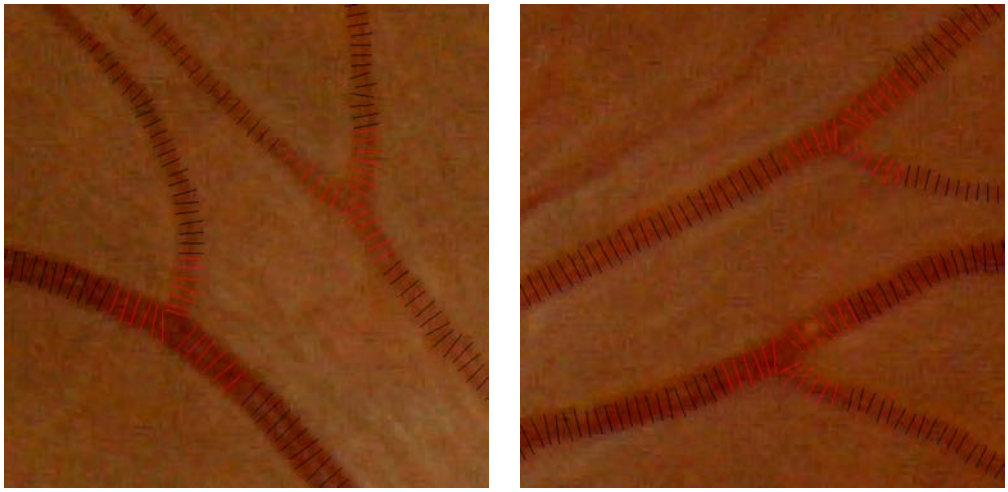

(a) (b)

Figure 5.7: Typical vessel width measurement images. Red lines denote the vessel width measurement for branching points. Black lines denote the vessel width measurement for straight vessels.

Table 5.2. The result of the comparison is given in Table 5.1. branch_1, branch_2 and branch_3 are the three branches.

Table 5.1: Comparison of the performances between human experts and presented method (Vessel widths are in pixels. E_1 and E_2 denote the two human experts. Alg denotes the presented method. μ and σ are the mean and standard deviation of vessel width measurements).

	branch_1		branch_2		branch_3	
	μ	σ	μ	σ	μ	σ
E_1	18.24	4.82	14.57	4.53	13.37	3.66
E_2	19.40	4.94	16.01	4.34	14.39	3.52
Alg	18.41	4.81	14.75	4.20	13.78	3.69

The signed error and unsigned error are given in Table 5.2. branch_1, branch_2 and branch_3 are the three branches.

Table 5.2: Comparison of the performance between human experts and presented method (Signed error and unsigned error are in pixels. E_1 and E_2 denote the two human experts. *Alg* denotes the presented method. *Ave* denotes the average measurements of the two human experts. μ and σ are the mean and standard deviation of errors).

		E_1 vs. E_2			Alg vs. Ave		
		$branch_1$	$branch_2$	$branch_3$	$branch_1$	$branch_2$	$branch_3$
Signed Error	μ	-1.160	-1.440	-1.026	-0.408	-0.532	-0.102
	σ	1.557	1.882	-1.932	-1.670	-1.895	-2.090
Unsigned Error	μ	1.544	1.884	1.695	1.253	1.480	1.534
	σ	1.176	1.435	1.378	1.174	1.294	1.419

The scatter plots are given in Figure 5.8 and arteries and veins were plotted separately. Pearson's correlation was given to quantify how good the performances were linearly correlated. The correlation was lower for artery branchings between both the algorithm and ground truth, and between two observers, as shown in Figure 5.8 (a) and (b). The Bland-Altman plots are given in Figure 5.9.

5.4.1 Parent Branch-Daughter Branch Relationship

The measured branch was matched with the annotation from human experts and only the matched branch was involved in further analysis. A number of 4607 branch points were matched, among which 1703 were arteries and 2904 were veins. First, a linear regression was done to show whether parent branch-daughter branch relationship conform to Murray's. Then a comparison between different models was given.

Murray's power relationship is based on the hypothesis that calibers of daughter branches are smaller than the caliber of parent branch. Hence, branches that has

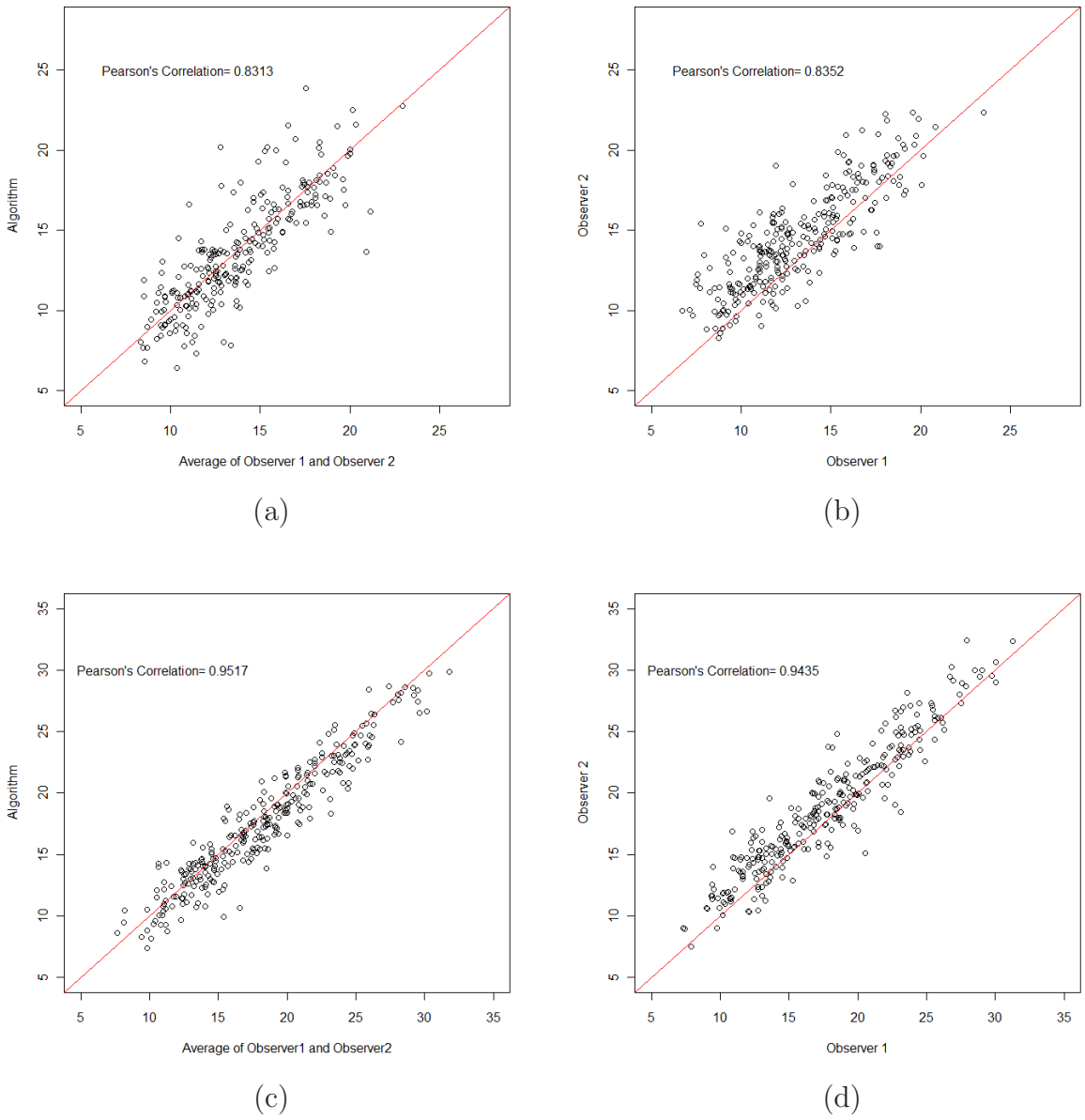

Figure 5.8: Vessel width measurement scatter plots. (a) The scatter plot of vessel width measured by automatic algorithm and the average of vessel width given by observer 1 and observer 2 for artery branchings. (b) The scatter plot of vessel width measurement performed by observer 1 and observer 2 for artery branchings. (c) The scatter plot of vessel width measured by automatic algorithm and the average of vessel width given by observer 1 and observer 2 for vein branchings. (d) The scatter plot of vessel width measurement performed by observer 1 and observer 2 for vein branchings.

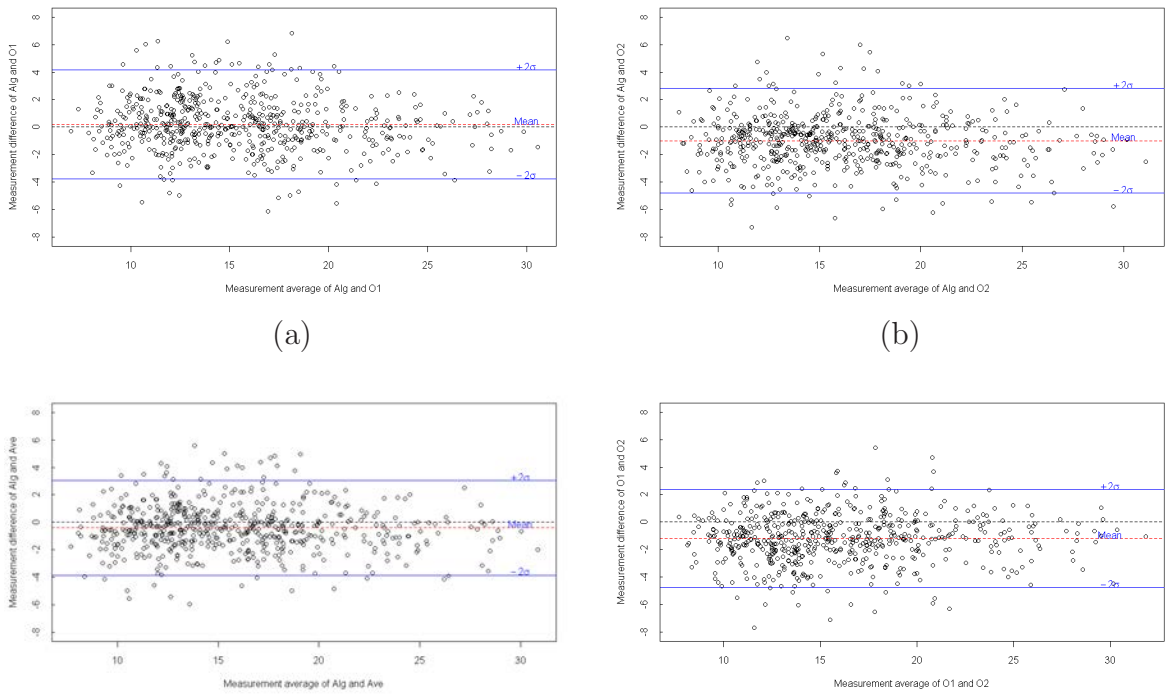

Figure 5.9: Bland-Altman plots. (a) Bland-Altman plot of proposed method and observer 1. (b) Bland-Altman plot of proposed method and observer 2. (c) Bland-Altman plot of proposed method and the average of observer 1 and observer 2. (d) Bland-Altman plot of observer 1 and observer 2.

a larger daughter branch comparing with parent branch was excluded in this analysis. The result is shown in Figure 5.10. The total number of artery branch is 1145 and the number for vein is 2527. Figure 5.10 (a) shows that the arterial parent branch-daughter branch relationship conforms to the Murray's law. The best fitting for vein was found at $x = 2.3$, which deviates from the Murray's law. The Bland-Altman plot is given in Figure 5.11.

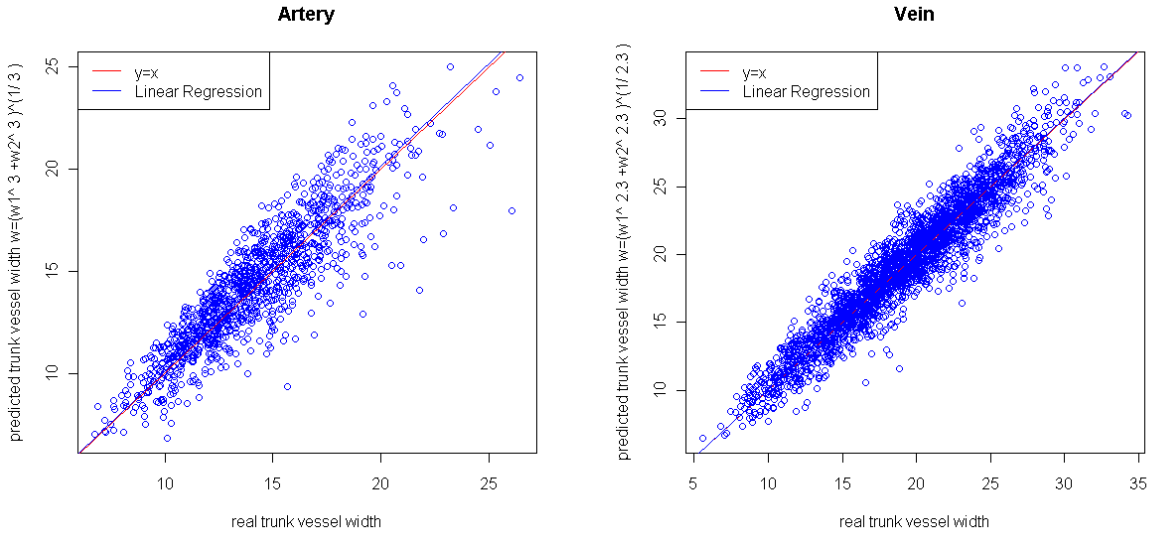

(a) (b)

Figure 5.10: Scatter plot of the measured vessel width and predicted vessel width by applying the model $d^x = d_1^x + d_2^x$, where d is the caliber of parent branch and d_1, d_2 are the calibers of daughter branches. (a) The best fitting for arterial branch was found at $x = 3$, which conforms to the Murray's law. (b) The best fitting for venous branch was found at $x = 2.3$ which deviates from the Murray's law.

The parent branch-daughter branch relationship was also analyzed by finding the best fitting value x for each branch and then check the distribution of it. For each

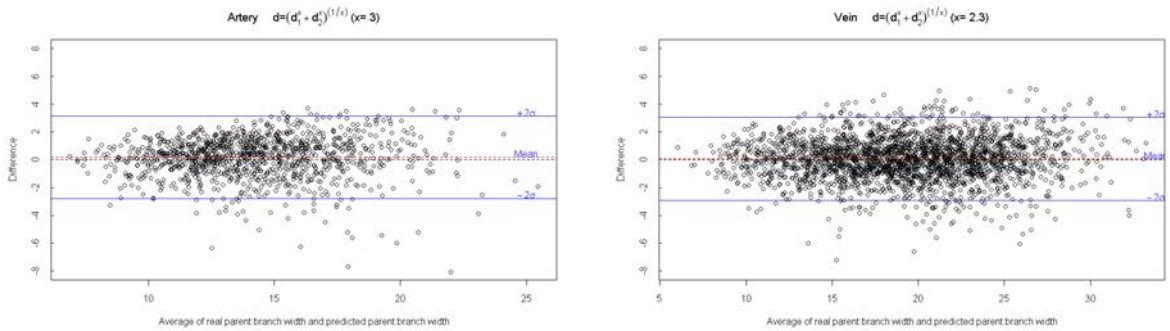

(a) (b)

Figure 5.11: Bland-Altman plots of real parent branch width and predicted parent branch width. Predicted parent branch width calculated by $d = (d_1^x + d_2^x)^{1/x}$, where d_1 and d_2 are the calibers of two daughter branches. (a) Bland-Altman plot of arterial branch points. $x = 3$. (b) Bland-Altman plot of venous branch points. $x = 2.3$.

branch point, the best fitting power x ranging from 1 to 6, with a step of 0.1 was found. When the fitting power x is larger than 6, it becomes very sensitive to small measurement errors [25], as illustrated in Table 5.3. Table 5.3 contains a number of examples to show how the fitting power becomes very sensitive to small vessel width changes when $x > 6$. For instance, when $d_1 = 15, d_1 = 7$, a parent branch caliber of $d = 10.18$ pixels result in a fitting power of $x = 6$. A small changes of the parent branch caliber of 0.15 pixels (from 10.18 pixels to 10.03 pixels) will result in a fitting value of $x = 10$. Hence, the branch with a value $x > 6$ is regarded as outliers and excluded in this study. Figure 5.12 shows the result. A number of 138 arterial branch points (out of 1145) and 35 venous branch points (out of 2527) were excluded. The mean value for arterial branch point is $x = 3.07 \pm 1.13$ and $x = 2.39 \pm 0.80$ for venous branch.

The performances of different models were also compared. The results are

Table 5.3: Simulated branch point vessels to illustrate the relationship between vessel width and corresponding fitting power x in model $d^x = d_1^x + d_2^x$, where d is the diameter of parent branch in pixels, d_1, d_2 are the diameters of children branches in pixels.

	d			
	x=3	x=6	x=10	x=20
$d_1 = 15, d_2 = 7$	15.49	15.03	15.0007	15.0000
$d_1 = 10, d_2 = 7$	11.03	10.18	10.03	10.003
$d_1 = 10, d_2 = 7$	6.30	5.61	5.36	5.18

given in Figure 5.13 and Table 5.4.

Table 5.4: Comparison of the performances of different parent branch-daughter branch relationship models ($\mu \pm \sigma$ in μm).

Model	Murray's Model	Parr-Hubbard Model	Knudtson Model
	$d^3 = d_1^3 + d_2^3$	$W_a = (0.87w_1^2 + 1.01w_2^2 - 0.22w_1w_2 - 10.76)^{1/2}$	$\hat{W}_a = 0.88 \times (w_1^2 + w_2^2)^{1/2}$
Artery	-4.77±8.59	-6.27±8.79	-3.19±8.53
	$d^{2.3} = d_1^{2.3} + d_2^{2.3}$	$W_v = (0.72w_1^2 + 0.91w_2^2 + 450.05)^{1/2}$	$\hat{W}_v = 0.95 \times (w_1^2 + w_2^2)^{1/2}$
Vein	-1.84±7.68	-1.30 ± 7.51	-0.70±7.65

5.5 Discussion

We proposed a vessel width measurement method for branch points on retinal images. Performance of the fully automatic method was comparable with human observers' performance. Figure 5.8 shows that both the human observers and the automatic method have low performance for artery branch points. One reason might be that arteries have a lower contrast with the background while veins usually have a better contract with the background. Figure 5.14 shows a typical artery branch and

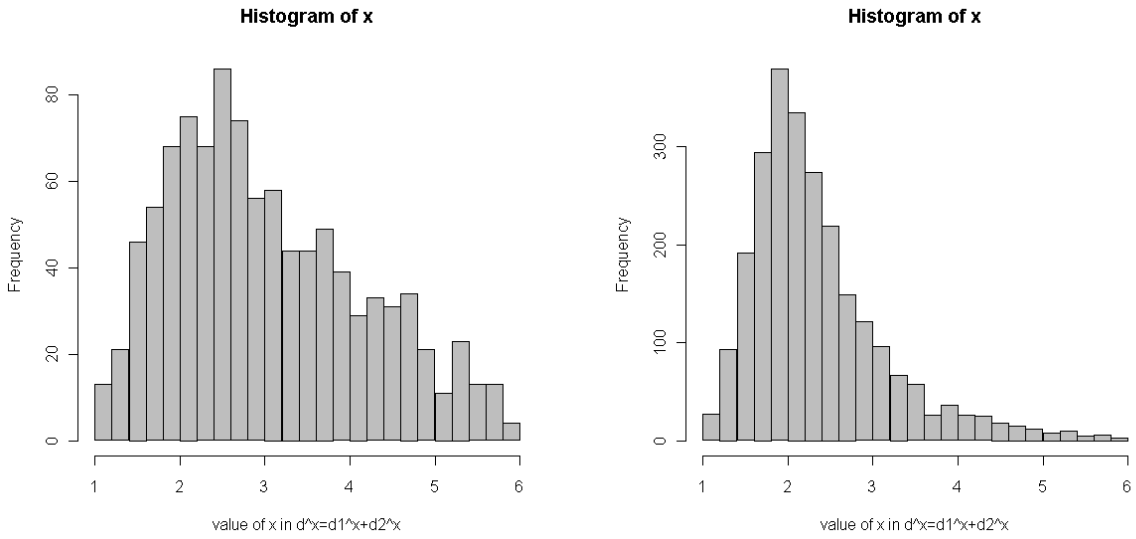

(a) (b)

Figure 5.12: Histograms of fitting power x in model $d^x = d_1^x + d_2^x$. (a) Histogram of arterial branch points. (b) Histogram of venous branch points.

a typical vein branch. The venular boundaries are better defined for both observers and automatic methods.

5.5.1 Parent Branch-Daughter Branch Relationship

There are two basic characteristics of different models: 1. whether a smaller parent branch vessel width is allowed; 2. whether the model passes through (0,0), meaning when the diameters of two daughter branches approach zero, the diameter of parent branch also approaches zero. Murray's junctional exponent model, which was initially only proposed for artery, passes through (0,0), but it does not allow a larger parent branch. In the Parr-Hubbard model, both the model for artery branches and the model for vein branches don't passes through (0,0). It allows a larger arterial parent branch but not a larger venous parent branch. Knudtson's revised model, on

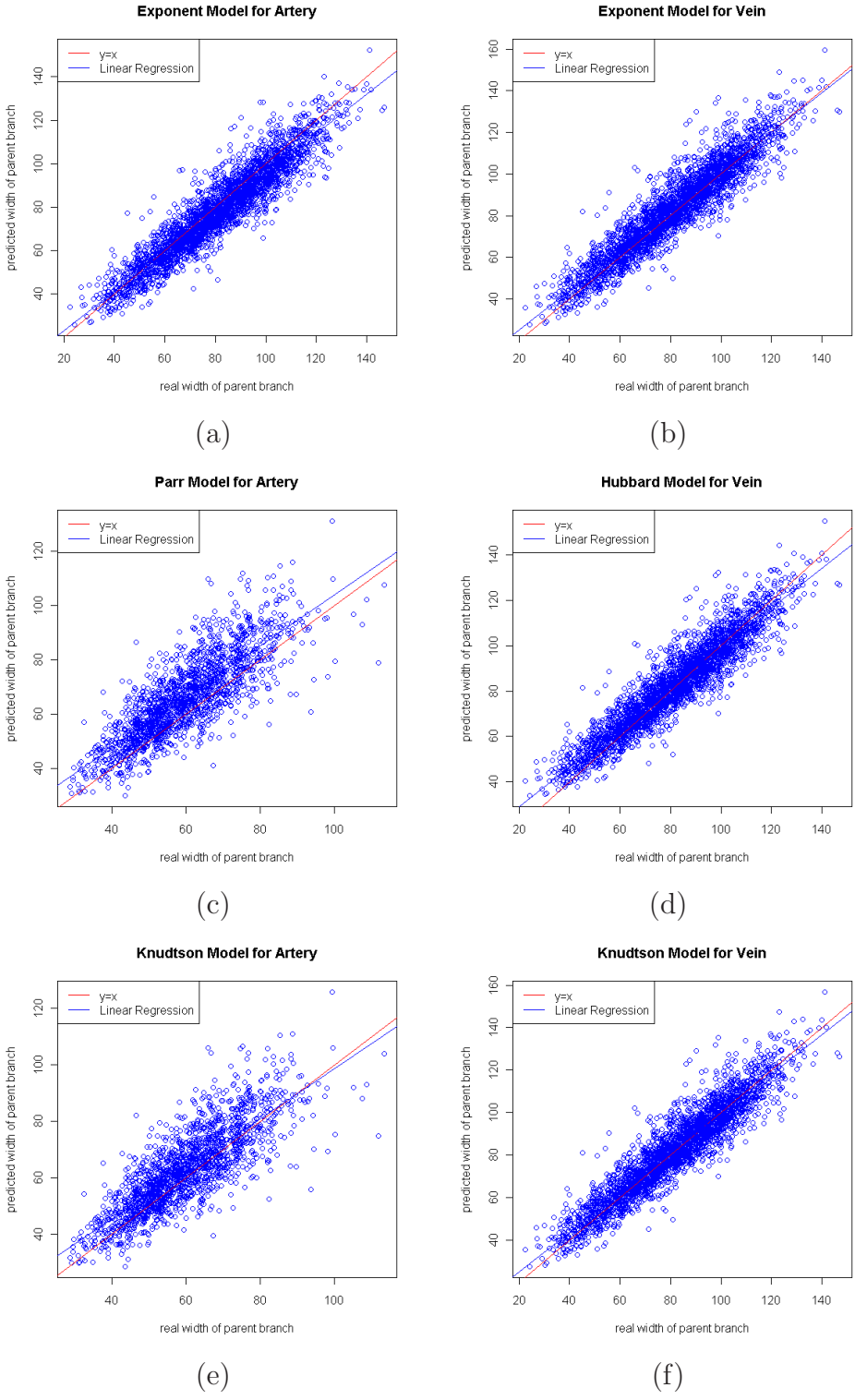

Figure 5.13: Comparison of the performance of different models. (a), (b) Murray's junctional exponent model for artery and vein. (c), (d) Parr-Hubbard model for artery and vein. (e), (f) Knudtson's revised model for artery and vein.

(a) (b)

Figure 5.14: Examples of typical arterial branching and venule branching. Arteries usually have a lower contrast with the background comparing with veins. (a) A typical arterial branching. (b) A typical venule branching.

the other hand, satisfies both characteristics. It passes through (0,0) and allows a smaller parent branch for both artery and vein.

Hence, when the condition of a larger parent branch was excluded from the parent branch-daughter branch relationship study, the Murray's junctional exponent explains the arterial parent branch-daughter branch relationship precisely. Otherwise, the Knudtson's revised model performs slightly better than the other two models.

As mentioned, the Murray's model suffers from the limits that a small measurement error will result in big error in fitting x. The smaller the difference between diameters of parent branch and daughter branch, the more sensitive the model is. When daughter branch becomes larger than the parent branch, the model fails completely. Figure 5.15 shows two branches where the algorithm gave a larger daughter

branch vessel width than a parent branch vessel width. Branches with white circles are parent branches. We can see in these branches, the daughter branches have comparable vessel width with the parent branches. Then a slight measurement error will result in the failure of Murray's model.

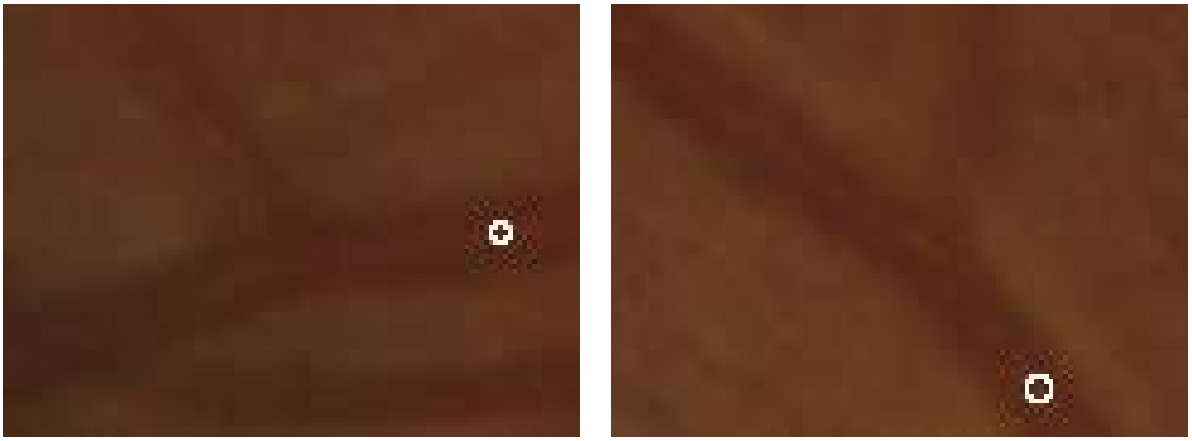

(a) (b)

Figure 5.15: Example images with similar diameters of parent branch and daughter branch. Branches with white circles denotes parent branches.

5.5.2 Computational Performance

This method also has a nice computational performance. For a retinal image of size 2196×1958 pixels, the vesselness map generation takes about 100 seconds. The image centerline image generation takes less than 10 seconds. The average number of straight vessel segments on the image is 90 and the number of branching is around 30. It takes around 17 seconds to solve the graph for straight vessels and about 9 seconds to solve the graph for branch points. In total, it takes approximately 130

seconds to process one image.

5.5.3 Limitations

This method also suffers from some limitations. It relies largely on the quality of the vessel centerline image. If the vessel centerline, which is generated from the vesselness map, has a branching pattern that is very different with the real branching pattern, the ELF computation will be incorrect and leads to less reliable measurement result. The electric field theory based method is computationally intractable for large scale problems. ELF computation time increases exponentially with the increase in the number of vertices [64]. It is also easily influenced by noise as the location of each positive charges influences the computation of every electric line of force in the electric field. In order to alleviate these problems, the implementation of the electric field theory based graph construction method is limited to only each branching region, rather than the whole vessel tree.

CHAPTER 6
DISCUSSION

A state-of-the-art system of system for retinal vessel delineation and quantitative analysis is presented in this thesis. This system was validated on a number of datasets, with a wide variety in image resolutions and qualities. The results of our evaluation showed that the vessel boundary delineation was accurate and comparable to the performance of human experts.

There are several advantages of the presented system. First, this is the first fully automated vessel width quantification algorithm for both straight vessel segments and branch points. As discussed in Section 5.2, in most retinal branching studies, the vessel width was measured using manual or semi-automatic methods. The lack of a fully automated vessel width measurement method has restricted retinal vessel quantitative study into very limited datasets. On the other hand, the presented method enables the study in much larger datasets. For instance, the vessel width changes with regard to the optic disc was carried out on a dataset of 600 color fundus images and the parent branch-daughter branch relationship was on a dataset of 544 color fundus images.

Second, the algorithm is accurate and comparable to the performance of human experts in a number of tested datasets, while with a much better computational performance, as discussed in Section 4.5 and Section 5.5. For instance, it takes about 110 seconds to create the vessel segmentation map, 20 seconds to generate the vessel centerline image, and about 40 seconds to solve all the graphs in an image of size

2160 × 1440 pixels, with an average of 160 vessel segments, resulting a total running time of less than 3 minutes. On the other hand, the manual measurement of all vessel segments in an image of similar resolution is too laborious that no comparison time is available.

There are also several limitations of this system. First, This algorithm relies largely on the vessel segmentation result. If the vessel centerline image exhibits a false positive vessel segment, the algorithm will still try to delineate the vessel boundaries and hence lead to meaningless measurement result. Second, it tends to have a better performance in venous vessel measurement, compared with arterial vessel measurement. Arteries usually have a lower contrast to the background comparing with veins, which leads to a lower performance for both the algorithm and human observers. It also tends to be biased towards showing a smaller measurement for smaller vessels, as discussed in Section 4.5. The most likely explanation is that the vessel width measurement is done with a fixed scale parameter σ, while the optimal measurement of vessels in different scales need different scale parameters. This problem can be solved by applying a multi-scale cost function.

6.1 Future Work

The methods presented in this thesis have a number of potential applications. One of the most important applications of this method is the measurement of arteriole-to-venule ratio (AVR) in the retinal image.

There were mainly two formulas used in the past AVR study, the Parr-Hubbard

formulas and the Knudtson's revised formulas. Both formulas have limitations. For the Parr-Hubbard formulas, Knudtson claimed that the Parr-Hubbard formulas will lead to spurious variability in the estimation. For example, the calculation allows contributions of a variable number of vessel diameters for each eye to the overall estimate of vessel caliber. The association between the number of vessels included in the calculation and the magnitude of summary estimates potentially decreases the ability to discern real biological association of vessel caliber. Knudtson also claimed that the formulas include constant terms in their equations, which in turn cause the result to be dependent upon the units of measurement.

However, the Knudtson's revised formulas also suffers from some limitations. First of all, the calculation of CRAE and CRVE is limited to only the six largest arterioles and venules, which may be a waste of information if more arterioles or venules are able to be measured on the image. Secondly, vessel width measurement was only performed within a circular region centered at the optic disc (Figure 6.1, Zone B). The obvious drawback of this approach is the AVR changes at smaller blood vessels, which normally locate outside Zone B will not get measured at all. Last but not least, the branching coefficient was developed using the semi-automatic software, the same as what they used for further application, which we think weaken the reliability of the formulas.

On the other hands, the Parr-Hubbard formulas is more basic and usable. First of all, though the formulas depend on the unit used in the measurement, we can easily convert one unit into another unit. Secondly, if we are considering the AVR,

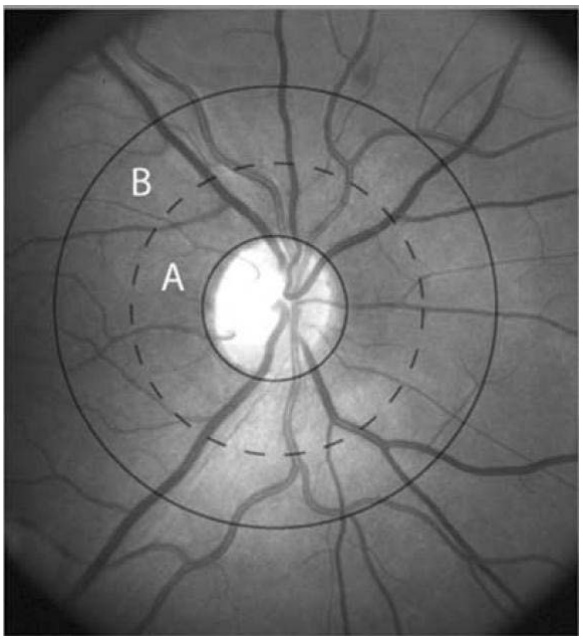

Figure 6.1: Illustration of the region used to calculate AVR in Knudtson's revised formulas.

instead of separate parameters as CRAE and CRVE, we expect the number of blood vessels would not have a big influence on the final estimation. To further address this problem, we propose Equation 6.1 and 6.2 to normalize the CRAE and CRVE with respect to the number of blood vessels included in the calculation. Suppose m_a arterioles and m_v venules are detected at the edge of the optic disc, where the vessel trees are excluded if they only contain one vessel segment. We propose the following formulas to calculate the CRAE and CRVE. Besides the normalization method, simply keep the number of included arterioles and venules the same is expected to eliminate the problem. Hence, if the normalized formulas does not work as expected, we will keep the number of arterioles and venules the same and use the original Parr-Hubbard

formulas to calculate the AVR.

$$W_a = \frac{(0.87w_1^2 + 1.01w_2^2 - 0.22w_1w_2 - 10.76)^{1/2}}{m_a}, \tag{6.1}$$

$$W_v = \frac{(0.72w_1^2 + 0.91w_2^2 + 450.05)^{1/2}}{m_v} \tag{6.2}$$

Except for the measurement described above, some other parameters can also be measured for the AVR, for example, a general AVR changes with regard to the geodesic distance to the optic disc.

CHAPTER 7
CONCLUSION

A fully automated and highly robust retinal vessel delineation and quantitative analysis method in fundus image was presented. The presented method was able to precisly measure vessel parameters for both straight vessel segments and for branch points.

This novel method modeled the vessel boundary delineation problme in two-dimension into an optimal surface segmentation problem in three-dimension. Then the optimal surface segmentation problem was transformed into finding a minimum-cost closed set problem in a vetex-weighted geometric graph (Chapter 4). Furthermore, an improved electric field theoretic method was applied to better adjust the graph for branch points (Chapter 5). This method was validated on a wide range of datasets with a diversity in image resolution and image quality. The results showed that the algorithm was of high accuracy and robustness.

A simultaneous optic disc and fovea detection method was also presented to facilitate the retinal vasculature analysis (Chapter 3). The location information can be used in a number of other retinal image analysis projects.

A number of retinal vasculature analysis was provided as applications of presented methods. Vessel width with regard to the distance to optic disc center was explored and a monotonic decrease was observed. Branching coefficient for arterioles and venules was studied and found to be different. At last, a few more potential applications were discussed as the future work. This approach showed to be promising

in multiple applications in the field of reitnal vessel quantitative analysis.

REFERENCES

[1] "Anatomy of the eye." http://www.eyesandeyesight.com/2009/02/anatomy-of-the-eye/.

[2] "Visual system: Light path." http://en.wikipedia.org/wiki/File:Eye-diagram.png.

[3] A. C. van Trigt, "Dissertatio ophthalmologica inauguralis de speculo oculi," *Trajecti ad Rhenum*, 1853.

[4] "Cjroyle opticians: Fundus camera." `http://www.cjroyleopticians.co.uk/html/services.html`.

[5] A. M. Miller, "Eyewiki." http://eyewiki.aao.org/Fluorescein_Angiography/, 02 2012.

[6] B. Hoffmann, "Ultrasound guide for emergency physicians." http://www.sonoguide.com/smparts_ocular.html, 2008.

[7] Wikipedia, "retina oct." http://en.wikipedia.org/wiki/File:Retina-OCT800.png.

[8] T. Y. Wong, F. M. Islam, and R. Klein, "Retinal vascular caliber, cardiovascular risk factors, and inflammation: The multiethnic study of atherosclerosis (MESA)," *Investigative Ophthalmology and Visual Science*, vol. 47, no. 6, pp. 2341–2350, 2006.

[9] M. Niemeijer, J. Staal, B. van Ginneken, M. Loog, and M. D. Abràmoff, "Comparative study of retinal vessel segmentation methods on a new publicly available database," *SPIE Medical Imaging*, vol. 5370, pp. 648–656, 2004.

[10] L. Sherwood, *Human Physiology-From Cell to Systems*. Jack Carey, 2001.

[11] N. Patton, T. M. Aslam, T. MacGillivray, I. J. Deary, B. Dhillon, R. H. Eikelboom, K. Yogesan, and I. J. Constable, "Retinal image analysis: Concepts, applications and potential," *Progress in retinal and eye research*, vol. 07, pp. 100–127, 2005.

[12] S. S. Hayreh, "Hypertensive retinopathy," *Ophthalmologica*, vol. 198, no. 4, pp. 173–177, 1989.

[13] M. D. Abràmoff, M. K. Garvin, and M. Sonka, "Retinal imaging and image analysis," *IEEE Reviews in Biomedical Engineering*, vol. 3, pp. 169–208, 2010.

[14] L. D. Hubbard, R. J. Brothers, W. N. King, L. X. Clegg, R. Klein, L. S. Cooper, A. R. Sharrett, M. D. Davis, and J. Cai, "Methods for evaluation of retinal microvascular abnormalities associated with hypertension/sclerosis in the atherosclerosis risk in communities study," *Ophthalmology*, vol. 106, pp. 2269–2280, 1999.

[15] R. Webb and G. Hughes, "Scanning laser ophthalmoscope," *IEEE Transaction on Biomedical Engineering*, vol. 28, no. 7, pp. 488–492, 1981.

[16] Retina Macula Institute, "Ocular ultrasound." http://www.retinamaculainstitute.com/technology/ocular-ultrasound.

[17] H. G. Bezerra, M. A. Costa, G. Guagliumi, A. M. Rollins, and D. I. Simon, "Intracoronary optical coherence tomography: A comprehensive review: Clinical and research applications," *JACC Cardiovascular Interventions*, vol. 2, pp. 1035–1046, 2009.

[18] T. Y. Wong, R. Klein, A. R. Sharrett, B. B. Duncan, D. J. Couper, J. M. Tielsch, B. E. K. Klein, and L. D. Hubbard, "Retinal arteriolar narrowing and risk of coronary heart disease in men and women," *JAMA*, vol. 287, no. 9, pp. 1153–1159, 2002.

[19] C. Sun, J. J. Wang, D. A. Mackey, and T. Y. Wong, "Retinal vascular caliber: Systemic, environmental, and genetic associations," *Survey Ophthalmol*, vol. 48, no. 3, pp. 245–255, 2003.

[20] J. C. Parr and G. F. S. Spears, "Mathematic relationship between the width of a retinal artery and the width of its branches," *Am. J. Ophthalmol.*, vol. 77, no. 4, pp. 478–483, 1974.

[21] B. Gopinath, L. A. Baur, J. J. Wang, E. Teber, G. Liew, N. Cheung, T. Y. Wong, and P. Mitchell, "Blood pressure is associated with retinal vessel signs in preadolescent children," *Journal of Hypertension*, vol. 28, no. 7, pp. 1406–1412, 2010.

[22] B. Gopinath, L. A. Baur, E. Teber, G. Liew, T. Y. Wong, and P. Mitchell, "Effect of obesity on retinal vascular structure in pre-adolescent children," *International Journal of Pediatric Obesity*, vol. 6, no. 2, pp. 353–359, 2011.

[23] L.-J. Li, C. Y.-L. Cheung, Y. Liu, A. Chia, P. Selvaraj, X.-Y. Lin, Y.-M. Chan, R. Varma, P. Mitchell, T.-Y. Wong, and S.-M. Saw, "Influence of blood pressure on retinal vascular caliber in young children," *Ophthalmology*, vol. 118, no. 7, pp. 1459–1465, 2011.

[24] F. N. Doubal, R. de Haan, T. J. MacGillivray, P. E. Cohn-Hokke, B. Dhillon, M. S. Dennis, and J. M. Wardlaw, "Retinal arteriolar geometry is associated with cerebral white matter hyperintensities on magnetic resonance imaging," *International Journal of Stroke*, vol. 5, pp. 434–439, 2010.

[25] N. Chapman, G. Dell'Omo, M. Sartini, N. Witt, A. Hughes, S. Thom, and R. Pedrinelli, "Peripheral vascular disease is associated with abnormal arteriolar diameter relationships at bifurcations in the human retina," *Clinical Science*, vol. 103, pp. 111–116, 2002.

[26] A. V. Stanton, B. Wasan, A. Cerutti, S. Ford, R. Marsh, P. P. Sever, S. A. Thom, and A. D. Hughes, "Vascular network changes in the retina with age and hypertension," *Journal of Hypertension*, vol. 13, pp. 1724–1728, 1995.

[27] N. Patton, T. M. Aslam, T. MacGillivray, A. Pattie, I. J. deary, and B. Dhillon, "Retinal vascular analysis as a potential screening tool for cerebrovascular disease: a retionale based on homology between cerebral and retinal microvasculatures," *Journal of Anatomy*, vol. 206, pp. 319–348, 2005.

[28] M. D. Knudtson, K. E. Lee, L. D. Hubbard, T. Y. Wong, R. Klein, and B. E. K. Klein, "Revised formulas for summarizing retinal vessel diameters," *Current Eye Research*, vol. 27, no. 3, pp. 143–149, 2003.

[29] J. C. Parr and G. F. S. Spears, "General caliber of the retinal arteries expressed as the equivalent width of the central retinal artery," *Am. J. Ophthalmol.*, vol. 77, no. 4, pp. 472–477, 1974.

[30] N. Patton, T. M. Aslam, T. MacGillivray, B. Dhillon, and I. J. Constable, "Asymmetry of retinal arteriolar branch widths at junctions ability of formulae to predict trunk arteriolar widths," *Investigative Ophthalmology and Visual Science*, vol. 47, no. 4, pp. 1329–1333, 2006.

[31] A. D. Fleming, K. A. Goatman, S. Philip, J. A. Olson, and P. F. Sharp, "Automatic detection of retinal antomy to assist diabetic retinopathy screeing," *Physics in Medicine and Biology*, vol. 52, pp. 331–345, 2007.

[32] M. Foracchia, E. Grisan, and A. Ruggeri, "Detection of optic disc in retinal images by means of a geometrical model of vessel structure," *IEEE Transactions on Medical Imaging*, vol. 23, no. 10, pp. 1189–1195, 2004.

[33] A. Hoover and M. Goldbaum, "Locating the optic nerve in a retinal image using the fuzzy convergence of the blood vessel," *IEEE Transactions on Medical Imaging*, vol. 22, no. 8, pp. 951–958, 2003.

[34] H. Li and O. Chutatape, "Automated feature extraction in color retinal images by a model based approach," *IEEE Transactions on Biomedical Engineering*, vol. 51, no. 2, pp. 246–253, 2004.

[35] J. Lowell, A. Hunter, D. Steel, A. Basu, R. Ryder, and E. Fletcher, "Optic nerve head segmentation," *IEEE Transactions on Medical Imaging*, vol. 23, pp. 256–264, 2004.

[36] M. Niemeijer, M. D. Abràmoff, and B. van Ginneken, "Automated localization of the optic disc and the fovea," *IEEE EMBS Conference*, pp. 3583–3541, 2008.

[37] C. Sinthanayothin, J. Boyce, H. Cook, and T. Williamson, "Automated localisation of the optic disc, fovea, and retinal blood vessels from digital colour fundus images," *British Journal of Ophthalmology*, vol. 83, no. 11, pp. 902–910, 1999.

[38] K. Tobin, E. Chaum, V. Govindasamy, and T. Karnowski, "Detection of anatomic structures in human retinal imagery," *IEEE Transactions on Medical Imaging*, vol. 26, no. 12, pp. 1729–1739, 2007.

[39] X. Xu, M. K. Gravin, M. D. Abràmoff, and J. M. Reinhardt, "Simultaneous automatic detection of the optic disc and fovea on fundus photographs," *SPIE Medical Imaging*, 2011.

[40] M. Sonka, V. Hlavac, and R. Boyle, *Image Processing, Analysis, and Machine Vision*. New York: PWS, 1998.

[41] P. Pudil, F. Ferri, J. Novovicova, and J. Kittler, "Floating search methods in feature selection," *Pattern Recognition Letters*, vol. 15, no. 11, pp. 1119–1125, 1994.

[42] J. Staal, M. D. Abràmoff, M. A. Viergever, and B. van Ginneken, "Ridge-based vessel segmentation in color images of the retina," *IEEE Transactions on Medical Imaging*, vol. 23, no. 4, pp. 501–509, 2004.

[43] L. Gang, O. Chutatape, and S. M. Krishnan, "Detection and measurement of retinal vessel in fundus images using amplitude modified second-order Gaussian filter," *IEEE Transactions on Biomedical Engineering*, vol. 49, no. 2, pp. 168–172, 2002.

[44] M. Lalonde, L. Gagnon, and M. C. Boucher, "Non-recursive paired tracking for vessel extraction from retinal images," *Proceeding of the Conference Vision Interface*, pp. 61–68, 2000.

[45] B. Al-Diri, A. Hunter, and D. Steel, "An active contour model for segmenting and measuring retinal vessels," *IEEE Transactions on Biomedical Engineering*, vol. 29, no. 9, pp. 1488–1497, 2009.

[46] O. Brinchmann-Hansen and H. Heier, "Theoretical relations between light streak characteristics and optical properties of retinal vessels," *Acta Ophthalmologica, Supplement*, vol. 179, pp. 33–37, 1986.

[47] P. Gregson, Z. Shen, R. Scott, and V. Kozousek, "Automated grading of venous beading," *Comput. Biomed. Res.*, vol. 28, no. 4, pp. 291–304, 1995.

[48] J. Shlens, *A Tutorial on Principal Component Analysis*. Institute of Nonlinear Science, University of California at San Diego, 2005.

[49] K. Li, X. Wu, D. Z. Chen, and M. Sonka, "Optimal surface segmentation in volumetric images-A graph theoretic approach," *IEEE Transactions on Pattern Analysis and Machine Intelligence*, vol. 28, no. 1, pp. 119–134, 2006.

[50] S. Lee, M. D. Abràmoff, and J. M. Reinhardt, "Retinal atlas statistics from color fundus images," vol. 7623, 2010.

[51] W. T. Freeman and E. H. Adelson, "The design and use of steerable filters," *IEEE Transactions on Pattern Analysis and Machine Intelligence*, vol. 13, no. 9, pp. 891–906, 1991.

[52] M. D. Abràmoff and M. Niemeijer, "The automatic detection of the optic disc location in retinal images using optic disc location regression," *IEEE EMBS Conference*, pp. 4432–4435, 2006.

[53] M. D. Abràmoff and M. S. A. Suttorp-Schulten, "Automatic detection of red lesions in digital color fundus photographs," *Telemedicine and e-Health*, vol. 11, no. 6, pp. 668–674, 2005.

[54] B. G. Chandran and D. S. Hochbaum, "a computational study of the pseudoflow and push-relabel algorithms for the maximum flow problem," *Operations Research*, vol. 57, no. 2, pp. 358–376, 2009.

[55] C.-L. Tsai, C. V. Steward, H. L. Tanebaum, and B. Roysam, "Model-based method for improving the accuracy and repeatability of estimating vascular bifurcations and crossovers from retinal fundus images," *IEEE Transactions on Information Technology in BioMedicine*, vol. 8, no. 2, pp. 122–130, 2004.

[56] A. Bhuiyan, B. Nath, J. Chua, and K. Ramanohanarao, "Automatic detection of vascular bifurcations and crossovers from color retinal fundus images," in *Third International IEEE Conference on Signal-Image Technologies and Internet-Based System*, pp. 711–718, 2003.

[57] H. Shen, B. Roysam, C. V. Steward, J. N. Turner, and H. L. Tanenbaum, "Optimal scheduling of tracing computations for real-time vascular landmark extraction from retinal fundus images," *IEEE Transactions on Information Technology in BioMedicine*, vol. 5, no. 1, pp. 77–91, 2001.

[58] P. Quelhas and J. Boyce, "Vessel segmentation and branching detection using an adaptive profile kalman filter in retinal blood vessel structure analysis," *LNCS*, vol. 2652, pp. 802–809, 2003.

[59] D. Calvo, M. Ortega, M. G. Penedo, and J. Rouco, "Automatic detection and characterisation of retinal vessel tree bifurcations and crossovers in eye fundus images," *Computer methods and programs in biomedicine*, vol. 103, pp. 28–38, 2011.

[60] N. Chapman, N. Witt, X. Gao, A. Bharath, A. Stanton, S. Thom, and A. Hughes, "Computer algorithms for the automated measurement of retinal arteriolar diameters," *British Journal of Ophthalmology*, vol. 85, pp. 74–79, 2001.

[61] X. Xu, M. Niemeijer, Q. Song, M. Sonka, M. K. Garvin, J. M. Reinhardt, and M. D. Abràmoff, "Vessel boundary delineation on fundus images using graph-based approach," *IEEE Transactions on Medical Imaging*, vol. 30, no. 6, pp. 1184–1191, 2011.

[62] Y. Yin, Q. Song, and M. Sonka, "Electric field theory motivated graph construction for optimal medical image segmentation," *GbRPR*, pp. 334–342, 2009.

[63] M. Christopher, D. C. Moga, S. R. Russell, J. C. Folk, T. Scheetz, and M. D. Abràmoff, "Validation of tablet-based evaluation of color fundus images," 2012.

[64] Y. Yin, X. Zhang, R. Williams, X. Wu, D. D. Anderson, and M. Sonka, "LOGISMOS-layered optimal graph image segmentation of multiple objects and surface: Cartilage segmentation in the knee joint," *IEEE Transactions on Medical Imaging*, vol. 29, no. 12, pp. 2023–2037, 2010.